

Università degli Studi di Trento

**Study of dynamic and  
ground-state properties  
of dipolar Fermi gases  
using mean-field and  
quantum Monte Carlo methods**

Ph.D. thesis by  
Natalia Matveeva

Thesis advisor: Prof. Stefano Giorgini

Facoltà di Scienze Matematiche Fisiche e Naturali

Dipartimento di Fisica

February 18, 2013



# Contents

<b>1</b>	<b>Introduction</b>	<b>1</b>
1.1	Ultracold dipolar gases . . . . .	3
<b>2</b>	<b>Dipolar drag in bilayer harmonically trapped gases</b>	<b>9</b>
2.1	Introduction . . . . .	9
2.2	Dipolar drag of the center-of-mass motion . . . . .	10
2.3	The model and the method . . . . .	11
2.4	The details of calculations . . . . .	13
2.5	Variational parameters . . . . .	14
2.5.1	Bosons . . . . .	14
2.5.2	Fermions . . . . .	16
2.6	Frequency shift: bosons versus fermions . . . . .	16
2.7	Comparison with a classical gas . . . . .	17
2.8	Conclusions . . . . .	18
<b>3</b>	<b>Quantum Monte Carlo methods</b>	<b>21</b>
3.1	Introduction . . . . .	21
3.2	Basic concepts . . . . .	24
3.3	Random walks and Metropolis sampling . . . . .	27
3.4	Variational Monte Carlo . . . . .	31
3.5	Diffusion Monte Carlo . . . . .	34
3.6	Diffusion Monte Carlo for fermions . . . . .	40
3.7	Trial wave functions . . . . .	41
3.8	Correlation functions . . . . .	42
<b>4</b>	<b>Liquid and Crystal Phases of Dipolar Fermions in Two Dimensions</b>	<b>49</b>
4.1	Introduction . . . . .	49
4.2	Calculation of the potential energy . . . . .	51
4.3	Fermi liquid phase . . . . .	53
4.3.1	General physical properties of a Fermi liquid and the Slater-Jastrow wave function . . . . .	53
4.3.2	Optimization of the variational parameter $R_p$ . . . . .	54
4.3.3	Optimization of DMC parameters: time step and number of walkers . . . . .	55
4.3.4	Extrapolation to the thermodynamic limit . . . . .	57

---

4.3.5	Equation of state, effective mass and renormalization factor . . . . .	58
4.3.6	Chemical potential and compressibility . . . . .	61
4.4	Crystal phase . . . . .	62
4.4.1	Wave function . . . . .	62
4.4.2	Optimization of the variational parameter $\alpha$ . . . . .	63
4.4.3	Finite size scaling . . . . .	63
4.5	Stripe phase . . . . .	64
4.5.1	The model . . . . .	64
4.5.2	VMC results . . . . .	66
4.5.3	Finite size scaling . . . . .	66
4.6	Quantum phase transition liquid-crystal . . . . .	67
4.7	Correlation functions . . . . .	69
<b>5</b>	<b>The impurity problem</b>	<b>75</b>
5.1	Introduction . . . . .	75
5.2	Two-body problem . . . . .	76
5.3	Perturbative calculation of the impurity chemical potential. . .	79
5.4	Trial wave function and its optimization . . . . .	81
5.5	Calculation of the potential energy . . . . .	82
5.6	Chemical potential of the impurity . . . . .	83
5.7	Effective mass of the impurity . . . . .	85
5.8	Conclusion . . . . .	85
<b>A</b>	<b>Twist-averaged boundary conditions</b>	<b>87</b>

# Acknowledgements

I would like to express my deep gratitude to my supervisor Prof. Stefano Giorgini for his great scientific support, confidence, kindness, patience and encouraging me. His willingness to give his time so generously has been very much appreciated. Also I am very grateful to Prof. Sandro Stringari and Alessio Recati with who I've been working during the first year of the PhD study.

I would like to thank all members of INO-CNR BEC center with who I always had very useful and interesting discussions, especially Gianluca Bertaina, Riccardo Rota, Marta Abad, Yun Li, Marco Larcher, Giovanni Martone, Luis Ardila, Yan-Hua Hou, Nicola Bartolo, Robin Scott, David Papoular, Tomoki Ozawa, Zou Peng, Gabriele Ferrari, Giacomo Lamporesi, Onur Umuncalilar, Phillip Hyllis, Francesco Piazza, Michael Klawunn. It was a great opportunity to spend three years in such an inspiring place. I would also like to extend my thanks to the secretaries Beatrice Ricci, Michaela Paoli, Flavia Zanon and the technician Giuseppe Froner.

Also I am very grateful to the group of Prof. Jordi Boronat in UPC, Barcelona and especially to Gregory Asrtracharchik for the hospitality during my visit, for many valuable advices and useful critiques.

The discussions with Prof. Markus Holzmann, Sebastiano Pilati and Alex Pikovski are also greatly appreciated.

And, finally, I would like to thank my husband Konstantin and my mother for their love and moral support.



# Introduction

---

In this thesis we theoretically study the dynamic and ground state properties of ultracold dipolar Fermi gases. Since 1995, when a Bose-Einstein condensate was experimentally created [1, 2], the field of ultracold gases has been developing very rapidly. The first degenerate Fermi gas has become experimentally available since 1999 [3] and during the last ten years a spectacular experimental progress has been achieved in the creation of Bose and Fermi gases with dipolar interactions (see Section 1.1). A lot of theoretical studies devoted to ultracold gases with short- and long-range interactions were performed as well. Several reviews are available: Bose [4] and Fermi [5] gases with short-range interactions, Bose [6] and Fermi [7] gases with dipolar interactions.

The interest in ultracold atoms is based on the fact that they are highly controllable and clean systems and they can be used to verify with great precision condensed-matter theoretical predictions. This task has already been largely accomplished in the case of the short-range interactions, but systems with dipolar interaction can give access to a wider range of physical phenomena. As an example, in the near future they can be used to simulate solid state systems with long-range interactions similar to Coulomb case. The new interesting features of the dipolar interaction is the possibility of controlling its strength and the anisotropic character.

In the weakly interacting regime, the mean-field approach and perturbation theory can be used to study the ground-state and dynamic properties of ultracold gases. These approaches, however, have the disadvantage that they become inaccurate with the increase of the interaction strength. Therefore, more precise numerical techniques, such as the Quantum Monte Carlo methods (QMC), are better suited to investigate the strongly interacting regime. These methods allow one to find the exact ground-state energy of a many-body Hamiltonian for bosonic systems and a very good upper bound of the ground-state energy for fermionic ones. The investigation of dynamic properties using the QMC methods is computationally very demanding and the majority of the QMC studies are devoted to the ground-state properties.

In this Thesis we apply the mean-field approach based on the Thomas-Fermi energy functional to study the dynamic properties of bilayer harmonically trapped dipolar Fermi gases. The fixed-node Diffusion Monte Carlo

method (FNDMC) is used instead to investigate the ground-state properties of two dimensional dipolar Fermi gases. This technique is also applied to the problem of one impurity in a bilayer configuration with dipolar fermions.

In the first project a trapped bilayer configuration of a dipolar Fermi gas is studied (Chapter 2). Due to the long-range character of the dipolar interaction a frequency shift of the collective dipole mode is expected. This shift can open the possibility to experimentally measure the parameters of the dipolar potential. Our goal is to propose a scheme of a drag experiment (analogous to the famous Coulomb drag experiment), which can be realized using dipolar Fermi gases. We found that this effect is relatively large and can be detected in a sample of polar molecules.

Chapter 3 contains the detailed description of the QMC methods which we use, namely the Variational and the Diffusion Monte Carlo techniques.

The second project, which is discussed in Chapter 4, is devoted to the study of the ground-state properties of a two dimensional dipolar Fermi gas at zero temperature by means of the FNDMC method. The dipoles are oriented by an external field perpendicular to the plane of motion, resulting in a purely repulsive  $1/r^3$  interaction. In the weakly interacting regime the ground state of the system can be described in terms of the Fermi liquid theory. We calculated the ground-state energy, the effective mass of a quasiparticle and the renormalization factor of the momentum distribution. In the strongly interacting regime the system is expected to undergo the transition to a crystalline phase. The point of this quantum phase transition was quantitatively established. Near the phase transition point we also searched for the existence of a stripe phase predicted by different mean-field approaches. It was found that this phase is never energetically favorable. Also, important quantities related to the system, such as the pair-distribution function, the static structure factor and the momentum distribution were obtained for a wide range of parameters.

In Chapter 5 we discuss 2D dipolar fermions in a bilayer configuration, where the dipole moments are polarized perpendicular to the planes. We consider the case of only one particle in the top layer and many particles in the bottom layer which are in the Fermi liquid phase. The intralayer interaction has a purely repulsive  $1/r^3$  character, but the interlayer one has an attractive part. This system represents an interesting impurity problem with long-range anisotropic interactions. Using the FNDMC method we calculated the chemical potential of the impurity, its effective mass and the pair-correlation function between the impurity and the bottom layer particles.

The results discussed in this thesis are published in Ref. [8] and Ref. [9].

In the rest of the Introduction we discuss the basic physical properties of ultracold dipolar gases. Also, we review the recent experimental progress in

the field of ultracold dipolar gases and the new physical phenomena which appear due to the long-range character of the dipolar interaction.

## 1.1 Ultracold dipolar gases

As it follows from the basic principles of quantum mechanics, a particle can be described as a matter wave packet with the characteristic de Broglie wave length  $\lambda_T = \sqrt{\frac{\hbar}{2\pi mk_B T}}$ , where  $T$  is the temperature,  $m$  is the atomic mass and  $k_B$  is Boltzmann's constant. At density  $n \simeq 10^{12} \text{cm}^{-3}$  and at temperature  $T \simeq 10^{-6} \text{K}$ , the mean interparticle distance  $l = 1/n^3$  is comparable or less than  $\lambda_T$  meaning that the matter waves of the different particles overlap and quantum indistinguishability becomes important. If these conditions are satisfied, a gas is in the quantum degenerate regime. It means that the effects of quantum statistics play an important role. If the temperature of an atomic ensemble is less than a critical temperature a Bose gas forms a Bose-Einstein condensate, while a Fermi gas enters gradually the degenerate regime by reducing the temperature. For a detailed description of these states of matter see the reviews [4] and [5].

If the particles of an ultracold gas do not have a dipole moment, the s-wave scattering is the dominant process. Therefore, the real interatomic potential (typically the van der Waals interaction) can be effectively replaced by the contact interaction potential

$$U_{cont}(\mathbf{r}) = \frac{4\pi\hbar^2 a}{m} \delta(\mathbf{r}) = g\delta(\mathbf{r}), \quad (1.1)$$

where  $a$  is the s-wave scattering length. As one sees from Eq. (1.1), the contact potential is isotropic, short-range and is characterized only by the value of the scattering length  $a$ . Notice that for a single-component Fermi gas the potential (1.1) is absent and only p-wave interactions are allowed by the Pauli principle.

If the particles have a dipole moment their interaction include both the contact and the dipolar part. Assuming that the dipoles are polarized by an external field (electric or magnetic) along the  $z$ -axis (see Fig. 1.1.a), the dipolar interaction has the following form

$$V_{dd}(\mathbf{r}) = \frac{d^2}{r^3} (1 - 3 \cos^2 \theta). \quad (1.2)$$

Here  $d$  is the electric (magnetic) dipole moment,  $\mathbf{r}$  is the vector connecting two particles, and  $\theta$  is the angle between  $\mathbf{r}$  and the direction of  $d$  ( $z$ -axis). The dipolar potential is anisotropic: depending on the orientation of dipoles

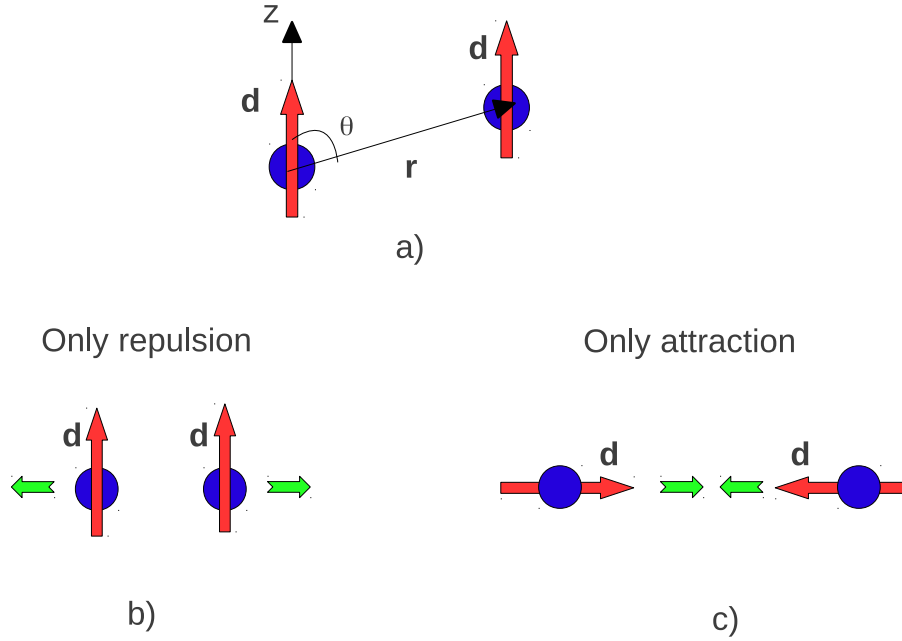


Figure 1.1: Two aligned dipoles (a), "side-by-side" configuration, purely repulsive interaction (b), "head-to-tail" configuration, purely attractive interaction (c).

with respect to  $\mathbf{r}$ , the dipolar potential  $V_{dd}$  can be completely repulsive (Fig. 1.1.b), completely attractive (Fig. 1.1.c) or partially repulsive and partially attractive. The other important property of  $V_{dd}$  is its long-range character, which appears because, from Eq. (1.2), it decays as  $\frac{1}{r^3}$  at large distances. Such long-range behavior leads to scattering properties different from the contact interaction case. As it was found in Ref. [10], for the dipole-dipole interaction the phase shift  $\delta_l$  in a scattering channel with angular momentum  $l$  behaves as  $\delta_l \sim k$  for  $l \geq 0$  and small  $k$  and therefore all partial waves must be taken into account.

The other important characteristic of the dipolar potential is the existence of a contribution to the s-wave scattering channel. It appears because, due to the anisotropy of  $V_{dd}$ , the angular momentum is not conserved during the scattering. Therefore, the dipole-dipole interaction mixes all even angular scattering channels for the bosons and all odd ones for the fermions. For two bosonic dipolar particles the scattering at low energy is determined not only by the short-range part of the interaction (Eq. (1.1)), but also by the long-range one. For two identical fermions the situation is different because, as we already mentioned, for the purely short-range interaction potential (1.1) the

s-wave contribution to the scattering amplitude is equal to zero due to the Pauli exclusion principle and the long-range dipolar part of the interaction alone defines the scattering properties.

In the weakly interacting regime the following pseudopotential was proposed in Ref. [11] to describe the properties of a polarized ultracold dipolar gas of bosons

$$V_{pseud}(\mathbf{r}) = g\delta(\mathbf{r}) + \frac{d^2}{r^3}(1 - 3\cos^2\theta), \quad (1.3)$$

where

$$g = \frac{4\pi\hbar^2 a}{m}. \quad (1.4)$$

Here  $a$  is the s-wave scattering length. It is worth noticing here that the dipolar potential (the second term in the right-hand side of Eq. (1.3)) also contributes to the s-wave scattering and therefore modifies the s-wave scattering length  $a$ . For a one-component Fermi gas the pure dipolar potential  $V_{dd}$  is used instead of Eq. (1.3).

The strength of the dipolar interaction can be characterized by the quantity

$$r_0 = \frac{md^2}{\hbar^2}. \quad (1.5)$$

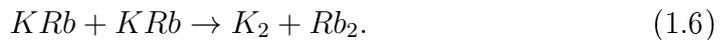
The scale of  $r_0$  in Eq. (1.5) has the dimension of length and it can be considered as the characteristic length of the dipolar interaction.

The other important property of the dipolar interaction is its tunability. There are possibilities to tune the strength and the sign of the dipolar interaction [12] as well as its shape [13, 14] using a combination of external magnetic and electric fields.

Let us discuss now the experimental progress in the field of ultracold dipolar gases. There are several possibilities to experimentally realize an ultracold gas with a dominant dipolar interaction. On one hand, one can work with atomic species having a large magnetic moment  $\mu$ . At the present time several of them are already available in the quantum degenerate regime. They are the following bosonic and fermionic atomic species:  $^{52}\text{Cr}$  [15] with  $\mu = 6\mu_B$ ,  $^{168}\text{Er}$  [16] with  $\mu = 7\mu_B$ ,  $^{164}\text{Dy}$  [17] and  $^{161}\text{Dy}$  with  $\mu = 10\mu_B$  [18] (where  $\mu_B$  is Bohr magneton). The magnetic interaction can be made stronger than the short-range one by tuning the effective scattering length close to zero using Feshbach resonances [19].

The second possibility to obtain a dipolar gas is the creation of heteronuclear polar molecules. In their lowest rovibrational state such molecules can have an induced dipole moment along the internuclear axis as large as 0.1–10 debye (D), where  $1D = 107.92\mu_B$ . For comparison, the dipole moments corresponding to  $^{52}\text{Cr}$ ,  $^{168}\text{Er}$  and  $^{164}\text{Dy}$  are  $d = 0.054 D$ ,  $d = 0.065 D$  and  $d = 0.093$

D, respectively. The most spectacular progress was obtained with  $^{40}\text{K}^{87}\text{Rb}$  fermionic molecules [20, 21, 22], which have a dipole moment  $d = 0.56D$ . The experimental technique can be described as follows: potassium and rubidium atoms are brought to quantum degeneracy, then large and very weakly bound Feshbach molecules are created by tuning the interaction close to the resonance. These molecules, which have a very small dipole moment are transferred to the rovibrational ground state, where the dipole moment can reach its maximum value. The main problem with KRb molecules is the process of two-body losses which occur due to the possibility of the following isothermal chemical reaction



At present, a three-dimensional gas of  $KRb$  molecules is available in the quantum degenerate regime, but the molecules have a dipole moment  $d = 0.2D$ . For larger values of  $d$ , a two-body losses increases exponentially due to the chemical reaction (1.6). In a 2D geometry, the losses are greatly suppressed, but the gas is not yet available in the quantum degenerate regime (the lowest obtained temperature is  $T = 2.4T_F$ ). Other heteronuclear molecules can have a dipole moment on the order of several debye. Currently, there are experimental attempts to create and bring to quantum degeneracy the following molecules: NaLi [23], NaK [24], LiCs [25] and RbCs [26].

Finally, let us mention a dipolar gas of Rydberg atoms [27, 28]. These atoms have a large dipole moment because they are in a highly excited electronic state. The disadvantage of Rydberg atoms is a very short life-time compared to the case of magnetic atoms and dipolar molecules.

Such a spectacular experimental development goes alongside with the theoretical progress. We briefly discuss some of the theoretical works, which are devoted to homogeneous and trapped systems, without considering lattice models (e. g. Bose-Hubbard model). For a general review see Ref. [7].

The ground-state properties of a spatially homogeneous and a trapped dipolar Bose gas were studied within the mean-field approximation in Refs. [29, 30, 31, 32]. It was found that a bulk system with a dominant dipolar interaction is always unstable against collapse. However, a trapped Bose gas can be stabilized when the number of particles is smaller than a critical number. The analysis of the excitation spectrum of a trapped Bose gas was performed using the time-dependent Gross-Pitaevskii equation [29, 33, 34] and the Bogoliubov- de Gennes equations [32]. For a very anisotropic pancake trap, with the dipoles perpendicular to the trap plane, the excitation spectrum has a roton-maxon shape similar to that in superfluid helium [35].

Dipolar weakly-interacting homogeneous Fermi gases with purely  $1/r^3$  interaction were studied in Ref. [36]. Such systems behave as a Fermi liquid

with modified Landau parameters. The anisotropy of the dipolar interaction leads to the anisotropy of the Fermi surface and, correspondingly, of the Fermi liquid parameters. This effect was investigated in Refs. [37, 38], using the Hartree-Fock approximation. It was also found that the anisotropy of the Fermi surface results in the appearance of a stripe phase [39, 40] characterized by stationary density modulations.

The attractive part of the dipole-dipole interaction opens the possibility of Barden-Cooper-Shifter (BCS) pairing in fermionic many-body dipolar systems. This effect was discussed in Ref. [41] for a polarized single-component dipolar Fermi gas. An exact value of the critical temperature and the angular dependence of the order parameter for a dilute gas were determined in Ref. [42]. A bilayer system of dipolar fermions was considered in Refs. [43, 44]. The long-range character of the dipolar potential couples particles from the different layers allowing for the formation of bound states and of BCS pairing.

Strongly interacting dipolar Bose gases in 2D at zero temperature were investigated in Refs. [45, 46] by means of QMC methods. It was found that at some critical density a quantum phase transition takes place and a triangular crystal forms. The finite temperature study of 2D dipolar Bose systems by Path-Integral Monte Carlo methods was performed in Ref. [47]. The case of a dipolar potential with a cut-off at small interparticle distance was considered in Ref. [48] and the appearance of a supersolid phase was predicted for this system.



# Dipolar drag in bilayer harmonically trapped gases

---

We consider two separated pancake-shaped trapped gases interacting with a dipolar (either magnetic or electric) force. We study how the center of mass motion propagates from one cloud to the other as a consequence of the long-range nature of the interaction. The corresponding dynamics is fixed by the frequency difference between the in-phase and the out-of-phase center of mass modes of the two clouds, whose dependence on the dipolar interaction strength and the cloud separation is explicitly investigated. We discuss Fermi gases in the degenerate as well as in the classical limit and comment on the case of Bose-Einstein condensed gases. This chapter shares the main results with Ref. [8].

## 2.1 Introduction

The aim of the present work is to propose a drag experiment induced by the long-range nature of the dipolar interaction. We consider an atomic or molecular gas harmonically trapped in a double well configuration such that the overlap between the two clouds and the corresponding tunneling effect can be neglected (see Fig. 2.1). The only force acting between the two gases is of long-range nature (here and in the following we assume that dipoles are oriented in the direction orthogonal to the discs, i.e along the  $z$ -th axis of Figure 1) and we study how the out-of-phase transverse dipole mode is affected by the long-range interaction. Displacing one of the two clouds out of its equilibrium position and releasing it, will excite both the in-phase (center of mass) and the out-of-phase dipole modes. On a time scale fixed by the inverse of the frequency difference between the two modes, the center of mass motion of the first cloud will be transferred to the second one. We call this effect "dipolar drag" in analogy to the well known Coulomb drag (see e.g., [49]) exhibited by electrons in uniform bilayer systems[50].

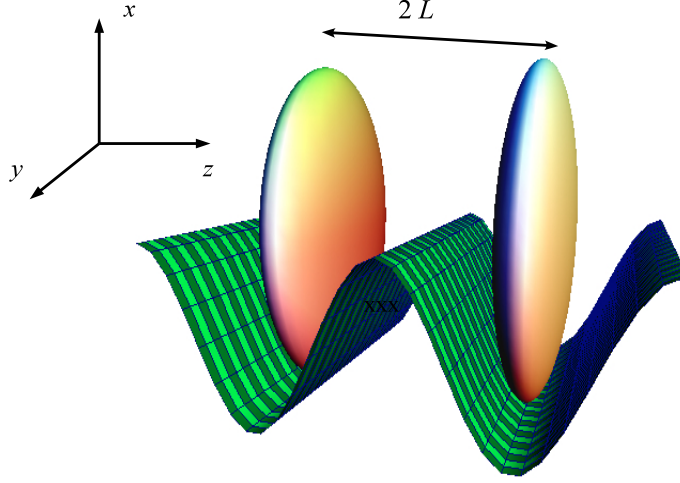


Figure 2.1: Scheme of two not overlapping pancake shaped clouds of a dipolar gas. The distance between the centers of mass of the clouds is  $2L$ . The clouds are harmonically confined in the transverse directions  $x, y$ .

## 2.2 Dipolar drag of the center-of-mass motion

We consider a gas confined by a cylindrically harmonic potential:

$$V_{trap}^{1,2}(x, y, z) = \frac{1}{2}m\omega_{\perp}^2[x^2 + y^2 + \lambda^2(z \pm z_0)^2]. \quad (2.1)$$

where  $2z_0$  is the distance between the minima of the potential along  $z$ ,  $\lambda = \omega_z/\omega_{\perp}$  is the ratio between the transverse and longitudinal trapping frequencies and we consider pancake configurations, i.e.,  $\lambda \gg 1$ . Let  $x_i$  being the center of mass coordinate along  $x$  of the  $i$ -th cloud. The equations of motion can be written as

$$\frac{d^2x_1}{dt^2} = -\omega_{\perp}^2x_1 - \alpha(x_1 - x_2), \quad (2.2)$$

$$\frac{d^2x_2}{dt^2} = -\omega_{\perp}^2x_2 + \alpha(x_1 - x_2), \quad (2.3)$$

where  $\alpha$  is the coupling between the two bare center-of-mass modes. The eigenfrequencies of the previous equations are simply  $\omega_{in} = \omega_{\perp}$ , for the in-phase sloshing mode and  $\omega_{out} = \omega_{\perp}\sqrt{1 + 2\alpha/\omega_{\perp}^2}$  for the out-of-phase sloshing mode. Thus in order to determine  $\alpha$  we just need to determine the splitting  $\omega_{out} - \omega_{\perp}$  for the dipolar coupled system. Once the frequency  $\omega_{out}$  is known, we can determine quantitatively the evolution of the system as described by Eq. (2.3). In Fig. 2.2 the motion of the coupled clouds for a value of  $\omega_{out} = 1.1\omega_{\perp}$

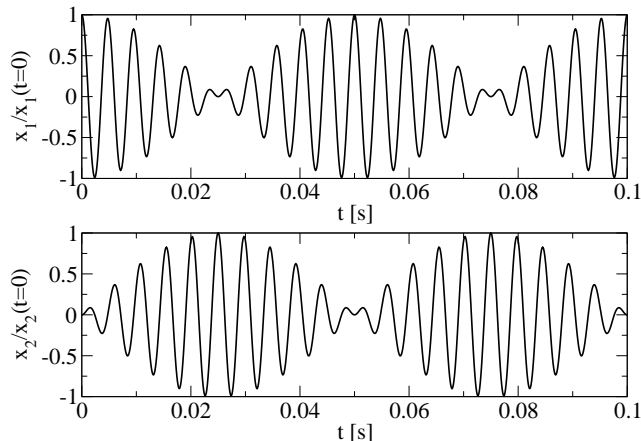


Figure 2.2: The motion of the center of mass of the two clouds for  $\omega_{out} = 1.1\omega_{\perp}$ , with  $\omega_{\perp}/2\pi = 200$  Hz which corresponds to a beating time  $\bar{t} = \pi/(\omega_{out} - \omega_{\perp}) = 0.025$ s. Initially, at  $t = 0$ , only the cloud 1 is displaced from its central equilibrium position.

is shown. The beating of the motion is a direct measurement of the out-of-phase mode frequency, since the time at which the initially displaced cloud stops in the center is simply  $\bar{t} = \pi/(\omega_{out} - \omega_{\perp})$ .

In the following we calculate the frequency  $\omega_{out}$  as a function of the dipolar interaction strength and the distance between the two clouds. We will also discuss how the equation of state of the gas affects such a frequency. The frequency  $\omega_{out}$  was recently calculated by Huang and Wu [51] in the case of a magnetic dipolar Bose gas, using a technique very similar to the one employed in the present work. For this reason we mainly focus on the case of a Fermi gas. Moreover the Fermi statistics allows for an easier realization of cold gases of hethero-nuclear molecules carrying an electric dipole moment (e.g., the recent experiment [22]) so that the strength of the dipolar force can be much larger.

## 2.3 The model and the method

We consider two clouds of dipolar ultracold gas (Fig. 2.1), each cloud is confined in the cylindrically harmonical potential (2.1).

The dipoles are oriented along the axis  $z$  by an additional external field. The interaction potential between two dipoles ( $\vec{d}_1 = \vec{d}_2 = \vec{d}$ ) has the standard form:

$$V_D(\vec{r}_1, \vec{r}_2, \theta) = \frac{d^2(1 - 3\cos^2\theta)}{|\vec{r}_1 - \vec{r}_2|^3}, \quad (2.4)$$

where  $\theta$  is the angle between  $\vec{d}$  and  $\vec{r}_1 - \vec{r}_2$ .

## 12 Chapter 2. Dipolar drag in bilayer harmonically trapped gases

The energy functional for the system has the following general form:

$$E[n_a, n_b] = E[n_a] + E[n_b] + \int d\vec{r}_a d\vec{r}_b V_D(\vec{r}_a - \vec{r}_b) n_a(\vec{r}_a) n_b(\vec{r}_b), \quad (2.5)$$

where  $n_a$  and  $n_b$  are the atomic densities for clouds  $a$  and  $b$ ,  $\vec{r}_a$  and  $\vec{r}_b$  are the coordinates relative to the two clouds,  $E[n_a]$  and  $E[n_b]$  are the energy functionals of each cloud separately.

Let us consider the small density shifts along the  $x$  axis of cloud  $a$  and cloud  $b$ :

$$n_{a,b}(x, y, z) \rightarrow n_{a,b}(x - \varepsilon_{a,b}, y, z). \quad (2.6)$$

We can write the variation of the energy (2.5) as a difference between the energy of shifted and nonshifted position:

$$\delta E = E[n_a(x - \varepsilon_a, y, z), n_b(x - \varepsilon_b, y, z)] - E[n_a(x, y, z), n_b(x, y, z)]. \quad (2.7)$$

From the other hand for small oscillations the expression (2.7) is equal to the potential energy:

$$\delta E = m\omega_D^2 N(\varepsilon_a^2 + \varepsilon_b^2), \quad (2.8)$$

where  $\omega_D$  is the frequency of the dipole mode and  $N$  is the number of atoms in each cloud. Provided that the frequency shifts  $\varepsilon_a$  and  $\varepsilon_b$  are small the expansion of expression (2.7) up to second order can be performed giving the result

$$n_{a,b}(x - \varepsilon_{a,b}) \approx n_{a,b} - \varepsilon_{a,b} \frac{\partial n_{a,b}}{\partial x} + \frac{1}{2} \varepsilon_{a,b}^2 \frac{\partial^2 n_{a,b}}{\partial x^2} + \dots \quad (2.9)$$

After substitution Eq. (2.9) into Eq. (2.7) we obtain the following expression for  $\delta E$ :

$$\delta E = \frac{1}{2} m\omega_p^2 N(\varepsilon_a^2 + \varepsilon_b^2) - \frac{1}{2} (\varepsilon_a - \varepsilon_b)^2 \int d\vec{r}_a d\vec{r}_b V_D(\vec{r}_a - \vec{r}_b) \frac{\partial n_a(\vec{r}_a)}{\partial x_a} \frac{\partial n_b(\vec{r}_b)}{\partial x_b}. \quad (2.10)$$

It can be seen from Eq. (2.10) and Eq. (2.8) that for the in-phase mode ( $\varepsilon_a = \varepsilon_b$ ) the frequency of the collective oscillation  $\omega_D$  equals the trap frequency  $\omega_p$ . But, for the out-of-phase mode ( $\varepsilon_a = -\varepsilon_b$ ) the frequency of the dipole mode is different from the trap frequency:

$$\omega_D = \omega_p \left( 1 - \frac{2}{m\omega_p^2 N} \int d\vec{r}_a d\vec{r}_b V_D(\vec{r}_a - \vec{r}_b) \frac{\partial n_a(\vec{r}_a)}{\partial x_a} \frac{\partial n_b(\vec{r}_b)}{\partial x_b} \right)^{1/2}. \quad (2.11)$$

Consequently, from Eq. (2.11), that one can see for the out-of phase mode the presence of long-range dipolar interactions leads to a shift of the dipole mode frequency. In the following we calculate the shift for experimentally relevant parameters.

## 2.4 The details of calculations

Let us denote by  $I$  the integral in Eq. (2.11)

$$I = \int d\vec{r}_a d\vec{r}_b V_D(\vec{r}_a - \vec{r}_b) \frac{\partial n_a(\vec{r}_a)}{\partial x_a} \frac{\partial n_b(\vec{r}_b)}{\partial x_b}. \quad (2.12)$$

It can be rewritten in the following way using the properties of the Fourier transformation and of the convolution:

$$\begin{aligned} I &= \int d\vec{r}_a \left( V_D * \frac{\partial n_b(\vec{r}_b)}{\partial x_b} \right)_{(\vec{r}_a)} \frac{\partial n_a(\vec{r}_a)}{\partial x_a} = \\ &= \int d\vec{k} F[V_D * \frac{\partial n_b(\vec{r}_b)}{\partial x_b}]_{(\vec{k})} F[\frac{\partial n_a(\vec{r}_a)}{\partial x_a}]_{(\vec{k})} = \\ &= \int d\vec{k} F[V_D]_{(\vec{k})} F[\frac{\partial n_a(\vec{r}_a)}{\partial x_a}]_{(\vec{k})} F[\frac{\partial n_b(\vec{r}_b)}{\partial x_b}]_{(\vec{k})}, \end{aligned} \quad (2.13)$$

where the symbol  $*$  denotes the convolution and  $F[...]$  is the Fourier transformation. The Fourier transformation of dipole potential [33] can be approximated as

$$F[V_D](\vec{k}) = 4\pi d^2 (1 - 3 \cos^2 \alpha) \left( \frac{\cos(bk)}{(bk)^2} - \frac{\sin(bk)}{(bk)^3} \right), \quad (2.14)$$

where  $\alpha$  is the angle between  $\vec{k}$  and the dipole direction, and  $b$  is a cutoff distance corresponding to the atomic radius. Since  $b$  is much smaller than any significant length scale of the system, it is possible to perform the limit

$$\lim_{b \rightarrow 0} F[V_D](\vec{k}) = \frac{4\pi}{3} d^2 (3 \cos^2 \alpha - 1). \quad (2.15)$$

In the following we will always use Eq. (2.15).

To obtain the density distributions  $n_a(\vec{r}_a)$  and  $n_b(\vec{r}_b)$  one needs to solve the stationary non-local Gross-Pitaevskii equation with long-range dipolar interactions. In the present work we use the following Gaussian ansatz for the density:

$$n_{a,b}(x, y, z) = \frac{N}{W_p^2 W_z \pi^{\frac{3}{2}}} e^{-\frac{(x^2+y^2)}{W_p^2} - \frac{(z^2 \mp 2zL + L^2)}{W_z^2}}, \quad (2.16)$$

where  $2L$  is the distance between layers  $a$  and  $b$ , while  $W_p$  and  $W_z$  are the variational parameters that define the size of the cloud.

Using spherical coordinates  $I$  can be written as:

$$\begin{aligned} I &= \frac{N^2 d^2}{6\pi^2} \int_0^\infty \int_0^\pi \int_0^{2\pi} k^4 (3 \cos^2 \alpha - 1) \sin^3 \alpha \cos^2 \phi \times \\ &\times \exp \left( -\frac{k^2}{2} \sin^2 \alpha W_p^2 - \frac{W_z^2 k^2 \cos^2 \alpha}{2} + 2iLk \cos \alpha \right) dk d\alpha d\phi. \end{aligned} \quad (2.17)$$

## 14 Chapter 2. Dipolar drag in bilayer harmonically trapped gases

After the substitution  $\cos \alpha = y$  and the integration over  $\phi$  Eq. (2.17) becomes

$$I = \frac{N^2 d^2}{6\pi^2} \tilde{I},$$

where

$$\begin{aligned} \tilde{I} = & \int_0^\infty \int_{-1}^1 k^4 (1-y^2) (3y^2 - 1) \times \\ & \times \exp\left(-\frac{y^2 k^2}{2} (W_z^2 - W_p^2) - \frac{k^2 W_p^2}{2} + 2iLky\right) dk dy. \end{aligned}$$

Finally, the expression for  $\omega_D$  can be written as

$$\omega_d = \omega_p \left(1 - \frac{Nd^2}{3\pi m \omega_p^2} \tilde{I}\right)^{1/2}. \quad (2.18)$$

## 2.5 Variational parameters

In this section we discuss the variational parameters of the Gaussian ansatz (2.16) which minimize the energy of a single cloud. The results of a Bose gas are also considered and compared to the ones of a Fermi gas.

### 2.5.1 Bosons

In the case of bosons the total energy for a single cloud has the following form [52]

$$E_{bos} = E_{trap} + E_{kin} + E_{cont} + E_{dd}, \quad (2.19)$$

where  $E_{trap} = \int n V_{trap} d\vec{r}$  is the potential energy due to the trap,  $E_{kin} = \frac{\hbar^2}{2m} \int \nabla n^2 d\vec{r}$  is the kinetic energy,  $E_{cont} = \frac{g}{2} \int n^2 d\vec{r}$  is the contact interaction energy and

$$E_{dd} = \frac{1}{2} \int n(\vec{r}) n(\vec{r}') U_{dd}(\vec{r} - \vec{r}') d\vec{r} d\vec{r}'$$

is the energy of dipolar interactions. By using the Gaussian ansatz (2.16) Eq. (2.19) becomes

$$\begin{aligned} E_{bos} = & \frac{mN\omega_p^2}{2} (W_p^2 + \frac{\omega_z^2}{2\omega_p^2} W_z^2) + \frac{N}{4m} \left(\frac{2}{W_p^2} + \frac{1}{W_z^2}\right) + \\ & + \frac{N^2 a}{\sqrt{2\pi m W_p^2 W_z}} - \frac{d^2 N^2}{3\sqrt{2\pi W_p^2 W_z}} f(\kappa), \end{aligned} \quad (2.20)$$

where  $\kappa = \frac{W_p}{W_z}$  is the cloud aspect ratio, and

$$f(\kappa) = \frac{1 + 2\kappa^2}{1 - 2\kappa^2} - \frac{3\kappa^2 \arctan \sqrt{1 - \kappa^2}}{(1 - \kappa^2)^{3/2}}.$$

As an example of a bosonic dipolar gas we consider  $^{52}\text{Cr}$  atoms (that have relatively large magnetic dipole moment  $d_{Cr} = 6\mu_B$ ) and  $^{41}\text{K}^{87}\text{Rb}$  polar molecules. The first case is important because BEC of  $^{52}\text{Cr}$  atoms has been already created experimentally [15]. The second case is also very interesting because  $^{41}\text{K}^{87}\text{Rb}$  molecules have a large electric dipole moment ( $d_{KRB} = 0.6D$ ) in the rovibrational ground state and their fermionic counterpart ( $^{40}\text{K}^{87}\text{Rb}$ ) is already available experimentally in the degenerate regime [22].

In Table 2.1 the values of  $W_p$ ,  $W_z$  are shown for different trap aspect ratios ( $\lambda = \frac{\omega_z}{\omega_p}$ ) in the case of  $^{52}\text{Cr}$  (for  $\lambda = 1.6$  notice that the cloud is predicted to be spherical). The other parameters are as follows: number of atoms 30000 and  $\bar{\omega} = 2\pi \cdot 800$  Hz, where  $\bar{\omega} = (\omega_p^2 \omega_z)^{1/3}$  is the average trap frequency. The scattering length is taken to be equal to  $18a_0$ , where  $a_0$  is the Borh radius,  $a_p = \sqrt{\hbar/m\omega_p}$  and  $a_z = \sqrt{\hbar/m\omega_z}$  are the oscillator lengths in the radial and axial direction.

Table 2.1: Bosons. The size of cloud for  $^{52}\text{Cr}$ .

$\lambda$	$\frac{\omega_p}{2\pi}, \text{Hz}$	$\frac{\omega_z}{2\pi}, \text{Hz}$	$W_p, 10^{-4}\text{cm}$	$W_z, 10^{-5}\text{cm}$	$\frac{W_p}{a_p}$	$\frac{W_z}{a_z}$
1.6	684	1094	1.05	10	1.88	2.5
10	372	3720	2.5	3.2	2.8	1.4
20	295	5894	3.2	2.3	3.94	1.3
40	234	9356	3.9	1.6	4.28	1.1

The cloud size for the bosonic polar molecule  $^{41}\text{K}^{87}\text{Rb}$  is shown in the Table 2.2 at the same number of atoms and trap parameters (the case  $\lambda = 1.6$  absence because cloud is unstable for such parameters). The scattering length here is equal to  $100a_0$ .

Table 2.2: Bosons. The size of cloud for  $^{41}\text{K}^{87}\text{Rb}$ .

$\lambda$	$\frac{\omega_p}{2\pi}, \text{Hz}$	$\frac{\omega_z}{2\pi}, \text{Hz}$	$R_p, 10^{-4}\text{cm}$	$R_z, 10^{-5}\text{cm}$	$\frac{R_p}{a_p}$	$\frac{R_z}{a_z}$
10	372	3720	4.14	5	9	3.4
20	295	5894	5.6	2.8	10.8	2.4
40	234	9356	7.2	1.9	12.4	2.1

## 2.5.2 Fermions

The total energy of a single cloud of dipolar fermions can be expressed in terms of the Thomas-Fermi energy functional [53]

$$E_{ferm} = \frac{3}{5} \frac{\hbar^2}{2m} (6\pi^2)^{2/3} \int n^{5/3} d^3x + E_{dd} + E_{pot}, \quad (2.21)$$

where  $E_{dd}$  and  $E_{pot}$  are the same as in the bosonic case. In the energy functional (2.21) we have not included the intra-cloud exchange energy. We safely neglect it, because for the pancake-like configurations, which are our main interest, the direct term is the dominant effect (see, e.g., [37]).

For the Gaussian ansatz (2.16)  $E_{ferm}$  becomes

$$E_{ferm} = \left(\frac{3}{5}\right)^{5/2} 6^{2/3} \frac{1}{2m} \pi^{1/3} \frac{N^{5/3}}{R_p^{4/3} R_z^{2/3}} + \frac{mN\omega_p^2}{2} (R_p^2 + \frac{\omega_z^2}{2\omega_p^2} R_z^2) - \frac{d^2 N^2}{3\sqrt{2\pi} W_p^2 W_z} f(\kappa). \quad (2.22)$$

In Table 2.3 the size of the cloud is shown for the fermionic polar molecules  $^{40}\text{K}^{87}\text{Rb}$ . The trap parameters, the number of atoms and the scattering length are taken to be the same as for the bosonic polar molecule  $^{41}\text{K}^{87}\text{Rb}$ .

Table 2.3: Fermions. The size of cloud for  $^{40}\text{K}^{87}\text{Rb}$ .

$\lambda$	$\frac{\omega_p}{2\pi}, Hz$	$\frac{\omega_z}{2\pi}, Hz$	$R_p, 10^{-4}\text{cm}$	$R_z, 10^{-5}\text{cm}$	$\frac{R_p}{a_p}$	$\frac{R_z}{a_z}$
10	372	3720	4.64	5.28	10	3.6
20	295	5894	6.1	3.25	11.7	2.8
40	234	9356	7.84	2.02	13.4	2.18

From the comparison of Table 2.2 and Table 2.3 one sees that for the same trap parameters and value of the dipolar moment the fermionic cloud has a larger size compared to the bosonic one. This effect is a direct consequence of the Pauli exclusion principle.

## 2.6 Frequency shift: bosons versus fermions

In this section we study the frequency of the dipole mode (2.18) for bosonic ( $^{52}\text{Cr}$  and  $^{41}\text{K}^{87}\text{Rb}$ ) and fermionic ( $^{40}\text{K}^{87}\text{Rb}$ ) dipolar gases. We use the variational parameters which were presented in the previous section. Fig. 2.3 shows the dependence of  $\omega_D$  on the distance  $L$  between the clouds at different values of the parameter  $\lambda$ . The top figure shows the results for  $^{52}\text{Cr}$ . One

can see that the effect of the frequency shift is not too small (around several percents) and, in principle, can be experimentally detected. The middle and bottom figures depict the  $\omega_D$  for  $^{41}\text{K}^{87}\text{Rb}$  and  $^{40}\text{K}^{87}\text{Rb}$  polar molecules. The effect is slightly larger for bosons than for fermions. This fact can be understood in the following way: as emerges from Eq. (2.11) the effect is amplified for smaller radial sizes where the gradient of the density is larger, and, as it was discussed above, the sizes  $W_p$  and  $W_z$  are smaller for a bosonic cloud.

Moreover, we see that for small enough distances the larger the cloud (larger  $\lambda$  for fixed  $N$ ) the smaller the effect. This can be easily understood in terms of the potential of a single disk of radius  $W_\perp$  on a probe dipole. Indeed at a distance  $z \ll W_\perp$  the potential decays with  $W_\perp$ , which is a general result independent of statistics. On the other hand we have that the asymptotic behavior of the frequency shift at large distance is  $\propto \sqrt{1 + C/L^5}$  with  $C$  a constant, which is the result one immediately obtains by considering just two trapped dipoles. It can also be easily shown that for spherical clouds with  $W_\perp = W_z = W$  in Eq. (2.11) the frequency of the out-of-phase dipole mode reads

$$\omega_{out} = \omega_\perp \left( 1 - \frac{\sqrt{2}Nd^2h(L/W)}{3\sqrt{\pi}m\omega_\perp^2L^5} \right)^{1/2}, \quad (2.23)$$

where  $h(y) = e^{-2y^2}(4y^5 + 6y^3 + 9/2y) - 9/2\sqrt{\frac{\pi}{2}}\text{Erf}(\sqrt{2}y)$ , which approaches a constant for large values of  $y$ .

## 2.7 Comparison with a classical gas

An important question arises: is it possible to detect the frequency shift of dipolar mode for a classical gas? This section is devoted to the comparison of  $\omega_D$  for a degenerate Fermi gas of  $^{40}\text{K}^{87}\text{Rb}$  molecules with a classical gas composed of the same molecules. Here we chose other parameters for the trap and number of particles, which should be closer to the parameters of the  $^{41}\text{K}^{87}\text{Rb}$  experiment [22]. The Tables 2.4 and 2.5 show the variational parameters for degenerate and classical gases, correspondingly. There  $T_F \equiv \hbar\omega_\perp(6N\lambda)^{1/3}/k_B$  is the Fermi temperature and  $k_B$  is Boltzmann's constant. For a classical gas we use simply the Gaussian density profiles of Eq. (2.16) where the radii are given by the Boltzmann expression  $W_\perp^2 = 2k_B T/(m\omega_\perp^2)$  and  $\kappa = \lambda$ .

In Fig. 2.4 and Fig. 2.5 we report the predictions for the frequency shifts exhibited by the degenerate gas and the thermal configuration calculated at the temperature  $T = T_F$ . The variational parameters are taken from Tables 2.4 and 2.5. We see that the effect, for the same trapping conditions and

## 18 Chapter 2. Dipolar drag in bilayer harmonically trapped gases

Table 2.4: The cloud size for  $N = 2200$   $^{40}\text{K}^{87}\text{Rb}$  molecules with  $\omega_z/2\pi = 10$  kHz (corresponding to  $a_z = 8.89 \times 10^{-6}\text{cm}$ ) and dipole momentum  $d = 0.56$  D.

$\lambda$	$W_{\perp}, 10^{-4}\text{cm}$	$W_z, 10^{-5}\text{cm}$
10	1.8	2.05
20	2.9	1.54
40	4.6	1.17

Table 2.5: The size of cloud for classical gas of  $^{40}\text{K}^{87}\text{Rb}$  at  $T = T_F$  with dipole momentum  $d = 0.56\text{D}$  and trapping frequency  $\omega_z = 10$  kHz ( $a_z = 8.89 \times 10^{-6}\text{cm}$ ).

$\lambda$	$W_{\perp}, 10^{-4}\text{cm}$	$W_z, 10^{-5}\text{cm}$
10	2.8	2.8
20	4.5	2.25
40	7.15	1.79

number of particles, is smaller for a classical gas than for a degenerate Fermi gas, since the thermal radii are larger and the densities smaller than the ones of the degenerate configuration.

## 2.8 Conclusions

We have proposed a drag experiment between two non-overlapping atomic/molecular clouds (see Fig. 2.1 and Fig. 2.2) to test the long-range nature of the dipolar potential. The method is independent of quantum statistics and holds for both degenerate and thermal gases. This effect corresponds to the trapped version of the famous Coulomb drag exhibited by electrons in uniform bilayer systems. The realization of such a drag experiment would provide a direct and easy signature of the long-range nature of the dipole interaction.

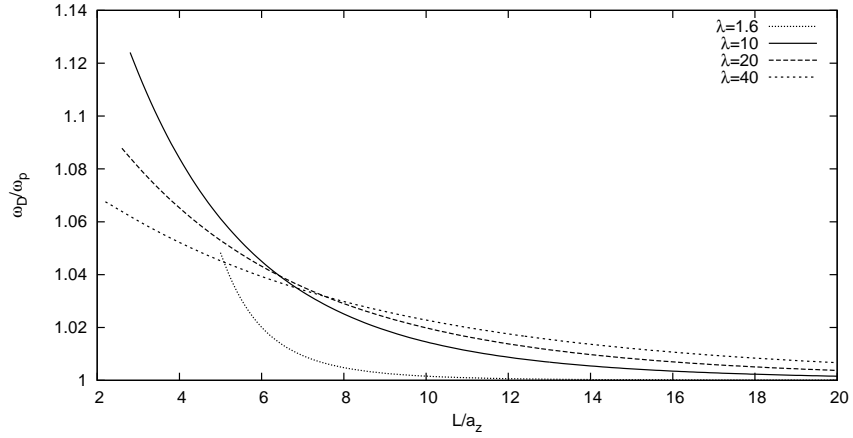
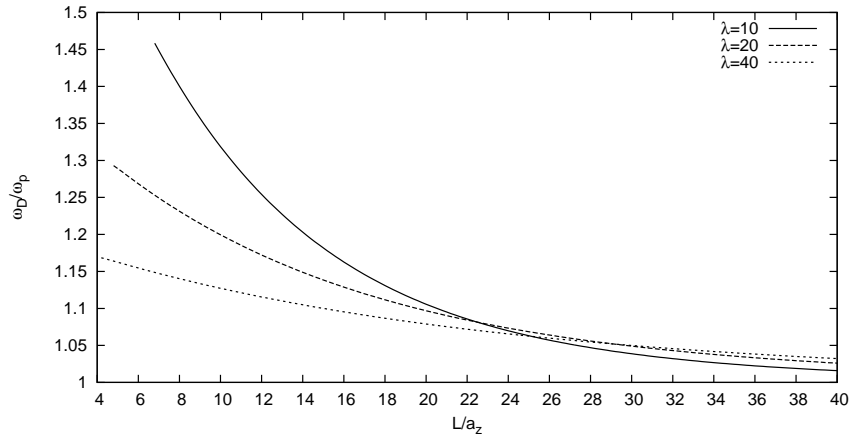
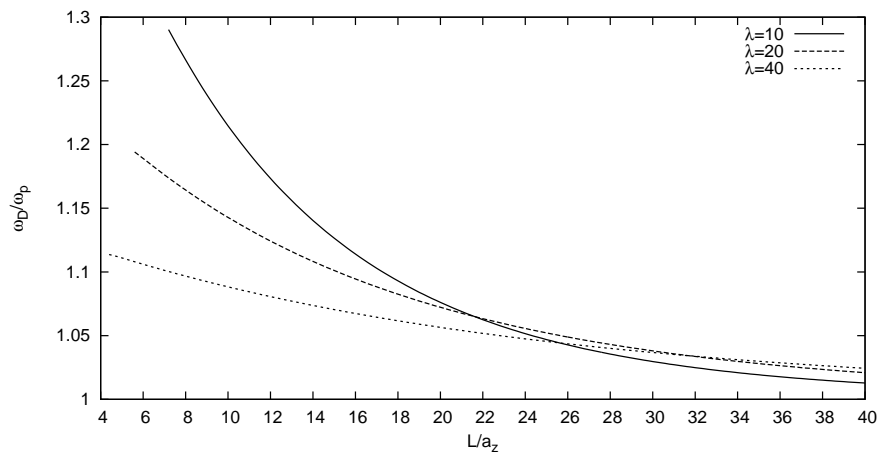
(a) Frequency shift of dipole mode for  $^{52}\text{Cr}$ .(b) Frequency shift of dipole mode for  $^{41}\text{K}^{87}\text{Rb}$ .(c) Frequency shift of dipole mode for  $^{40}\text{K}^{87}\text{Rb}$ .

Figure 2.3: Frequency shift of dipole mode for bosons:  $^{52}\text{Cr}$  (a),  $^{41}\text{K}^{87}\text{Rb}$  (b); and for fermions  $^{40}\text{K}^{87}\text{Rb}$  (c).

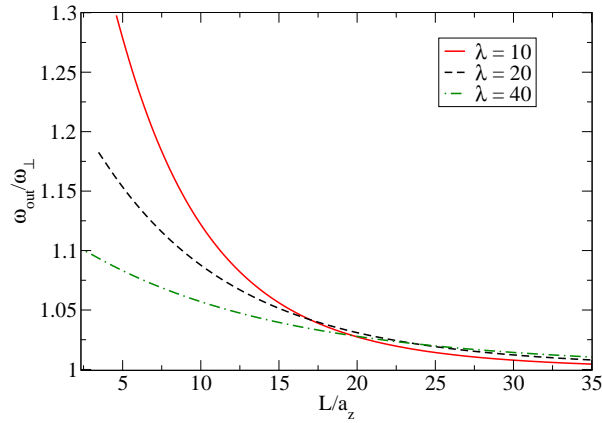


Figure 2.4: Frequency shift of  $\omega_{out}/\omega_{\perp}$  for the out-of-phase mode for a degenerate gas of  $^{40}\text{K}^{87}\text{Rb}$ , with parameters as given in Table 2.4.

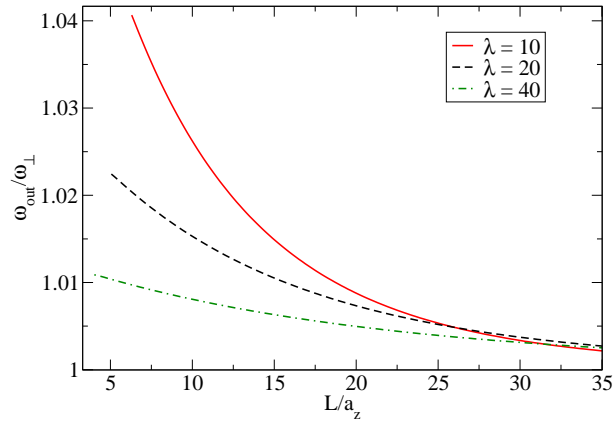


Figure 2.5: Frequency shift of  $\omega_{out}/\omega_{\perp}$  for the out-of-phase mode for a classical gas of  $^{40}\text{K}^{87}\text{Rb}$  at temperature  $T = T_F$ , where  $T_F$  is the Fermi temperature of the gas. Parameters are given in Table 2.5.

# Quantum Monte Carlo methods

---

In this chapter we describe Quantum Monte Carlo methods and the underlying concepts, such as Markov chains and Metropolis algorithm. We discuss Variational and Diffusion Monte Carlo techniques, as well as trial wave functions used for bosonic and fermionic systems.

## 3.1 Introduction

The behavior of a nonrelativistic quantum system can be described by the many-body Schroedinger equation. The ground state expectation value of an operator can be found as a quantum-mechanical average on the many-body wave function that leads to the calculation of multidimensional integrals. Usually we are interested in the physical properties of a system which contains a large number of particles, so the problem of solving Schroedinger's equation as well as calculation of the observables becomes very difficult. If the degrees of freedom are strongly coupled, perturbation theories are not reliable and the use of different numerical techniques becomes necessary.

Monte Carlo (MC) methods are a class of techniques that are used to solve multidimensional integrals, where grid methods becomes ineffective because the number of grid points rapidly increase with dimensionality. The essential property of MC methods is the stochastic nature, which arises from the use of random number sequences. More exactly, to compute the results, Monte Carlo methods rely on repeated random sampling which is governed by a probability distribution function. The term "quantum Monte Carlo" (QMC) covers several related stochastic methods that are used to investigate the properties of a variety of quantum systems. The word "quantum" is important since QMC approaches differ significantly from Monte Carlo methods for classical systems.

Originally MC methods were developed mainly to study the properties of condensed matter systems. Historically the first method was Variational Monte Carlo (VMC), which was used to study the ground-state properties of a bosonic isotope of helium, namely  $\text{He}^4$  [54]. In that method the modulus square of a trial wave function plays the role of a probability distribution, which is used to stochastically sample physical observables. It provides an

upper bound of the ground-state energy (both for bosons and fermions) which crucially depends on the quality of the trial wave function used. The ground-state energy of liquid  $\text{He}^4$  was found to be in agreement with the experimental value using more sophisticated wave functions [55]. VMC was also used to study the fermionic isotope  $^3\text{He}$  ([55], [56]) and later to investigate the ground-state properties of the electron gas. Later the Green's Function Monte Carlo (GFMC) method was developed and used for  $^4\text{He}$  [57]. For bosons GFMC method samples a probability distribution proportional to the exact ground-state wave function, and it gives an exact ground-state energy biased only by a statistical error, which can be decreased at the cost of simulation time. For fermions GFMC was first used in [58]. Another method called Diffusion Monte Carlo (DMC) was introduced in [59]. DMC solves the Schroedinger equation in imaginary time based on the short-time approximation of the Green function. It had allowed to significantly improve the VMC results for the electron gas [61]. DMC is similar to GFMC but simpler in implementation which makes DMC a very popular method up to the present time (for review see [62]).

All techniques mentioned before are valid only at zero temperature. But there is the possibility to study finite temperature properties of quantum systems using Path Integral Monte Carlo methods (PIMC). They are based on the isomorphism between the partition function of quantum particles in the canonical ensemble representation and classical polymers. This partition function can be simulated using Monte Carlo algorithms. Firstly PIMC was used to study low-temperature properties of liquid  $^4\text{He}$  [63] and then became a standard technique to study quantum liquids. Recently more sophisticated variants of PIMC were developed such as the Worm algorithm [64], which allows one to consider very large systems (up to several hundred thousands of bosons).

Unfortunately, QMC methods, that are exact for bosons, are only approximate for fermions because of the sign problem. This problem is a consequence of the fundamental quantum mechanical statement which requires antisymmetry of the many-body wave function with respect to particles exchange. Therefore the probability distribution sampled during the simulation can not be proportional to the many-body wave-function because it should be positively defined and various approximations were developed to overcome this problem. In case of the DMC method a valid scheme is provided by the fixed-node approximation, where the nodes of the ground-state wave function are chosen to coincide with the nodes of a trial wave function. Since the exact nodes of the ground state are in general not known the energy calculated by the fixed-node DMC method is only an upper bound to the exact ground-state energy. In case of PIMC method, an algorithm for fermions, called constrained

Path-Integral technique discussed in [65], [66], deals with the sign problem at finite temperature.

During the last twenty years these methods were employed to study ultracold atomic systems. In the following we describe some of the most important QMC results. Initially, only systems with short-range contact interaction were studied.

We first consider continuum systems. In Bose gases, beyond mean-field corrections to the equation of state at zero temperature were calculated in three dimensions [67], two dimensions [68] and one dimension [69]. In fermionic systems, QMC approaches were used to give quantitative information about the BEC-BCS crossover [70], and especially the unitarity regime where there is no small parameter for perturbation theory. For example, the equation of state at zero temperature was calculated in [71] and in [72]. Another interesting phenomena such as itinerant ferromagnetism was studied by means of the FNDCM method for a three dimensional repulsive Fermi gas [73], where evidence for a ferromagnetic phase was found.

Lattice models which are described by different variants of the Hubbard model also attracted a lot of attention. The Bose-Hubbard model [74], which is the simplest model that describes a conductor-insulator transition for bosons was the object of many studies. Such interest is based on the hope that bosons in optical lattices can play the role of quantum simulators for solid state systems (see Introduction). In [75] the superfluid to normal liquid transition of the Bose - Hubbard model was experimentally investigated and benchmarked against the theoretical calculations. The integrated column densities from time-of-flight images showed excellent agreement with the results of the worm algorithm PIMC method over the whole temperature range. Remarkably, the QMC simulations were performed for  $3 * 10^5$  bosons, the same number of particles presenting in the experiment. Disordered Bose-Hubbard model for 3D bosons was studied by QMC methods in [76], [77]. The authors found that the Bose glass phase is an intermediate phase between the superfluid and Mott insulator phases of the Bose-Hubbard model.

In the case of fermions the attractive Hubbard model was studied at unitarity in [78], [79], and the superfluid transition temperature as well as the thermodynamic properties for unpolarized gases have been calculated.

Let us now move to the progress of QMC studies of ultracold systems with long-range interactions (for a review see [80]). One of the interesting questions which was addressed by QMC methods is the phenomenon of supersolidity. Two-dimensional Bose-Hubbard model with dipolar interactions was studied in [81], [82] and a supersolid phase was found as an intermediate phase between the superfluid and solid phase. A bulk two dimensional bosonic system with pure repulsive  $1/r^3$  dipolar interaction was investigated at zero temperature

in [45], [46]. It was found that at small densities the ground state of the system is a liquid and at large densities a triangular crystal is formed. For  $1/r^3$  interaction with a cut-off at small distances, the supersolid phase was instead predicted to appear at least in two dimensions [48]. This phase is formed through the formation of superfluid droplets that become coherent as one lowers the temperature.

Finally, let us mention the Diagrammatic Monte Carlo method, which was developed to investigate the properties of fermionic systems at finite temperature. This method is based on a direct sampling of Fermi diagrams that contribute to physical properties. Recently, in [83] the equation of state of a balanced Fermi gas at unitarity was determined using this method.

## 3.2 Basic concepts

As it was already mentioned the most important use of Monte Carlo methods is the calculation of multidimensional integrals. Non-stochastic methods, such as grid methods are highly effective for low dimensional integrals or in case where the integrand can be approximately separated into low dimensional parts. But when the dimensionality  $d$  of the space increases the number of grid points increases as  $N^d$ . For the case  $d \leq 5$  some more sophisticated grid techniques can still be effective. But for higher dimensions the computational efforts increase so rapidly, that other possibilities such as Monte Carlo sampling become more favorable. Monte Carlo integration is based on sampling points from an appropriate probability distribution function instead of using a grid.

Let us explain the idea of Monte Carlo evaluation of definite integrals. Only the one dimensional case is considered below, but the results can be easily generalized to the multidimensional case.

At the beginning, let us define what is a random variable. Let us consider for example such process as throwing a dice. At each trial the result of this action can be expressed in term of a numerical value  $x$  which is called a random variable. It can be discrete or take values in the continuum. The random variable is characterized by its domain and its probability distribution function (pdf), which also can be discrete or continuous. As an example, two common pdf's are written below. The first one is the uniform distribution, defined in  $[a, b]$  as

$$f(x) = \frac{1}{(b-a)}\theta(x-a)\theta(b-x), \quad (3.1)$$

where  $\theta$  is a Heaviside step function. The second one is the Gaussian distri-

bution defined in  $(-\infty, +\infty)$  as

$$f(x) = \frac{1}{\sqrt{2\pi}\sigma} \exp^{-\frac{(x-\bar{x})^2}{2\sigma^2}}. \quad (3.2)$$

Usually we are not directly interested in the value of the variable  $x$  but in some function  $g(x)$ . In this case the expectation value of  $g$  can be found as

$$\langle g \rangle = \int_a^b g(x)f(x)dx, \quad (3.3)$$

here it is assumed that  $x$  is defined in the interval  $(a, b)$ . The important characteristics of a distribution are its mean value  $\mu$  and central moments  $\mu_n$ . Mean value is defined for  $g(x) = x$  as

$$\langle x \rangle = \mu = \int_a^b xf(x)dx \quad (3.4)$$

and another choice of  $g(x)$  such as  $g(x) = (x - \mu)^n$  determines the central moments as

$$\mu_n = \int_a^b (x - \mu)^n f(x)dx. \quad (3.5)$$

The second central moment  $\mu_2$  is called the variance of the probability distribution, usually its square root  $\sigma$  is used which corresponds to the standard deviation.

Now we are ready to discuss the central limit theorem (CLT). Let us consider a random variable  $x$  with probability distribution  $f(x)$  which has mean value  $\mu$  and variance  $\sigma$ . Also let us define the random variable  $z$  as the average over  $n$  random realizations of  $x$ :

$$z = \frac{x_1 + x_2 + \dots + x_n}{n}. \quad (3.6)$$

The CLT tells us that for  $n$  large enough the random variable  $z$  is distributed according to the Gaussian distribution (3.2) independently of the form of  $f(x)$ . More exactly, the pdf  $p(z)$  of the random variable  $z$  is

$$p(z) = \frac{1}{\sqrt{2\pi}} \frac{1}{(\sigma/\sqrt{n})} \exp\left(-\frac{(z - \mu)^2}{2(\sigma/\sqrt{n})^2}\right). \quad (3.7)$$

The mean of  $p(z)$  equals the mean of the original distribution  $f(x)$  and its variance is equal to the variance of  $f(x)$  divided by  $n$ .

So, the CLT proves that the mean of the probability distribution  $f(x)$  can be found as the average over  $n$  realizations of  $x$ . And the error in its determination decreases with the square root of  $n$ .

The importance of CLT is that it can be used not only for the calculation of the mean value of a probability distribution but can be easily generalized to other types of expectation values such as

$$m_h = \int_a^b h(x)f(x)dx, \quad (3.8)$$

which has the variance

$$s^2 = \int f(x)(h(x) - \mu_h)^2 dx. \quad (3.9)$$

The generalized version of CLT tells us that  $m_h$  can be estimated as the mean value of a new random variable

$$z_h = \frac{h(x_1) + h(x_2) + \dots + h(x_n)}{n}. \quad (3.10)$$

The variance of this estimate of  $m_h$  is equal to the  $s^2/n$ .

The most important use of CLT is the possibility to calculate defined integrals stochastically. Suppose we are interested in the calculation of the integral

$$I = \int_a^b h(x)dx, \quad (3.11)$$

where  $h(x)$  is an arbitrary function (no necessarily positively defined). One can rewrite the integral  $I$  as

$$I = (b - a) \int_a^b h(x)f(x)dx, \quad (3.12)$$

where  $f(x)$  is the uniform distribution (3.1). Now the integral  $I$  can be considered as the expectation value  $m_h$  of  $h(x)$  on the distribution  $f(x)$

$$I = (b - a) \langle h \rangle_u. \quad (3.13)$$

According to CLT the expectation value  $\langle h \rangle_u$  can be estimated as the average over a large number  $N$  of  $h(x_i)$ , where  $x_i$  are sampled from the uniform distribution

$$\langle h \rangle_u \approx \bar{h} = \frac{1}{N} \sum_{i=1}^N h(x_i). \quad (3.14)$$

The variance of this estimate of  $I$  is equal to

$$\sigma_I^2 = \sigma_h^2/N, \quad (3.15)$$

where for a finite number of samples

$$\sigma_h^2 \approx \frac{1}{N} \sum_{i=1}^N (h(x_i) - \bar{h})^2. \quad (3.16)$$

Therefore the variance in the estimate of the integral  $I$  equals

$$\sigma_I^2 \approx \frac{1}{N^2} \sum_{i=1}^N (h(x_i) - \bar{h})^2. \quad (3.17)$$

One can see that the variance  $\sigma_I^2$  depends on the variance of the function  $h(x)$  and on the number  $N$  of samples. But the variance  $\sigma_h^2$  depends only on the shape of the function  $h(x)$ . Therefore, the only way to reduce  $\sigma_I$  is to increase  $N$ . This limitation can be overcome by using the importance sampling technique, which allow one to significantly reduce the variance of the integrand function.

In order to do this we should rewrite the integral (3.12) as

$$I = \int_a^b \frac{h(x)}{q(x)} q(x) dx = \left\langle \frac{h(x)}{q(x)} \right\rangle_q, \quad (3.18)$$

where  $\frac{h(x)}{q(x)}$  is the new integrand function and  $q(x)$  is the new (not uniform!) distribution function such that  $q(x)$  is close to  $h(x)$ . So, the integral can be estimated as

$$I \approx \frac{\overline{h(x)}}{q(x)} = \frac{1}{N} \sum_{i=1}^N \frac{h(x_i)}{q(x_i)}, \quad (3.19)$$

where the points  $\{x_i\}$  are sampled from  $q(x)$ . The probability to sample a given point  $x_i$  is larger where  $h(x)$  is large and smaller where  $h(x)$  is small, which leads to smaller fluctuations of  $\frac{h(x_i)}{q(x_i)}$  and, finally, to a decrease of the variance with respect to the case of the uniform distribution.

### 3.3 Random walks and Metropolis sampling

In this section we discuss sampling from an arbitrary distribution function. In some cases the sampling can be done relatively easily, as, for example, for the Gaussian probability distribution (3.2), where the Box-Muller algorithm was developed [85]. Suppose we want to sample from a Gaussian distribution (3.2) with  $\sigma = 1$  and  $\mu = 0$ . Firstly, one needs to sample two random variables  $u_1$  and  $u_2$  from the uniform distribution (3.1) with  $a = 0$  and  $b = 1$  using, for example, the standard algorithms `ran2` or `ran3` from [86]. Then, two variables  $x_1$  and  $x_2$  should be calculated as

$$x_1 = \sqrt{-2 \log u_1} \cos(2\pi u_2), \quad x_2 = \sqrt{-2 \log u_1} \sin(2\pi u_2). \quad (3.20)$$

These variables  $x_1$  and  $x_2$  are independent random variables distributed according to a Gaussian pdf. In case of arbitrary  $\sigma$  and  $\mu$ , the random variables  $x_{1,2}$  should be rescaled as  $x_{1,2} \rightarrow \sigma x_{1,2} + \mu$ .

In case of more sophisticated pdf's, usually there is no easy way to sample points from them. Metropolis and coworkers [87] developed a stochastic algorithm which generate asymptotically the given set of random numbers. This algorithm is based on a random walk in multidimensional space. Before going to the details of this algorithm we explain the underlying concept of Markov chain [84].

Firstly, let us define a "walker" as a mathematical quantity which completely describes the state of the system. The walker moves in configurational space by combination of deterministic and random displacements. Suppose the system has  $N$  states  $S_1, \dots, S_N$  such that the probability for the system to occupy each of the states at a given time  $i$  is  $p_1^i, \dots, p_N^i$ . All this probabilities form the probability-space density, which can be represented as the vector

$$\mathbf{p}^i = [p_1^i \dots p_N^i]^T. \quad (3.21)$$

If the system starts its evolution from the state  $S_i$ , then after some time it ends at  $S_f$  after a sequence of jumps between intermediate states. If at every time the current state depends only on the previous one, then such a sequence of events is called a "Markov chain". The probability of the system to jump from state  $S_j$  to  $S_k$  in one time step is defined as  $P_{kj}$ . The whole set of probabilities  $\{P_{kj}\}$  forms so called transition probability matrix  $\hat{P}$ . It is obvious that its elements must satisfy the following conditions:  $0 \leq P_{kj} \leq 1$  and  $\sum_j P_{kj} = 1$ .

What happens to a system after a large number of jumps? Suppose that at time  $i$  the system is in the state  $S_j$  and then at the next time step  $i + 1$  it moves to  $S_k$  with probability  $P_{kj}$ . During this jump the probability distribution changes as  $p_k^{i+1} = \sum_j P_{kj} p_j^i$ , which can be written in a matrix form as  $\mathbf{p}^{i+1} = \hat{P} \mathbf{p}^i$ . Using this notation the evolution of the system from the initial distribution can be written as follows:  $\mathbf{p}^1 = \hat{P} \mathbf{p}^0$ , then  $\mathbf{p}^2 = \hat{P} \mathbf{p}^1 = \hat{P} \hat{P} \mathbf{p}^0$  and so on. After  $m$  steps the probability-space density becomes  $\mathbf{p}^m = \hat{P}^m \mathbf{p}^0$ . If time  $m$  is sufficiently long  $|\mathbf{p}^{m+1} - \mathbf{p}^m| \rightarrow 0$ , which means that the system has reached the equilibrium probability distribution  $\mathbf{p}^*$ , defined as

$$\mathbf{p}^* = \hat{P} \mathbf{p}^*. \quad (3.22)$$

The probabilities  $p^*$  can be found as the solution of the set of linear equations (3.22). The existence of such equilibrium state requires that the system satisfies some conditions, one of the most important is the ergodicity, which means that none of the possible states has zero probability for being visited by the walker.

The generalization of the discussed concept to the case of continuum space is called a Markov process. In this case the states can be labeled by the continuous variable  $x'$  and the transition probability can be defined as a function  $p(x, x')$  with the properties  $p(x, x') > 0$  and  $\int p(x, x') dx' = 1$ .

Above we have considered a direct problem: how to get the stationary probability distribution which corresponds to a given transition probability matrix. But our sampling task requires the solution of the inverse problem: we should be able to find an appropriate  $\hat{P}$  for the desired  $\mathbf{p}^*$ . This issue is addressed by the Metropolis algorithm [87, 88].

Assume the system is in state  $S_i$  which has the equilibrium probability  $p_i^*$ . Then let us choose a trial state  $S_j$  which has the equilibrium probability  $p_j^*$ . The probability of transition between these two states is denoted as  $Q_{ij}$ , where  $\hat{Q}$  could be an arbitrary matrix. If  $p_j^* > p_i^*$  then the move is accepted and the matrix element of the matrix  $\hat{P}$  is  $P_{ij} = Q_{ij}$ . If  $p_j^* \leq p_i^*$  the trial state is accepted with the probability  $p_j^*/p_i^*$ . In case the state  $S_j$  is not accepted the new state is the old one. More precisely the above statements can be written as follows:

$$P_{ij} = Q_{ij}, (p_j^* > p_i^*) \quad (3.23)$$

$$P_{ij} = Q_{ij} p_j^*/p_i^*, (p_j^* \leq p_i^*) \quad (3.24)$$

$$P_{ii} = Q_{ii} + \sum_{k, p_k^* < p_i^*} Q_{ik} (1 - p_k^*/p_i^*) \quad (3.25)$$

The last equation (3.25) is chosen in such a form to fulfill the condition  $\sum_j P_{kj} = 1$ .

It is worth to mention here that the matrix  $\hat{P}$  constructed according to Eqs. 3.23, 3.24, 3.25 satisfies the detailed balance condition:  $P_{kj} p_k^* = P_{jk} p_j^*$ . The transition probability matrix should satisfy this condition in order to produce a stationary probability distribution. So, the repeated actions of the matrix  $\hat{P}$  drives the probability distribution to the equilibrium.

The Metropolis algorithm can be generalized to the case of continuous variables, which means that instead of the vector  $\mathbf{p}^*$  we use now the function  $p^*(x)$ . In this case, to generate a random move one can use the continuous transition matrix  $W(x_{fin}, x_{in})$  where  $x_{fin}$  is given by

$$x_{fin} = x_{in} + D(2z - 1), \quad (3.26)$$

where  $D$  is an arbitrary constant and  $z$  is a random variable sampled from an uniform probability distribution. Suppose that at the initial time the system can be characterized by a vector  $\mathbf{x}_{in}$ , which contains the coordinates of all particles (as it was already mentioned, this quantity is called a walker). The

easiest version of the Metropolis algorithm for continuous variables can be written as follows:

1. generate a random vector  $\mathbf{z}$  from an uniform distribution
2. make an attempt move  $x_{in} \rightarrow x_{fin}$
3. if  $p^*(x_{fin}) \geq p^*(x_{in})$  then go to step 5
4. if  $p^*(x_{fin}) < p^*(x_{in})$  the new position  $x_{fin}$  can be accepted with the probability  $p(x_{fin})/p(x_{in})$  meaning that one needs to do the following test:
  - i) generate a new random number  $z'$  from an uniform distribution
  - ii) if  $p(x_{fin})/p(x_{in}) > z'$  then go to step 5
  - iii) if  $p(x_{fin})/p(x_{in}) \leq z'$  the proposed position  $\mathbf{x}_{fin}$  is not accepted and we need to put  $x_{fin} = x_{in}$
5. the new state is  $x_{fin}$

After many repetitions, we get a random number (vector)  $\mathbf{x}_{fin}$  sampled from the desired probability distribution  $p^*(x)$ .

It is important to mention the following. In the above algorithm the stationary probability distribution is considered. But in practice the Metropolis algorithm gives the stationary distribution only after some equilibration time, so in order to use the points sampled from  $p^*(\mathbf{x})$  one should wait an appropriate number of iterations. The parameter  $D$  influences the acceptance rate  $A$  of the random moves, which is defined as  $A = \frac{N_{ac}}{N_{tot}}$ , where  $N_{ac}$  is the number of accepted moves and  $N_{tot}$  is the total number of attempts. In principle  $D$  can be arbitrary, but if it is too small  $A$  is large, and many moves are needed to cover the whole space; on the contrary if  $D$  is too large  $A$  is small and the system is stuck in each position for a large number of iterations. In both cases the equilibration time becomes too long. Therefore, the appropriate value of  $D$  should be chosen empirically such that  $A = 0.5 - 0.7$ .

Another issue to address here is the number of walkers which is used in real simulations. As it was already mentioned the equilibrium random walk is an ergodic process, which, by definition, means that the temporal average can be replaced by the average on an ensemble. Therefore, we can use instead of a single walker some number  $N_w$  of uncorrelated walkers that perform random walks independently and then average over them to calculate observables.

## 3.4 Variational Monte Carlo

In this section we discuss the Variational Monte Carlo (VMC) method, which is based on the evaluation of multidimensional integrals using importance sampling guided by the Metropolis algorithm. Before going to the details of this method, a very important concept called the variational theorem should be introduced [89, 90]. It can be formulated as follows: "The expectation value of a Hamiltonian calculated using a trial wave function is always larger (or equal) than the ground-state energy calculated using the ground-state wave function". In other words it means that it is always possible to make an estimate of the ground-state energy without exact knowledge of the ground-state wave function. Below we prove this statement, which is rather straightforward.

Let  $E_T$  be the estimate of the energy calculated as the expectation value of the Hamiltonian  $\hat{H}$  with respect to a normalized trial wave function  $\Psi_T$ :

$$E_T = \langle \Psi_T | \hat{H} | \Psi_T \rangle = \int \Psi_T^* \hat{H} \Psi_T d\mathbf{R}. \quad (3.27)$$

The trial wave function  $\Psi_T$  can be expanded on the set of eigenfunctions of  $\hat{H}$  as  $\Psi_T = \sum_n a_n \Psi_n$ . Now Eq. (3.27) can be rewritten as:

$$\begin{aligned} E_T &= \int \left( \sum_n a_n^* \Psi_n^* \right) \hat{H} \left( \sum_m a_m \Psi_m \right) d\mathbf{R} = \\ &= \sum_n \sum_m a_n^* a_m \int \Psi_n^* \hat{H} \Psi_m d\mathbf{R} = \sum_n |a_n|^2 E_n, \end{aligned} \quad (3.28)$$

where  $E_n$  are the eigenstates of  $\hat{H}$ . Since  $E_0 \leq E_1 \leq E_2 \dots$  it is obvious that  $E_T \geq E_0$ . It is worth noticing here that the variational principle can be applied both to bosonic and fermionic systems. The trial wave functions that are used in QMC methods for bosonic and fermionic systems are described in Section 3.7.

The VMC method is directly based on the variational principle. The estimate of the ground-state energy  $E_{vmc}$  can be obtained as

$$E_{vmc} = \frac{\langle \Psi_T | \hat{H} | \Psi_T \rangle}{\langle \Psi_T | \Psi_T \rangle} = \frac{\int \Psi_T^* \hat{H} \Psi_T d\mathbf{R}}{\int \Psi_T^* \Psi_T d\mathbf{R}}, \quad (3.29)$$

where the denominator is added in order to generalize Eq. (3.27) to non-normalized trial wave functions. Here the vector  $\mathbf{R}$  contains  $d \cdot N$  coordinates, where  $d$  is the dimensionality and  $N$  is the number of particles of the system. For large  $N$  the calculation of the integrals in Eq. (3.27) using grid methods

becomes very ineffective, so the stochastic Variational Monte Carlo method is used.

As it was discussed in Section 3.2, a definite integral can be considered as a mean value over a probability distribution function. Therefore, let us rewrite (3.29) as

$$E_{vmc} = \frac{\int |\Psi_T|^2 \frac{\hat{H}\Psi_T}{\Psi_T} d\mathbf{R}}{\int \Psi_T^* \Psi_T d\mathbf{R}} = \int \rho(\mathbf{R}) E_L(\mathbf{R}) d\mathbf{R}, \quad (3.30)$$

where  $\rho(\mathbf{R}) = \frac{|\Psi_T|^2}{\int \Psi_T^* \Psi_T d\mathbf{R}}$  is the multivariate probability distribution function and  $E_L = \frac{\hat{H}\Psi_T}{\Psi_T}$  is the so called "local energy". Here it is important to notice that  $\rho(\mathbf{R})$ , defined in such way, is always positive and normalized to 1. So, in Eq. (3.30)  $\rho(\mathbf{R})$  is the pdf and  $E_L(\mathbf{R})$  is the function, which should be averaged over  $\rho(\mathbf{R})$ . Finally, the estimate of the variational energy can be written as

$$E_{vmc} = \frac{1}{N_w} \sum_{i=1}^{N_w} E_L(\mathbf{R}_i), \quad (3.31)$$

where  $\mathbf{R}_i$  are  $N_w$  random variables sampled from  $\rho(\mathbf{R})$ . The variance of Eq. (3.31) is

$$\sigma_{vmc}^2 = \frac{\sum_{i=1}^{N_w} E_L^2(\mathbf{R}_i)}{N_w^2} - \frac{E_{vmc}^2}{N_w}. \quad (3.32)$$

There is another way to estimate the VMC energy, which can be used to test the implementation of the calculation of the trial function in the algorithm. It is based on integration by parts in Eq. (3.29). Let us rewrite the expression for the kinetic energy part of  $E_{vmc}$  in the following way:

$$\int_V \Psi_T(\mathbf{R}) \nabla^2 \Psi_T(\mathbf{R}) d\mathbf{R} = \int_V \nabla (\Psi_T^*(\mathbf{R}) \nabla \Psi_T(\mathbf{R})) - \int_V \nabla \Psi_T^*(\mathbf{R}) \nabla \Psi_T(\mathbf{R}) d\mathbf{R}, \quad (3.33)$$

where  $V$  is the volume of the simulation box. The first term in the right part of Eq. (3.33) can be rewritten as the integral over the surface of  $V$ :

$$\int_V \nabla (\Psi_T^*(\mathbf{R}) \nabla \Psi_T(\mathbf{R})) = \int_S \Psi_T^*(\mathbf{R}) \nabla \Psi_T(\mathbf{R}) d\mathbf{S} = 0. \quad (3.34)$$

The expression (3.34) is equal to zero because the trial wave function is chosen to have zero derivatives at the surface of the simulation box. The variational energy can be estimated as follows:

$$E_{vmc}^F = \int \rho(\mathbf{R}) E_L^F(\mathbf{R}) d\mathbf{R}, \quad (3.35)$$

where  $\rho(\mathbf{R})$  is the same as in (3.29) and

$$E_L^F(\mathbf{R}) = \frac{\nabla\Psi_T^*(\mathbf{R})}{\Psi_T^*(\mathbf{R})} \frac{\nabla\Psi_T(\mathbf{R})}{\Psi_T(\mathbf{R})} + V(\mathbf{R}). \quad (3.36)$$

The local energy  $E_L^F$  is called the "force" estimator, because it can be rewritten in terms of the "quantum force"  $\mathbf{F}_Q = 2\frac{\nabla\Psi_T(\mathbf{R})}{\Psi_T(\mathbf{R})}$  as

$$E_L^F(\mathbf{R}) = \frac{|\mathbf{F}_Q(\mathbf{R})|^2}{4} + V(\mathbf{R}). \quad (3.37)$$

It is very useful to use both direct and force estimaties of the energy since after statistical average they should agree within error bars providing therefore a test of the implementation of the alghorithm. Finally, it is worth noticing that the force estimator gives a larger variance compared to the direct one. This fact can be understod from the arguments below. If  $\Psi_T(\mathbf{R})$  is the exact ground-state wave function, the direct estimator  $E_L(\mathbf{R})$  provides the exact value of the ground-state energy with zero variance. However, the force estimator  $E_L^F(\mathbf{R})$  gives an estimate for the ground-state energy with a non-zero variance due to the term  $V(\mathbf{R})$ .

Let us now consider how to sample  $\mathbf{R}_i$  from the probability distribution  $\rho(\mathbf{R})$ . The transition matrix  $W(x_{fin}, x_{in})$  for the Metropolis algorithm is chosen to be a Gaussian

$$W(\mathbf{R}_{in} \rightarrow \mathbf{R}_{fin}) = \frac{1}{(2\pi\alpha)^{dN/2}} \exp\left(-\frac{|\mathbf{R}_{in} - \mathbf{R}_{fin}|^2}{2\alpha}\right), \quad (3.38)$$

where  $\alpha$  is the variance of the Gaussian distribution. The acceptance probability of the move  $\mathbf{R}_{in} \rightarrow \mathbf{R}_{fin}$  is provided by

$$\min\left(1, \frac{|\Psi_T(\mathbf{R}_{fin})|^2}{|\Psi_T(\mathbf{R}_{in})|^2}\right). \quad (3.39)$$

A more sophisticated version of VMC, which guarantees faster convergence to the ground-state, is called Smart VMC (SVMC) [91], [92]. It is based on the use of the improved transition matrix which reads as

$$W_{smart}(\mathbf{R}_{in} \rightarrow \mathbf{R}_{fin}) = \frac{1}{(4\pi D\tau)^{dN/2}} \exp\left(-\frac{|\mathbf{R}_{in} + 4D\mathbf{F}_Q(\mathbf{R}_{in}) - \mathbf{R}_{fin}|^2}{4D\tau}\right), \quad (3.40)$$

where  $D = \frac{\hbar^2}{2m}$ , and  $\tau$  is the imaginary time. This method shares some analogies (such as the dependence of  $W_{smart}(\mathbf{R}_{in} \rightarrow \mathbf{R}_{fin})$  on  $\mathbf{F}_Q$  and  $\tau$ ) with the Diffusion Monte Carlo, which is described in the next section. It is important to mention here that the transition matrix  $W_{smart}(\mathbf{R}_{in} \rightarrow \mathbf{R}_{fin})$  is not symmetric relative to the exchange between  $\mathbf{R}_{in}$  and  $\mathbf{R}_{fin}$ . Therefore the

acceptance probability for the Metropolis test should not be calculated using Eq. (3.39), but instead using the expression described in the next section for the DMC method. Finally, let us mention that the use of SVMC helps to check if the quantum force is implemented correctly in the code, because SVMC should give the same results as usual VMC (within error bars).

At the end of this section, let us discuss a very important issue of the optimization of the trial wave function. It is obvious, that the closer  $\Psi_T$  is to the real ground-state wave function, the lower the variational energy. So, it is necessary to find the set of parameters defining the trial wave function which correspond to the minimum of  $E_{vmc}$ . In the case of only one variational parameter  $a$ , the procedure is rather straightforward: one needs to get  $E_{vmc}$  as a function of  $a$  and find the global minimum (for an example, see Section 4.3.2). If  $\Psi_T$  depends on several variational parameters  $a_1, a_2, a_3, \dots$ , the task becomes more complicated as one needs to find the global minimum of a function of several variables. The most straightforward way here is to use standard numerical procedures such as conjugate gradient methods [86]. More sophisticated methods of optimization were developed, for example, by S. Sorella in [93].

### 3.5 Diffusion Monte Carlo

In this section we discuss a more advanced Monte Carlo method called Diffusion Monte Carlo (DMC) [94, 95]. This method solves the imaginary time Schroedinger equation using the analogy with a classical diffusion equation. For bosonic system the DMC method gives the exact ground-state energy apart from statistical uncertainty. This means that one can reach a desired error in the determination of the ground-state energy simply by increasing the number of statistically independent walkers. Another great advantage of DMC is that the estimate of energy does not depend so strongly on the quality of the trial wave function. In practice, the optimization of the wave function reduces the variance of the energy estimate, but it has almost no influence on its value. Unfortunately, for fermionic systems DMC is not able to provide an exact estimate of the ground-state energy, it gives only an upper bound. The treatment of fermionic systems is discussed in the next section in more details.

We are interested in the stationary solution of the Schroedinger's equation

$$-i\hbar \frac{\partial \Psi(\mathbf{R}, t)}{\partial t} = \hat{H} \Psi(\mathbf{R}, t). \quad (3.41)$$

The formal solution of (3.41) can be written as the expansion on eigenstates

$\{\Phi_n(\mathbf{R})\}$  of  $\hat{H}$

$$\Psi(\mathbf{R}, t) = \sum_{n=0}^{\infty} c_n \Phi_n(\mathbf{R}) \exp(-iE_n t), \quad (3.42)$$

where  $E_n$  are the eigenvalues of  $\hat{H}$ , and  $c_n$  are some constants. The oscillatory behavior of Eq. (3.42) becomes an exponential decay if the real time  $t$  is substituted by the imaginary time  $\frac{\tau}{\hbar}$ . So, the Schroedinger's equation (3.41) is rewritten as

$$-\frac{\partial \Psi(\mathbf{R}, \tau)}{\partial \tau} = \hat{H} \Psi(\mathbf{R}, \tau), \quad (3.43)$$

which has the solution

$$\Psi(\mathbf{R}, \tau) = \sum_{n=0}^{\infty} c_n \Phi_n(\mathbf{R}) \exp(-\tau E_n). \quad (3.44)$$

For large imaginary times  $\tau$  only the ground state eigenfunction contributes to Eq. (3.44), because it has the smallest eigenvalue  $E_0$  and Eq. (3.44) becomes

$$\Psi(\mathbf{R}, \tau \rightarrow \infty) = c_0 \Phi_0(\mathbf{R}) \exp(-\tau E_0). \quad (3.45)$$

The stationary solution of Schroedinger's equation can be found from the large  $\tau$  limit in imaginary time of its non stationary solution.

Let us explore the analogy between the imaginary time Schroedinger's equation (3.43) and a classical diffusion equation Eq. (3.43) is explicitly written as

$$\frac{\partial \Psi(\mathbf{R}, \tau)}{\partial \tau} = D \nabla^2 \Psi(\mathbf{R}, \tau) + (E_T - V(\mathbf{R})) \Psi(\mathbf{R}, \tau), \quad (3.46)$$

where  $D = \frac{\hbar^2}{2m}$  is the so called "diffusion constant" and  $E_T$  is a reference energy which is introduced to stabilize the algorithm. Without the second term on the right-hand part, Eq. (3.46) coincides with the classical diffusion equation. On the contrary, without the first term Eq. (3.46) becomes a first-order branching equation whose "rate constant" is  $E_T - V$ . The imaginary time Schroedinger's equation can be simulated by a combined stochastic process consisting of diffusion in configuration space plus branching process, which means the change of the number of walkers (called "population") during the simulation.

Equation (3.46) has a disadvantage for simulating the branching process because the branching rate can become too small or too large, depending on the value  $V(\mathbf{R})$ , that would lead to large fluctuations of the population. The importance sampling technique, discussed in Section 3.2, is used to avoid this problem. In this approach the following substitution is used

$$f(\mathbf{R}, \tau) = \Psi_T(\mathbf{R}) \Psi(\mathbf{R}, \tau), \quad (3.47)$$

where  $\Psi_T(\mathbf{R})$  is a trial wave function which is used to bias the random walk to produce the distribution  $f(\mathbf{R}, \tau)$ . The trial wave function is usually constructed based on the available knowledge about the physical system under consideration. Eq. (3.46) then becomes

$$\frac{\partial f(\mathbf{R}, \tau)}{\partial \tau} = D\nabla^2(f(\mathbf{R}, \tau)\mathbf{F}_Q(\mathbf{R})) + (E_T - E_L(\mathbf{R}))f(\mathbf{R}, \tau), \quad (3.48)$$

where the local energy  $E_L(\mathbf{R}) = \frac{\hat{H}\Psi_T(\mathbf{R})}{\Psi_T(\mathbf{R})}$  and the quantum force  $\mathbf{F}_Q(\mathbf{R}) = 2\frac{\nabla\Psi_T(\mathbf{R})}{\Psi_T(\mathbf{R})}$  are the same quantities introduced already when discussing the VMC method. The meaning of the quantum force is the effective velocity of the walkers. It is directed away from the regions where  $\Psi_T(\mathbf{R})$  is small. In classical Brownian motion the same role is played by the gradient of the external field.

Another important property of Eq. (3.48) is the appearance of the term  $E_T - E_L(\mathbf{R})$  instead of  $E_T - V(\mathbf{R})$ . The local energy  $E_L(\mathbf{R})$  is much smoother than the potential energy  $V(\mathbf{R})$ , because  $E_L(\mathbf{R})$  has contributions both from potential and kinetic energy operators. Therefore, the branching process is much more stable, than without the use of the importance sampling technique.

The main goal of the DMC technique is the evaluation of  $f(\mathbf{R}, \tau)$  according to Eq. (3.48) up to large enough imaginary time such that the contributions from the excited states in Eq. (3.44) would die out. For that purpose the differential equation (3.48) should be rewritten as an integral equation using the Green's function formalism.

Let us define the operator  $\hat{O}$  such that

$$\hat{O} = \hat{K}' + E_L(\mathbf{R}) - E_T, \quad (3.49)$$

where  $\hat{K}' = -D\nabla^2 + D(\nabla\mathbf{F}_Q(\mathbf{R}) + \mathbf{F}_Q(\mathbf{R})\nabla)$  is the modified kinetic energy operator. Using the operator  $\hat{O}$  the equation (3.48) becomes

$$-\frac{\partial f(\mathbf{R}, \tau)}{\partial \tau} = \hat{O}f(\mathbf{R}, \tau) \quad (3.50)$$

and the formal solution can be written as

$$f(\mathbf{R}', \tau) = \int G(\mathbf{R}', \mathbf{R}, \tau)f(\mathbf{R}', 0)d\mathbf{R}. \quad (3.51)$$

Here  $G(\mathbf{R}', \mathbf{R}, \tau)$  is the Green's function of the operator  $\hat{O}$  defined as

$$G(\mathbf{R}', \mathbf{R}, \tau) = \langle \mathbf{R}' | \exp(-\hat{O}\tau) | \mathbf{R} \rangle. \quad (3.52)$$

The exact form of the Green's function is not normally known, but a reliable approximation at small time-step can be obtained. The propagation in imaginary time can be performed as follows:

$$f(\mathbf{R}', \tau + \Delta\tau) = \int G(\mathbf{R}', \mathbf{R}, \Delta\tau)f(\mathbf{R}', \tau)d\mathbf{R} \quad (3.53)$$

We discuss now the approximate form of the Green's function that is used in the DMC method. For pedagogical purpose we firstly consider the Green's function corresponding to Eq. (3.46) which is denoted as  $G_0(\mathbf{R}', \mathbf{R}, \Delta\tau)$ . It is defined as

$$G_0(\mathbf{R}', \mathbf{R}, \tau) = \langle \mathbf{R}' | \exp \left( -\hat{K} - (\hat{V} - E_T)\tau \right) | \mathbf{R} \rangle, \quad (3.54)$$

where  $\hat{K} = D\frac{\nabla^2}{2m}$  is the usual operator of the kinetic energy. The main obstacle in finding the exact form of the Green's function  $G_0(\mathbf{R}', \mathbf{R}, \tau)$  is the non-commutativity of the operators  $\hat{K}$  and  $\hat{V}$ . For small times  $\Delta\tau$  the function  $G_0(\mathbf{R}', \mathbf{R}, \Delta\tau)$  approximately becomes

$$G_0(\mathbf{R}', \mathbf{R}, \Delta\tau) \simeq G_K(\mathbf{R}', \mathbf{R}, \Delta\tau)G_V(\mathbf{R}', \mathbf{R}, \Delta\tau) + O(\Delta\tau^2), \quad (3.55)$$

where  $G_K(\mathbf{R}', \mathbf{R}, \Delta\tau) = \exp \left( -\hat{K}\Delta\tau \right)$  and  $G_V(\mathbf{R}', \mathbf{R}, \Delta\tau) = \exp \left( -\hat{V}\Delta\tau \right)$ . So, in order to construct  $G_0(\mathbf{R}', \mathbf{R}, \Delta\tau)$  one needs to know only the Green's function of the operators of kinetic and potential energy separately. Namely

$$G_K(\mathbf{R}', \mathbf{R}, \Delta\tau) = \frac{\exp \left( (\mathbf{R}' - \mathbf{R})^2 / 2D\Delta\tau \right)}{(4\pi D\Delta\tau)^{-3N/2}}, \quad (3.56)$$

where  $N$  is the number of particles, and

$$G_V(\mathbf{R}', \mathbf{R}, \Delta\tau) = \exp \left( -(1/2[V(\mathbf{R}) + V(\mathbf{R}')] - E_T)\Delta\tau \right), \quad (3.57)$$

The Green's function  $G(\mathbf{R}', \mathbf{R}, \Delta\tau)$  of the Eq. (3.48) can be constructed analogously to  $G_0(\mathbf{R}', \mathbf{R}, \tau)$ . More precisely, if  $\Delta\tau$  is small it can be written as

$$G(\mathbf{R}', \mathbf{R}, \Delta\tau) \simeq G_{K'}(\mathbf{R}', \mathbf{R}, \Delta\tau)G_B(\mathbf{R}', \mathbf{R}, \Delta\tau) + O(\Delta\tau^2), \quad (3.58)$$

where  $G_{K'}(\mathbf{R}', \mathbf{R}, \tau)$  is the Green's function of the modified kinetic energy operator  $\hat{K}'$  which governs the diffusion process and  $G_B(\mathbf{R}', \mathbf{R}, \tau)$  is the Green's function responsible for the branching of walkers. The last part can be obtained simply by the change of  $V(\mathbf{R})$  with  $E_L(\mathbf{R})$  in Eq. (3.57) which gives

$$G_B(\mathbf{R}', \mathbf{R}, \Delta\tau) = \exp \left( - \left[ \frac{E_L(\mathbf{R}) + E_L(\mathbf{R}')}{2} - E_T \right] \Delta\tau \right). \quad (3.59)$$

The Green's function  $G_{K'}(\mathbf{R}', \mathbf{R}, \tau)$  can be found assuming that  $\mathbf{F}_Q$  remains constant during the random move  $\mathbf{R}' \rightarrow \mathbf{R}$  and it takes the form

$$G_{K'}(\mathbf{R}', \mathbf{R}, \Delta\tau) = \frac{\exp \left( (\mathbf{R}' - \mathbf{R} - D\Delta\tau\mathbf{F}_Q)^2 / 4D\Delta\tau \right)}{(4\pi D\Delta\tau)^{-3N/2}}. \quad (3.60)$$

The above assumption is satisfied better and better as  $\Delta\tau \rightarrow 0$ . Therefore an extrapolation to  $\Delta\tau = 0$  is required.

The ground-state energy  $E_0$  can be estimated using the following mixed matrix element:

$$E_0 = \frac{\int \Psi_T^*(\mathbf{R}) \hat{H} \Phi_0(\mathbf{R}) d\mathbf{R}}{\int \Psi_T^*(\mathbf{R}) \Phi_0(\mathbf{R}) d\mathbf{R}}. \quad (3.61)$$

The above expression can be rewritten in the suitable form for the Monte Carlo method as

$$E_0 = \int E_L(\mathbf{R}) \rho_{DMC}(\mathbf{R}), \quad (3.62)$$

where the local energy is exactly the same as in the VMC method, but the probability distribution  $\rho_{DMC}(\mathbf{R})$  is different

$$\rho_{DMC}(\mathbf{R}) = \frac{\Psi_T(\mathbf{R}) \Phi_0(\mathbf{R})}{\int \Psi_T(\mathbf{R}) \Phi_0(\mathbf{R}) d\mathbf{R}} = \frac{f(\mathbf{R}, \tau \rightarrow \infty)}{\int f(\mathbf{R}, \tau \rightarrow \infty) d\mathbf{R}}. \quad (3.63)$$

The last equality is based on (3.47) and (3.45). Finally, Eq. (3.62) can be estimated as the mean of the local energies  $E_L(\mathbf{R})$  calculated for the set of configurations  $\{\mathbf{R}_i\}$  distributed according to the stationary probability distribution  $f(\mathbf{R}, \tau \rightarrow \infty)$ :

$$E_0 = \frac{1}{N_w} \sum_{i=1}^{N_w} E_L(\mathbf{R}_i), \quad (3.64)$$

where  $N_w$  is the number of statistically independent walkers  $\mathbf{R}_i$ .

As it was discussed in Section 3.3, the transition probability function for a Markov process must satisfy the detailed balance condition in order to guarantee the existence of a stationary distribution. It is clear that  $G_{K'}(\mathbf{R}', \mathbf{R}, \Delta\tau)$  violates this condition because

$$G_{K'}(\mathbf{R}', \mathbf{R}, \Delta\tau) \neq G_{K'}(\mathbf{R}, \mathbf{R}', \Delta\tau). \quad (3.65)$$

In order to compensate for it, a Metropolis step is introduced with the acceptance probability

$$A(\mathbf{R}', \mathbf{R}, \Delta\tau) = \min(1, q(\mathbf{R}', \mathbf{R}, \Delta\tau)), \quad (3.66)$$

where

$$q(\mathbf{R}', \mathbf{R}, \Delta\tau) = \frac{|\Psi_T(\mathbf{R}')|^2 G(\mathbf{R}, \mathbf{R}', \tau)}{|\Psi_T(\mathbf{R})|^2 G(\mathbf{R}', \mathbf{R}, \tau)}. \quad (3.67)$$

It is worth noticing here that the effective time step changes when some number of proposed moves are rejected. Therefore it is necessary to determine the proper time step to use in Eq. (3.67).

At the end of this section let us write schematically our implementation of the DMC algorithm.

1. Choose the trial wave function  $\Psi_T(\mathbf{R})$ .

2. Do the optimization of the variational parameters in  $\Psi_T(\mathbf{R})$  using VMC.
3. Using the optimized parameters of  $\Psi_T(\mathbf{R})$  perform a short VMC run in order to prepare the starting configuration  $\{\mathbf{R}\}$  for DMC evolution. Usually it contains approximately 200 walkers.
4. Calculate the energy of the initial configuration averaged over all starting walkers. This energy is used as the reference energy  $E_T$  for the first iteration of DMC evolution.
5. Start the loop over all walkers  $i = 1, \dots, N_w$ , where  $N_w$  is the total number of walkers (which will change during the time evolution).

i) Gaussian jump + drift move

For walker  $i$  choose the new position  $\mathbf{R}'$  based on Eq. (3.60). More precisely, for every particle  $j$  from walker  $i$

$$\mathbf{r}'_j = \mathbf{r}_j + D\Delta\tau\mathbf{F}_Q^j(\mathbf{R}) + \boldsymbol{\xi}_j, \quad (3.68)$$

where  $\boldsymbol{\xi}_j$  is sampled from the Gaussian distribution  $\frac{\exp(-\boldsymbol{\xi}_j^2/4D\delta\tau)}{(4\pi D\delta\tau)^{3N/2}}$ .

ii) Metropolis test

Do the Metropolis test according to Eq. (3.66). It is worth stressing here that in the present implementation of DMC the Metropolis step is performed after the move of all particles of a given walker. Another possibility is to do it after moving each of the particles.

iii) Branching

If the random move is accepted calculate the number of sons  $n_{sons}$  for each walker according to Eq. (3.59) as

$$n_{sons} = Integer(\exp(E_T - [E_L(\mathbf{R}) + E_L(\mathbf{R}')])\Delta\tau_{eff}) + \chi, \quad (3.69)$$

where  $\chi$  is a random number sampled from the uniform distribution,  $\Delta\tau_{eff}$  is the effective time step corrected by the acceptance rate  $A$  as  $\Delta\tau_{eff} = \Delta\tau * A$ . For the first iteration  $\Delta\tau_{eff} = \Delta\tau$ . Number of sons can be equal to 0, 1, 2, .... Pass the configuration  $\mathbf{R}'$  and the energy to all sons of the walker. If  $n_{sons} = 0$  it means that the walker is killed.

6. At the end of the loop over all walkers calculate the average energy and update the value of  $E_T$ .
7. Proceed to the new iteration. The new number of walkers is

$$f_w^i = \sum_{j=1}^{N_w(i-1)} n_{sons}(j). \quad (3.70)$$

The value of energy can be biased by the finite time step  $\Delta\tau$  and by the average number of walkers  $\langle N_w \rangle$ . In order to get an unbiased value of the energy it is necessary to make the extrapolation to  $\Delta\tau = 0$  and to  $\langle N_w \rangle \rightarrow \infty$ .

Another important issue is that the sampling of random numbers must not be correlated during the whole simulation. The standard function of C programming language, such as `rand()`, does not satisfy this condition. Therefore, more sophisticated algorithms such as `ran2` or `ran3` from [86] must be used in the code.

The above discussed implementation of the DMC algorithm can be relatively easily parallelized (usually each processor makes calculation for some number of walkers). In this case it is important to be sure that the sampling of random numbers realized by different processors are not correlated between each other.

Finally let us mention that one can choose the approximate Green's function accurate up to  $O(\tau^3)$  [96] as

$$G_{quad}(\mathbf{R}', \mathbf{R}, \Delta\tau) = (4\pi D\tau)^{-3N/2} \exp\left(-\frac{1}{2}(E_L(\mathbf{R}) + E_L(\mathbf{R}')) - E_T\right)\tau \\ \times \exp\left(\frac{(\mathbf{R}' - \mathbf{R} - D\delta\tau(\mathbf{F}_Q(\mathbf{R})\mathbf{F}_Q(\mathbf{R}')))^2}{4D\tau}\right) \det\{\hat{I} - D\delta\tau\hat{H}(\mathbf{R}')\},$$

where  $\hat{I}$  is the unity matrix and  $\hat{H}$  is the matrix constructed from derivatives of the quantum force  $\mathbf{F}_Q$  as

$$H_{pq} = \frac{\partial^2}{\partial F_Q^p \partial F_Q^q} (2 \ln \Psi_T(\mathbf{R})).$$

### 3.6 Diffusion Monte Carlo for fermions

As it was already discussed in the previous section the product  $\Psi_T(\mathbf{R})\Phi_0(\mathbf{R})$ , which plays the role of a probability distribution, must always be positively defined in the DMC method. For bosons this requirement is easily satisfied, because  $\Phi_0(\mathbf{R})$  is always positively defined. It is then enough to choose  $\Psi_T(\mathbf{R})$  positively defined. For fermionic systems instead the famous "sign problem" immediately arises from the fact, that the ground state of fermions has nodes, meaning that the product  $\Psi_T(\mathbf{R})\Phi_0(\mathbf{R})$  can be negative.

Nevertheless there is possibility to use the DMC method for fermions using the fixed-node approximation, which was introduced in [61], [97]. Below we discuss this approximation, but two important definitions should be introduced before. The "nodal surface" is the region in configuration space where the trial wave function  $\Psi_T(\mathbf{R})$  is equal to zero. A "nodal pocket" is a region where  $\Psi_T(\mathbf{R})$  has a well-defined sign. The main problem is that the nodal surface of  $\Phi_0(\mathbf{R})$  is usually unknown.

The main idea of the fixed-node approximation is to use  $\Psi_T(\mathbf{R})\Phi_0^{FN}(\mathbf{R})$  instead of  $\Psi_T(\mathbf{R})\Phi_0(\mathbf{R})$  where the nodal surface of  $\Phi_0^{FN}(\mathbf{R})$  is equal to the nodal surface of the trial wave function. In practice, it means that if for a given walker  $\Psi_T(\mathbf{R})$  is positive (negative) at the beginning of the simulation, then it always remains positive (negative). So, one gets the following estimate of the ground-state energy

$$E_0^{FN} = \int E_L(\mathbf{R})\rho_{DMC}^{FN}(\mathbf{R}), \quad (3.71)$$

where the probability distribution  $\rho_{DMC}^{FN}(\mathbf{R})$  is

$$\rho_{DMC}^{FN}(\mathbf{R}) = \frac{\Psi_T(\mathbf{R})\Phi_0^{FN}(\mathbf{R})}{\int \Psi_T(\mathbf{R})\Phi_0^{FN}(\mathbf{R})d\mathbf{R}}. \quad (3.72)$$

This approximation can be implemented very easily in the algorithm, because the action of the quantum force is such that a walker is always pushed away from the boundary of a pocket. Therefore, for small enough time step the walker never crosses it.

Fixed-node DMC is a variational method with respect to the nodal surface of the many-body wave function, which means that  $E_0^{FN}$  is an upper bound to the ground-state energy.

## 3.7 Trial wave functions

In this section we discuss the basic trial wave functions that are usually used in QMC simulations.

Trial wave functions for bosons are usually chosen to be of the Jastrow form [54]

$$\Psi_J(\mathbf{R}) = \prod_{i<j} f(r_{ij}), \quad (3.73)$$

where  $f(r_{ij})$  is a non-negative two-body correlation term.

For fermions a Jastrow wave function alone can not be used because the many-body wave function must be antisymmetric with respect to particle exchange [90]. The way to construct such a wave function is based on the use of Slater matrices [98]. For two-dimensional non-interacting fermions in a square with size  $L$  Slater determinant is given by

$$\Delta_S = \begin{bmatrix} e^{i\mathbf{k}_1\mathbf{r}_1} & e^{i\mathbf{k}_1\mathbf{r}_2} & \dots & e^{i\mathbf{k}_1\mathbf{r}_N} \\ e^{i\mathbf{k}_2\mathbf{r}_1} & \ddots & & \vdots \\ \vdots & \ddots & & \vdots \\ e^{i\mathbf{k}_N\mathbf{r}_1} & \dots & \dots & e^{i\mathbf{k}_N\mathbf{r}_N} \end{bmatrix}$$

Here  $\mathbf{k}_\alpha = (2\pi/L)(n_\alpha^x, n_\alpha^y)$  with  $n_\alpha^{x,y} = 0, \pm 1, \pm 2, \dots$  are the wave vectors complying with periodic boundary conditions. According to Fermi liquid theory [99], [100] a one-to-one mapping is assumed between the low-lying excitations of interacting and noninteracting fermions. Therefore the use of  $\Delta_S$  is possible for interacting systems also. Nevertheless, in order to take into account interactions between fermions a product of a Slater determinant and a Jastrow wave function is used. Such an expression is called Slater-Jastrow wave function and within QMC calculations it was introduced in [56]. For VMC calculations the optimization of the orbitals of the Slater determinant and of the Jastrow term is crucial in order to get the lower energies. For FNDMC simulations only nodal surface is important. The nodal surface of the non-interacting Slater determinant is the zeroth order approximation for an interacting Fermi gas. In many cases this approximation is enough to get good QMC results that agree with experiments [71], [102]. However, in some strongly correlated systems such as  $^3\text{He}$ , it is necessary to introduce back-flow corrections to the orbitals in the determinant to improve the nodal surface. Such corrections were used in the content of cold atoms in Ref. [103].

### 3.8 Correlation functions

Quantum Monte Carlo methods can be used to calculate not only the ground-state energy of the system, but also other important one- and two-body quantities such as the pair-distribution function, the one-body density matrix, the static structure factor and the momentum distribution. All of them can be written in a way suitable for Monte-Carlo integrals as

$$O_{MC} = \int O_L(\mathbf{R})\pi(\mathbf{R})d\mathbf{R}, \quad (3.74)$$

where  $O_{MC}$  is the Monte-Carlo estimate of the expectation value of the operator  $\hat{O}$ ,  $O_L(\mathbf{R}) = \frac{\hat{O}\Psi_T(\mathbf{R})}{\Psi_T(\mathbf{R})}$  is the local value of the operator  $\hat{O}$ ,  $\pi(\mathbf{R})$  is a probability distribution. In case of the Diffusion Monte Carlo method at  $\tau \rightarrow \infty$  the probability distribution  $\pi(\mathbf{R})$  approaches the limit provided by Eq. (3.63). In this case Eq. (3.74) corresponds to the mixed estimator

$$\langle \hat{O} \rangle_{DMC} = \frac{\int \Phi_0(\mathbf{R})\hat{O}\Psi_T(\mathbf{R})d\mathbf{R}}{\int \Phi_0(\mathbf{R})\Psi_T(\mathbf{R})d\mathbf{R}} = \frac{\int \Phi_0(\mathbf{R})\Psi_T(\mathbf{R})O_{loc}(\mathbf{R})d\mathbf{R}}{\int \Phi_0(\mathbf{R})\Psi_T(\mathbf{R})d\mathbf{R}}. \quad (3.75)$$

In general, the mixed estimator  $\langle \hat{O} \rangle_{DMC}$  is biased by the trial wave function  $\Psi_T$  used for importance sampling. Only in case, when the operator  $\hat{O}$  is the Hamiltonian or commutes with the Hamiltonian Eq. (3.75) gives the exact

expectation value of  $\hat{O}$ , which is called a pure estimator

$$\langle \hat{O} \rangle_p = \frac{\int \Phi_0(\mathbf{R}) \hat{O} \Phi_0(\mathbf{R}) d\mathbf{R}}{\int \Phi_0(\mathbf{R}) \Phi_0(\mathbf{R}) d\mathbf{R}}. \quad (3.76)$$

The standard way [104] to correct this bias is to calculate also the VMC estimator

$$\langle \hat{O} \rangle_{VMC} = \frac{\int \Psi_T(\mathbf{R}) \hat{O} \Psi_T(\mathbf{R}) d\mathbf{R}}{\int \Psi_T(\mathbf{R}) \Psi_T(\mathbf{R}) d\mathbf{R}}, \quad (3.77)$$

and to use the extrapolation

$$\langle \hat{O} \rangle_{extr} = 2\langle \hat{O} \rangle_{DMC} - \langle \hat{O} \rangle_{VMC}. \quad (3.78)$$

The equation (3.78) can be easily obtained by the following procedure. Suppose, that the trial wave function  $\Psi_T$  is a good approximation of the ground state  $\Phi_0$ . In this case one can write  $\Phi_0 = \Psi_T + \delta\Psi$  and the pure estimator (3.76) can be written as

$$\langle \hat{O} \rangle_p = \frac{\int (\Psi_T + \delta\Psi) \hat{O} (\Psi_T + \delta\Psi) d\mathbf{R}}{\int (\Psi_T + \delta\Psi)(\Psi_T + \delta\Psi) d\mathbf{R}} \simeq 2\langle \hat{O} \rangle_{DMC} - \langle \hat{O} \rangle_{VMC} = \langle \hat{O} \rangle_{extr}. \quad (3.79)$$

Finally, let us mention that the pure estimator (3.76) for local operators can be calculated directly in the DMC algorithm using the forward walking technique [105].

Let us discuss the details of the MC calculation of the correlation functions that were mentioned above for an one-component system (which means that we do not consider spin degrees of freedom). We consider only mixed estimators, since variational estimators can be easily obtained from the mixed ones by replacing  $\Phi_0$  by  $\Psi_T$ . An important quantity, which contains a wealth of information about the ground state, is the pair-correlation function  $g(\mathbf{x})$ . This function describes the density fluctuations in the gas and is proportional to the probability of having two particles at the distance  $x$  between them. In the second quantization formalism it is defined as

$$g(\mathbf{x}) = \frac{1}{n^2} \langle \hat{\Psi}^+(\mathbf{r}) \hat{\Psi}^+(\mathbf{r} + \mathbf{x}) \hat{\Psi}(\mathbf{r} + \mathbf{x}) \hat{\Psi}(\mathbf{r}) \rangle, \quad (3.80)$$

where  $\hat{\Psi}^+$  and  $\hat{\Psi}(\mathbf{r})$  are the standard creation and annihilation field operators and  $n$  is the density. The expression (3.80) describes the process of removing two particles from position  $\mathbf{r}$  and  $\mathbf{r} + \mathbf{x}$ , returning back to the same state after replacing the particles in the same positions.

It is more convenient for MC calculations to write Eq. (3.80) in terms of wave functions as

$$g(x) = \frac{\frac{2}{n^2\Omega_d} \sum_{i<j}^N \int d\Omega_x \int \Psi_T(\mathbf{r}_i, \mathbf{r}_j = \mathbf{r}_i + \mathbf{x}, \mathbf{R}) \Phi_0(\mathbf{r}_i, \mathbf{r}_j = \mathbf{r}_i + \mathbf{x}, \mathbf{R}) d\mathbf{R}}{\int \Psi_T(\mathbf{R}) \Phi_0(\mathbf{R}) d\mathbf{R}}, \quad (3.81)$$

where  $\Omega_x$  is the solid angle which corresponds to the displacement vector  $\mathbf{x}$ ,  $\Omega_d$  is the total solid angle in dimension  $d$ ,  $n$  is the density. Using the homogeneity of the system, it is possible to eliminate the integration over the solid angle  $\Omega_x$  in the expression (3.81) which can be rewritten as

$$\begin{aligned} g(x) &= \frac{\frac{2}{Nn\Omega_d x^d} \sum_{i<j}^N \int \delta(x - |\mathbf{r}_i - \mathbf{r}_j|) \Psi_T(\mathbf{r}_i, \mathbf{r}_j, \mathbf{R}) \Phi_0(\mathbf{r}_i, \mathbf{r}_j, \mathbf{R}) d\mathbf{R}}{\int \Psi_T(\mathbf{R}) \Phi_0(\mathbf{R}) d\mathbf{R}} = \\ &= \frac{2}{Nn\Omega_d x^d} \sum_{i<j}^N \int \delta(x - |\mathbf{r}_i - \mathbf{r}_j|) \rho_{DMC}(\mathbf{R}) d\mathbf{R}. \end{aligned} \quad (3.82)$$

The calculation of  $g(x)$  is very easy to implement in the MC code. At every iteration and for every walker the distance between all pairs of particles should be calculated. Then we need to count the number of distances which lie between  $x$  and  $x + dx$ . Averaging this number over all walkers gives us (in the three dimensional case) an estimate of  $(N/2n4\pi x^2 dx) g(x)$ . Usually, the pair-correlation function is normalized in such a way that it is equal to 1 for  $x \rightarrow \infty$ .

The one-body density matrix (OBDM) has the physical meaning of the amplitude of a process where one particle is removed from position  $\mathbf{r}$  and the same quantum many-body state is recovered by replacing the particle at position  $\mathbf{r}'$ . In terms of field operators  $\hat{\Psi}$  and  $\hat{\Psi}^+$  it reads

$$\varrho_{DMC}(\mathbf{r}, \mathbf{r}') = \langle \hat{\Psi}^+(\mathbf{r}) \hat{\Psi}(\mathbf{r}') \rangle. \quad (3.83)$$

For homogeneous systems where  $\mathbf{r}' = \mathbf{r} + \mathbf{x}$  the expression (3.83) becomes

$$\varrho_{DMC}(\mathbf{x}) = \langle \hat{\Psi}^+(0) \hat{\Psi}(\mathbf{x}) \rangle. \quad (3.84)$$

Analogously to the case of the pair-correlation function the expression (3.84) can be rewritten as

$$\begin{aligned} \varrho_{DMC}(x) &= \frac{\frac{1}{N\Omega_d} \sum_{i=1}^N \int d\Omega_x \int d\mathbf{R} \Phi_0(\mathbf{r}_1 \dots \mathbf{r}_i \dots \mathbf{r}_N) \Psi_T(\mathbf{r}_1 \dots \mathbf{r}_i + \mathbf{x} \dots \mathbf{r}_N)}{\int \Phi_0(\mathbf{R}) \Psi_T(\mathbf{R}) d\mathbf{R}} = \\ &= \frac{1}{N\Omega_d} \sum_{i=1}^N \int d\Omega_x \int d\mathbf{R} \rho_{DMC}(\mathbf{R}) \varrho_{DMC}^{loc}(\mathbf{R}, \mathbf{x}), \end{aligned} \quad (3.85)$$

where  $\varrho_{DMC}^{loc}(\mathbf{R}, \mathbf{x}) = \frac{\Psi_T(\mathbf{r}_1 \dots \mathbf{r}_i + \mathbf{x} \dots \mathbf{r}_N)}{\Psi_T(\mathbf{r}_1 \dots \mathbf{r}_i \dots \mathbf{r}_N)}$ ,  $\rho_{DMC}(\mathbf{R})$  is the DMC probability distribution (3.63),  $\Omega_x$  is the solid angle corresponding to the displacement vector  $\mathbf{x}$ ,  $\Omega_d$  is the total solid angle in dimension  $d$  and  $N$  is the number of particles.

The MC calculation of the OBDM was first performed by McMillan in Ref. [54] for a system of liquid  ${}^4He$ . Below we describe the main steps of McMillan algorithm. All the steps are supposed to be performed at each iteration.

- 1) Choose randomly the vector  $\mathbf{x}$
- 2) Choose randomly the index  $i$  and displace the  $i$ -th particle by the vector  $\mathbf{x}$  such that  $\mathbf{r}_i \rightarrow \mathbf{r}_i + \mathbf{x}$ .
- 3) Calculate the value  $quoc = \frac{\Psi_T(\mathbf{r}_1 \dots \mathbf{r}_i + \mathbf{x} \dots \mathbf{r}_N)}{\Psi_T(\mathbf{r}_1 \dots \mathbf{r}_i \dots \mathbf{r}_N)}$ , i. e. the ratio between the wave function that corresponds to the configuration before and after the displacement.
- 4) Add  $quoc$  to the bin  $dr$  of  $\varrho^{loc}$  corresponding to the modulus of the vector  $\mathbf{x}$ .
- 5) Repeat all steps 1-4 for a large enough number of iterations (around 100). It allows to perform the integration over  $\Omega_x$  and average over all  $N$  particles.

The OBDM is connected with the momentum distribution  $n(\mathbf{k})$  by a Fourier transform

$$n(\mathbf{k}) = \int \mathbf{x} \varrho(\mathbf{x}) \exp(i\mathbf{k}\mathbf{x}). \quad (3.86)$$

Using the expression for the OBDM (3.85) the momentum distribution can be written as

$$n(k) = \frac{1}{N\Omega_d} \int d\mathbf{R} \rho_{DMC}(\mathbf{R}) \sum_i^N \int d\Omega_k \int d\mathbf{x} \varrho_{DMC}^{loc}(\mathbf{R}, \mathbf{x}) \cos(\mathbf{k}\mathbf{x}), \quad (3.87)$$

where  $\Omega_k$  is the solid angle which corresponds to the vector  $\mathbf{k}$ . In the QMC algorithm the calculation of the momentum distribution can be done simultaneously with the calculation of the OBDM. More precisely, every time the value  $quoc$  is calculated it should be multiplied by  $\cos(\mathbf{k}\mathbf{x})$ . The vector  $\mathbf{k}$  is usually compatible with PBC's and is taken as  $\mathbf{k} = \frac{2\pi}{L}(n_x, n_y, n_z)$ , where  $L$  is the size of the simulation box,  $n_x, n_y, n_z$  are integer numbers.

Another important quantity is the static structure factor  $S(k)$ , which has the meaning of the correlation between density fluctuations in momentum space. It is defined as the Fourier transform of  $g(x)$

$$S(k) = 1 + n \int \mathbf{x} (g(x) - 1) e^{i\mathbf{k}\mathbf{x}}. \quad (3.88)$$

One way to calculate  $S(k)$  is to perform a Fourier transformation of  $g(x)$ . However, this method does not work properly in the case when  $S(k)$  has a

very sharp structure as, for example, for crystals. This happens because in MC simulations  $g(x)$  can be calculated only up to half the size of a simulation box and this cut-off distance in real space leads to errors in momentum space. It is useful to calculate  $S(k)$  directly in the MC algorithm. The static structure factor can be defined as the product of density fluctuation operators  $\chi_{\mathbf{k}}$  as

$$S(\mathbf{k}) = \langle \chi_{\mathbf{k}} \chi_{-\mathbf{k}} \rangle = \left\langle \sum_{i,j} e^{i\mathbf{k}(\mathbf{r}_i - \mathbf{r}_j)} \right\rangle. \quad (3.89)$$

Here  $\chi_{\mathbf{k}} = \sum_{\mathbf{q}} a_{\mathbf{q}}^{\dagger} a_{\mathbf{q}+\mathbf{k}}$ , where  $\hat{a}^{\dagger}$  and  $\hat{a}$  are the standard creation and annihilation operators in momentum space  $\mathbf{k}$ . The expression (3.89) can be rewritten in a form suitable for MC calculations as

$$S(k) = \frac{1}{N} \int d\Omega_k \int \rho_{DMC}(\mathbf{R}) S_{loc}(\mathbf{k}, \mathbf{R}) d\mathbf{R}, \quad (3.90)$$

where  $S_{loc}(\mathbf{k}, \mathbf{R}) = \sum_{i,j} e^{i\mathbf{k}(\mathbf{r}_i - \mathbf{r}_j)}$  and  $d\Omega_k$  is the solid angle which corresponds to the vector  $\mathbf{k}$ .

As an example, let us consider the correlation functions discussed above, for a two dimensional noninteracting Fermi gas. The pair-correlation function is given by

$$\begin{aligned} g(x) &= \frac{1}{n^2 V^2} \sum_{\mathbf{k}, \mathbf{k}'} \langle \hat{a}_{\mathbf{k}}^{\dagger} \hat{a}_{\mathbf{k}'}^{\dagger} a_{\mathbf{k}'} a_{\mathbf{k}} \rangle (1 - e^{i(\mathbf{k}-\mathbf{k}')\mathbf{x}}) = 1 - \left| \frac{1}{nV} \sum_{\mathbf{k}} n_{\mathbf{k}} e^{i\mathbf{k}\mathbf{x}} \right|^2 \\ &= 1 - \left| \frac{1}{n4\pi^2} \int_{-\pi}^{\pi} d\theta \int_0^{k_F} k e^{ikx \cos(\theta)} dk \right|^2 = 1 - \frac{4}{k_F^2 x^2} J_1^2(k_F x), \end{aligned} \quad (3.91)$$

where  $n_{\mathbf{k}}$  is the momentum distribution,  $k_F$  is the modulus of the Fermi wave vector and  $J_1(x)$  is the Bessel function of the first kind. The pair-correlation function is shown in Fig. 5.10(a), where the line shows the expression (3.91) and the points are calculated using the MC method. One can see that correlations rapidly decay as a function of  $x$ , but for a distance smaller than  $1/k_F$  the probability to find two fermions close to each other is greatly suppressed. This effect is called anti-bunching and it has purely quantum mechanical origin. More precisely, this effect is the direct consequence of the Pauli exclusion principle.

The static structure factor can be straightforwardly calculated using the definition (3.88) and the explicit form of  $g(x)$  from Eq. (3.91). The result is plotted in Fig. 5.10(b) and compared with direct VMC evaluation.

The one-body density matrix for a two-dimensional non-interacting Fermi gas is given by

$$\begin{aligned} \rho(x) &= \frac{1}{nV} \sum_{\mathbf{k}} \langle \hat{a}_{\mathbf{k}}^{\dagger} a_{\mathbf{k}} \rangle e^{i\mathbf{k}\mathbf{x}} = \frac{1}{nV} \sum_{\mathbf{k}} n_{\mathbf{k}} e^{i\mathbf{k}\mathbf{x}} \\ &= \frac{1}{n4\pi^2} \int_{-\pi}^{\pi} d\theta \int_0^{k_F} k e^{ikx \cos(\theta)} dk = \frac{2}{k_F x} J_1(k_F x). \end{aligned} \quad (3.92)$$

The result (3.92) is plotted in Fig. 5.7(c) with a line and the points show the results of a McMillan VMC calculation of the OBDM.

The momentum distribution for a noninteracting gas calculated using a MC simulation is shown in Fig. 3.1(d). As it is expected, it has the shape of a step function with a jump at  $k_F$ .

The above discussed correlation functions of a non-interacting Fermi gas are important for the study of interacting Fermi systems presented in Section 4.7. Also, it is worth noticing here, that for a noninteracting gas VMC calculations are exact.

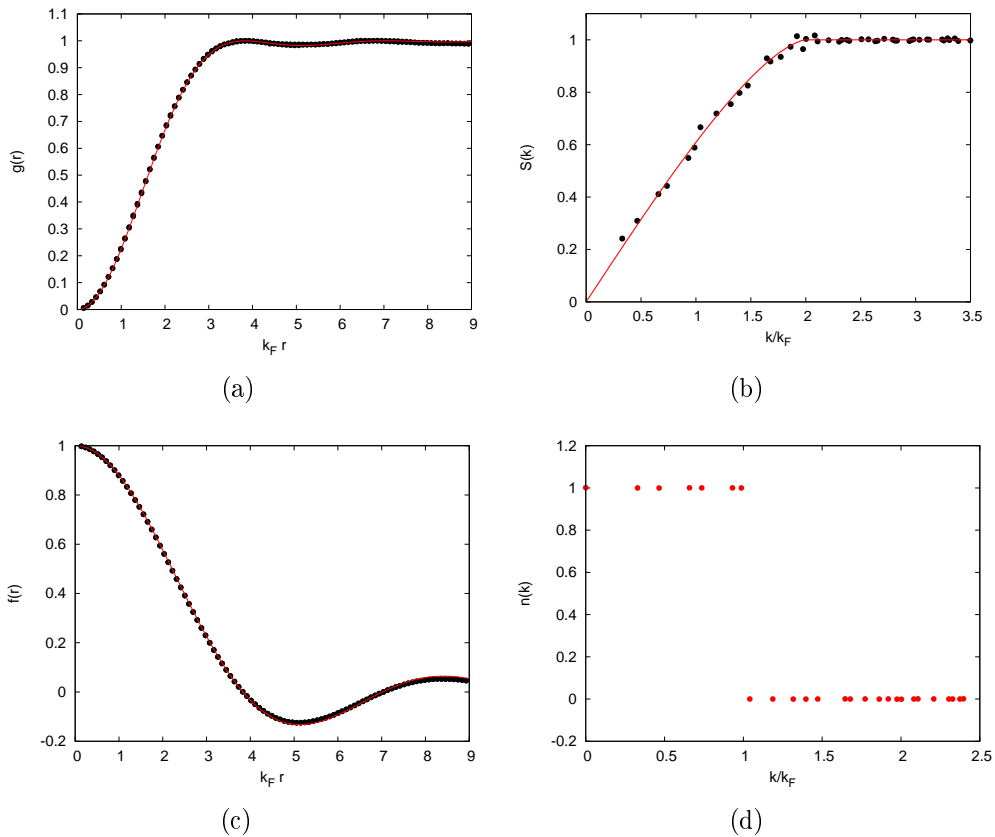


Figure 3.1: Correlation functions for a 2D noninteracting Fermi gas: pair-distribution function 5.10(a), static structure factor 5.10(b), one-body density matrix 5.7(c) and momentum distribution 3.1(d). The line is the result of analytical calculations; points are obtained from MC calculations, the error bars are smaller than symbol size.



# Liquid and Crystal Phases of Dipolar Fermions in Two Dimensions

---

In this chapter the liquid and crystal phase of a single-component Fermi gas with dipolar interactions are investigated using the FNDMC method in two spatial dimensions and at zero temperature. The dipoles are oriented by an external field perpendicular to the plane of motion, resulting in a purely repulsive  $1/r^3$  interaction. In the liquid phase we calculate the equation of state as a function of the interaction strength and other relevant properties characterizing the Fermi-liquid behavior: effective mass, discontinuity at the Fermi surface and pair correlation function. In the high density regime we calculate the equation of state of the Wigner crystal phase and the critical density of the liquid to solid quantum phase transition. Close to the freezing density we also search for the existence of a stripe phase, but such a phase is never found to be energetically favorable. This chapter shares the main results with Ref. [9].

## 4.1 Introduction

The single-layer and multi-layer configurations of two-dimensional fermions are particularly intriguing because of the competing interplay, depending on the strength of the dipolar interaction and on the distance between layers, between Fermi liquid behavior, superfluid pairing, crystal order and density-wave instabilities [106, 39, 40, 43, 107, 108, 109, 110, 36]. As it was discussed in Section 1.1, the fermionic molecules of  $^{40}\text{K}^{87}\text{Rb}$ , which can have a strong electric dipole moment, have been created using coherent transfer of weakly bound molecules to their rovibrational ground state [20] and have been brought toward the quantum degenerate regime [21]. Other fermionic molecules are now being actively studied experimentally [24, 23]. Atomic species with a large magnetic moment, such as dysprosium, offer a different possibility of realizing degenerate Fermi gases of dipoles that was

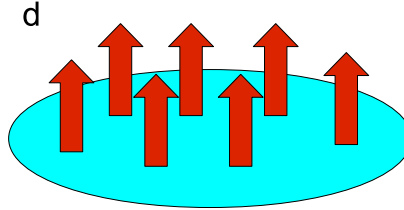


Figure 4.1: 2D system of one-component fermions with dipolar momentum oriented perpendicular to the plane

successfully pursued, although for the moment only in the weakly interacting regime, in the experiment of Ref. [18].

A particularly simple geometrical arrangement of a single-component dipolar Fermi gas in 2D is when the dipoles are oriented perpendicular to the plane of motion by means of a sufficiently strong external field. This configuration has been proven to greatly suppress the chemical reaction rate of molecules, thereby enhancing their lifetime [22]. Here particles at distance  $r$  interact via a purely repulsive, rotationally symmetric and long range  $1/r^3$  potential. Still the phase diagram at zero temperature is expected to be quite rich: interlayer dimers and a novel BCS-BEC superfluid crossover are predicted in bilayer systems [43], while in-plane and out-of-plane density ordered phases are predicted in multilayer systems [107, 108]. In the case of a single layer, a Fermi liquid with peculiar scattering properties is stable at low density [36] and a Wigner crystal emerges at high density, where the classical potential energy of dipoles largely exceeds their kinetic energy. For intermediate values of the interaction strength an instability at finite wave vector is predicted to set in [39, 40, 110], driving the system to a stripe phase that breaks both rotational and translational symmetry (in the direction perpendicular to the stripes). A similar scenario, involving microemulsion phases (*e.g.* stripes or bubbles) is expected for the melting of the Wigner crystal at  $T = 0$  in a 2D Coulomb gas [111]. These results are derived within a mean-field approach: an important question concerns the quantitative determination of the phase diagram using more accurate theoretical tools, such as quantum Monte Carlo (QMC) techniques. In this chapter we examine a 2D system of  $N$  identical fermionic particles of mass  $m$  (Fig. 4.1) that interact with the Hamiltonian

$$H = -\frac{\hbar^2}{2m} \sum_i \nabla_i^2 + \sum_{i<j} \frac{d^2}{r_{ij}^3}, \quad (4.1)$$

where  $r_{ij}$  is the distance between particle  $i$  and  $j$  and  $d$  is the intensity of the electric (or magnetic) dipole moment. The strength of the dipolar interaction is conveniently expressed in terms of the dimensionless parameter  $k_F r_0$ , where

$r_0 = md^2/\hbar^2$  is the characteristic length of the dipole-dipole force and  $k_F = \sqrt{4\pi n}$  is the Fermi wave vector of the 2D gas determined by the density  $n$ . Also, instead of  $k_F r_0$ , we use the dimensionless density  $nr_0^2$ . Energy is expressed in units of the Hartree-Fock energy

$$E_{HF} = \frac{E_F}{2} \left( 1 + \frac{128k_F r_0}{45\pi} \right), \quad (4.2)$$

where  $E_F = \frac{\hbar^2 k_F^2}{2m}$  is the Fermi energy of a 2D noninteracting Fermi gas. Sometimes it is convenient to use  $\frac{\hbar^2}{mr_0^2} (nr_0^2)^{3/2}$  as units for energy. The above result is derived [36] using first order perturbation theory.

## 4.2 Calculation of the potential energy

In this section we discuss the details of the calculation of potential energy, which requires a careful treatment. The dipolar potential  $V_d = \frac{d^2}{r^3}$  in two dimensions is strictly speaking not longranged, because the integral over all space  $\int_S V_d d^2r$  converges. But still  $V_d$  decays relatively slow with  $r$  which leads to some complications in numerical simulations. Monte-Carlo simulations are performed in a box of volume  $V = L_x L_y$ , where we always take  $L_x \leq L_y$ . The density is  $n = N/V$  and we use periodic boundary conditions (for a detailed discussion of boundary conditions see Appendix A) in both spatial directions. The potential energy contribution to the Hamiltonian, given by the second term in Eq. (4.1), is written as

$$V_{dd} = \frac{1}{2} \sum_{n_x, n_y} \left( \sum_{i=1}^N \sum_{j=1}^N \frac{d^2}{|\vec{r}_i - (\vec{r}_j + \vec{n}L)|^3} \right), \quad (4.3)$$

where  $n_x, n_y$  are the integer numbers,  $\vec{n} = (n_x, n_y)$ . Here  $i$  and  $j$  label particles in the simulation cell and the vectors  $\vec{r}_{i(j)} + \vec{n}L$  correspond to the positions of all images of particle  $i(j)$  in the array of replicas of the simulation cell. At  $n_x = n_y = 0$  the expression (4.3) gives the energy without any replicas. At  $i = j$  Eq. (4.3) gives a self-energy which has the meaning of the energy contribution due to the interaction of a particle with its own images. The inclusion of the self-energy term is necessary in order that all replicas of the simulation cell have the same density  $n$ , which provides a good approximation of the homogeneous medium.

In the case of the Coulomb potential the summation in Eq. (4.3) is carried out by means of the Ewald method [62]. In this method one can replace the sum of potential energy in real space with the sum in momentum space which converges much faster. For dipolar systems this technique was used,

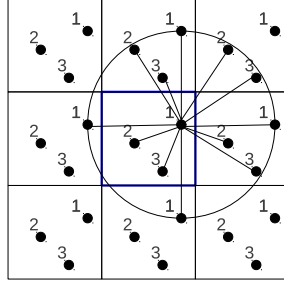


Figure 4.2: Estimation of potential energy at the example of a system containing 3 particles with  $L_{cut} = L$ .

for example, in [46]. But the use of Ewald summation requires the calculation of some special functions (such as the error function), which, in practice, makes the simulation more time consuming. Therefore we use an alternative technique, where the mean interaction energy is evaluated using the simpler formula

$$\langle V \rangle = \Sigma + E_{tail} , \quad (4.4)$$

here  $\Sigma$  denotes the sum (4.3) with the constraint  $|\mathbf{r}_i - \mathbf{r}_j - \mathbf{R}| \leq L_{cut}$  and  $E_{tail}$  is the contribution from distances larger than  $L_{cut}$  assuming an uniform distribution of particles. Fig. 4.2 illustrates the calculation of one of the terms in the sum (4.3) for  $i = 1$ ,  $N = 3$  and  $m = \frac{L_{cut}}{L} = 1$ . The blue square in the center is the simulation box, and the surrounding squares are its replicas. The cut-off distance for the calculation of potential energy is taken here equal to  $L$  (black circle). Lines show all terms in sum (4.3) over  $j$ . The tail energy can be calculated using the following formula:

$$\frac{E_{tail}(m)}{N} = \frac{1}{2} \int_{mL_x}^{\infty} \frac{d^2}{r^3} g(r) n 2\pi r dr, \quad (4.5)$$

where  $g(r)$  is the pair distribution function. An approximate value of the integral (4.5) can be obtained by replacing  $g(r)$  by its average value in the bulk  $g(r) = 1$ , so Eq. (4.5) becomes

$$\frac{E_{tail}}{\frac{\hbar^2}{mr_0^2} N} = (nr_0^2)^{3/2} \frac{\pi}{m\sqrt{N\rho}}, \quad (4.6)$$

where  $\rho = \frac{L_x}{L_y}$ .

Fig. 4.3 shows the dependence of the energies  $\Sigma$  and  $\Sigma + E_{tail}$  on cut-off distance  $m$  for a Fermi liquid at  $k_f r_0 = 40.11$ . It can be seen that if one performs only the summation (which means calculation of  $\Sigma$ ) the cut-off distance should be around  $40L$ . But it is possible to significantly reduce the

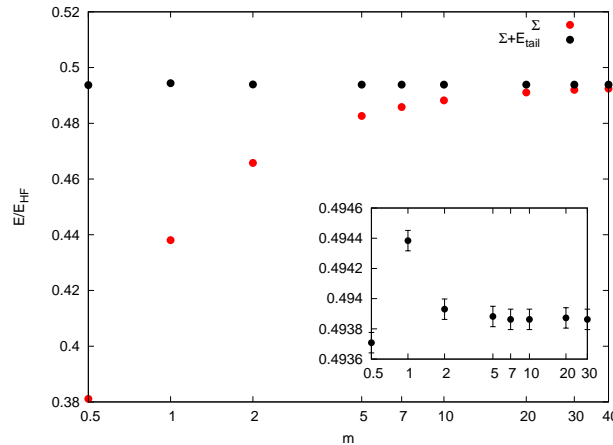


Figure 4.3: The dependence of the direct sum of potential energy  $\Sigma$  (the red points) on cutoff  $m$  ( $L_{cut} = mL$ ); the black points on the main figure and on the inset show  $\Sigma + E_{tail}$ .

cut-off by adding  $E_{tail}$ . In such case  $m = 2$  is already enough for the correct estimate of the potential energy within a typical statistical uncertainty. In this chapter the cut-off  $m = 2$  is usually used.

## 4.3 Fermi liquid phase

### 4.3.1 General physical properties of a Fermi liquid and the Slater-Jastrow wave function

According to Landau Fermi-liquid theory [99, 100, 101] the energy of a Fermi-system can be written as an energy functional of occupation numbers of quasiparticles, which behaves like an ideal Fermi gas:

$$E = E_0 + \int \delta n_{\mathbf{k}} e(\mathbf{k}) d\mathbf{k} + \int \delta n_{\mathbf{k}} \delta n_{\mathbf{k}'} d\mathbf{k} d\mathbf{k}' f(\mathbf{k}, \mathbf{k}') + \dots \quad (4.7)$$

where  $\delta n_{\mathbf{k}}$  is the deviation of the quasiparticle occupation from the ground state, and  $e(\mathbf{k})$  and  $f(\mathbf{k}, \mathbf{k}')$  are quasiparticle energy functionals. The perturbative calculations of the ground-state properties of two-dimensional dipolar Fermi gases were performed in [36], but they are limited by the regime of weak interaction strength.

Our first goal is to obtain the ground-state energy for an arbitrary strength of interaction by means of FNDMC. The trial wave function describing the FL phase is assumed of the Jastrow-Slater form

$$\psi_T(\mathbf{r}_1, \dots, \mathbf{r}_N) = \prod_{i < j} f(r_{ij}) \det[e^{i\mathbf{k}_\alpha \cdot \mathbf{r}_i}]. \quad (4.8)$$

Here  $\mathbf{k}_\alpha = (2\pi/L)(n_\alpha^x, n_\alpha^y)$  with  $n_\alpha^{x,y} = 0, \pm 1, \pm 2, \dots$  are the wave vectors complying with periodic boundary conditions in the square box ( $L_x = L_y = L$ ) and  $f(r)$  is a non-negative function satisfying the boundary condition  $f'(r = L/2) = 0$ . The short-range ( $r \leq R_p$ , where  $R_p$  is a variational parameter) behavior of  $f(r)$  is of the form  $f(r) \propto K_0(2\sqrt{r_0/r})$ , where  $K_0$  is the modified Bessel function. It also fulfills the cusp condition of the atomic potential. At large distance ( $r > R_p$ ) collective behavior (phonons) is expected, so the long-range part of the wave function decays as  $f(r) \propto \exp(-const/r)$  [45].

### 4.3.2 Optimization of the variational parameter $R_p$

Before performing DMC calculations it is important to optimize the wave function using the VMC technique, because the better the wave function the smaller the variance of the energy. But, how it was already discussed in Section 3.6, the value of the FNDMC energy is affected only by the nodal surface. In the present case only the Jastrow term contains a variational parameter which does not change the nodal surface and therefore the VMC energy minimization can lead just to the decrease of the variance. The example of such optimization is shown below at large and small densities for different numbers of particles.

Fig. 4.4 presents the direct  $E_1$  and the force  $E_2$  VMC energy estimates for 25 particles at  $nr_0^2 = 0.01989$ . One can see that the VMC energy as a function of  $R_p$  has a clear minimum at  $R_p^{min} \approx 0.03$ . It is worth noticing that  $E_1$  and  $E_2$  agree within error bars which is a good check that the wave function and the quantum force are implemented correctly in the VMC algorithm.

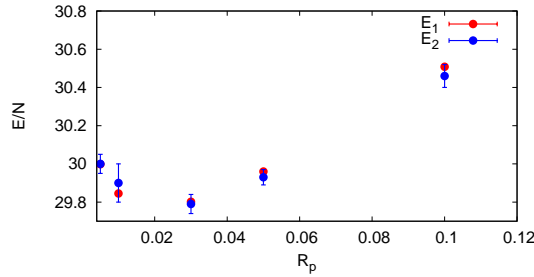


Figure 4.4: The direct  $E_1$  and the force  $E_2$  VMC estimates of the energy for 25 particles at density here is  $nr_0^2 = 0.01989$ . The energy is in units of  $\frac{\hbar^2}{mr_0^2}(nr_0^2)^{3/2}$ .

Fig. 4.5 shows similar VMC studies but at the larger density  $nr_0^2 = 32$  for 25, 49 and 61 particles. VMC energy has the minimum at  $R_p^{min} \approx 0.15$  for 25 particles and at  $R_p^{min} \approx 0.1$  for 49 and 61 particles. So, we can conclude that  $R_p^{min}$  becomes larger for larger densities but is not very sensitive to the

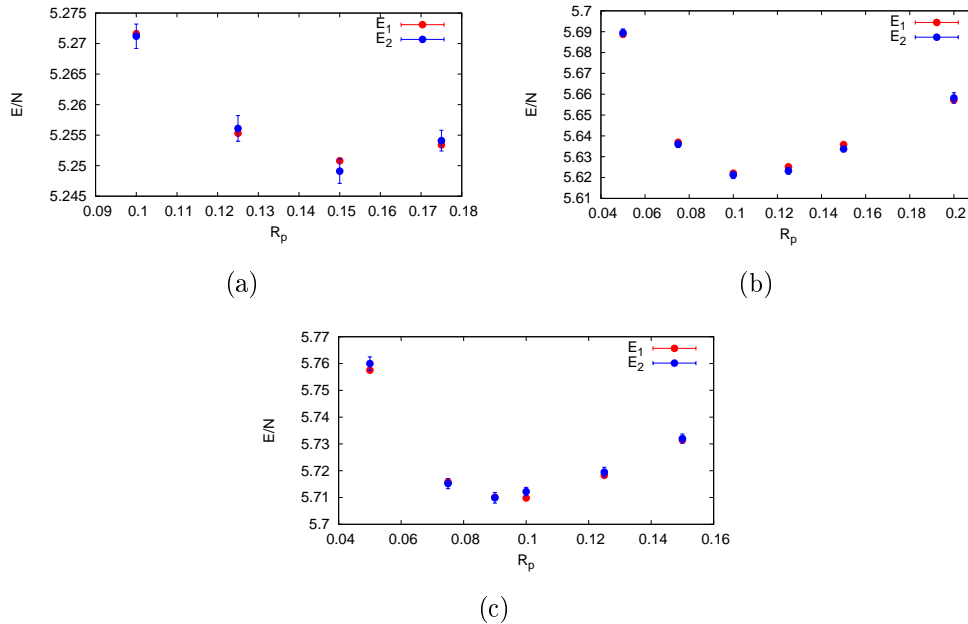


Figure 4.5: The direct  $E_1$  and the force  $E_2$  VMC estimates of the energy for 25 particles (a), for 49 particles (b) and 61 particles (c). The density here is  $nr_0^2 = 32$ , the energy is in  $\frac{\hbar^2}{mr_0^2}(nr_0^2)^{3/2}$  units.

number of particles.

### 4.3.3 Optimization of DMC parameters: time step and number of walkers

As it was mentioned in Chapter 3, the energy calculated by the DMC method is biased by the averaged number of walkers  $N_w$ , the time step  $dt$  and the system size. All these issues require a careful treatment. In this section we discuss the optimization of the average number of walkers and of the time step. Fig. 4.6 presents the energy dependence on the average number of walkers. This dependence can be fitted by a linear function in order to find the extrapolated value of the energy for an infinite number of walkers. One can see that the DMC energy for 200 walkers already agrees with the extrapolated value within statistical uncertainty.

The following Fig. 4.7 contains the energy dependence on time step. In the DMC algorithm we use a Green's function which is accurate up to  $O(t^2)$  ( see Eqs. (3.59), (3.60)), therefore the linear dependence on time step is expected [94]. But the use of the Metropolis acceptance Eq. (3.66) can lead to a non-linear dependence at large time step. However, at small  $dt$  the dependence can be fitted by a linear function. It is seen from the Fig. 4.7 that the DMC

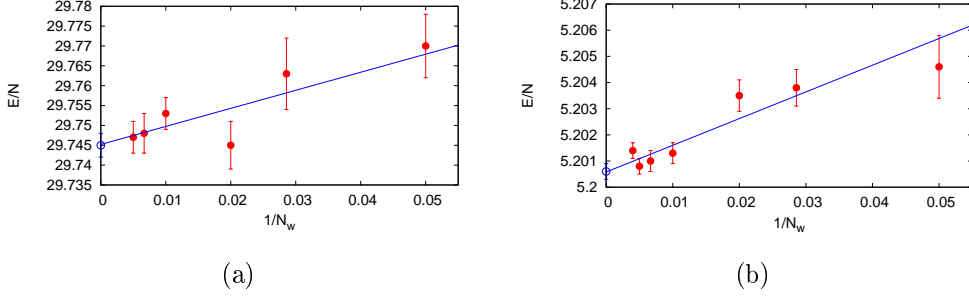


Figure 4.6: Dependence of DMC energy on number of walkers  $N_w$  for 25 particles: at  $nr_0^2 = 0.01989$  (a) and at  $nr_0^2 = 32$  (b). The energy is in units of  $\frac{\hbar^2}{mr_0^2}(nr_0^2)^{3/2}$ . The filled red circles are DMC energies, the blue line is linear fit and the blue empty circle is the extrapolated value of energy to the infinite number of walkers.

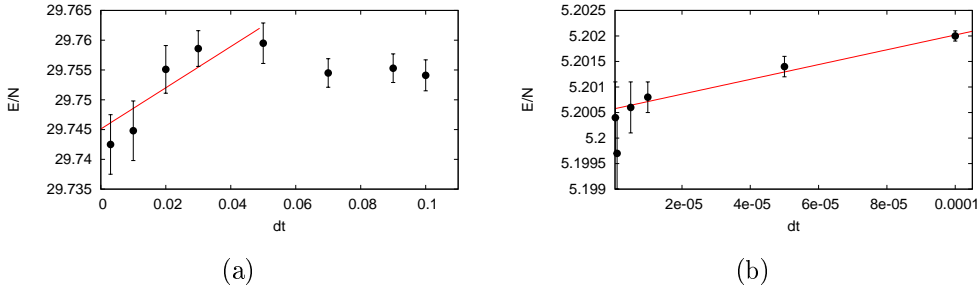


Figure 4.7: Dependence of DMC energy (the black points) on time step  $dt$  for 25 particles: at  $nr_0^2 = 0.01989$  (a) and at  $nr_0^2 = 32$  (b). The red lines show the linear fit. The energy is in units of  $\frac{\hbar^2}{mr_0^2}(nr_0^2)^{3/2}$ .

energy at  $dt = 0.01$  (for  $nr_0^2 = 0.01989$ ) and  $dt = 5 \cdot 10^{-6}$  (for  $nr_0^2 = 32$ ) agrees with the extrapolated value within the statistical uncertainty. The acceptance rate of the Metropolis check depends on  $dt$ , and here it equals approximately 99.95% in both cases. In order to choose an appropriate time step at a given density the following criterium is used: the acceptance rate should be around 99.95% – 99.98%, but not smaller (otherwise one needs much longer runs to get statistically satisfactory results). Finally, it is worth to comment here, that the use of the Metropolis check was found to be necessary, even for very high acceptance rate  $\leq 99.95\%$ . Without it an instability was observed in the DMC algorithm, because occasionally the number of walkers has increased too much due to the large fluctuations in the local energy.

### 4.3.4 Extrapolation to the thermodynamic limit

In this section we discuss the extrapolation to the thermodynamic limit (TL) which appears to be the most delicate issue related to QMC calculations of the equation of state. In the FL phase apart from the size dependence affecting the potential energy contribution, which we treated using the procedure discussed in Section 4.2, significant shell effects are present in the kinetic energy contribution. We consider closed-shell configurations corresponding to  $25 \leq N \leq 81$  for which the relative error  $|\Delta T_N|/E_{TL}^{(0)} = |E_N^{(0)}/E_{TL}^{(0)} - 1|$  in the energy of the non-interacting gas compared to the TL can be as large as  $\sim 1\%$ . As it was already discussed in Section 4.3.1, in the Fermi liquid phase the energy of the system can be written as an energy functional (4.7) of quasi-particle occupation numbers, which behave just like an ideal Fermi gas. Size corrections of the kinetic energy for interacting systems are expected to be proportional to the size corrections of the corresponding noninteracting system. An extrapolation method based on FL theory is provided by the fitting formula [60]

$$E_N = E_{TL} + \frac{m}{m_*} \Delta T_N + \frac{a}{N}, \quad (4.9)$$

which involves the parameter  $m/m_*$ , determining the inverse effective mass of the particles, and the coefficient  $a$  of the residual size dependence assumed to be linear in  $1/N$  analogously to the case of Coulomb systems [112]. Here  $E_N$  is the QMC output energy of the  $N$ -particle system with the potential contribution evaluated using Eq. (4.4). The values of  $E_N - \Delta T_N$  are shown as red symbols in Fig. 4.8. Their scattered dependence on  $1/N$  is considerably suppressed if one accounts for the effective mass, as it is shown by the green symbols corresponding to  $E_N - (m/m_*)\Delta T_N$ . A more reliable convergence to the TL is obtained using the method of twist-averaged boundary conditions (TABC) [113] (for a detailed discussion of TABC see Appendix A). Here the PBC wave vectors of the plane waves in the Slater determinant of Eq. (4.8) are replaced by  $\mathbf{k}_\alpha(\theta) = (2\pi/L)(n_\alpha^x + \theta_x, n_\alpha^y + \theta_y)$ , where  $\theta_x, \theta_y$  are continuous variables in the interval  $[0, 1]$ . In the grand canonical implementation of TABC described in Refs. [113, 114] the wave vectors are constrained by  $|\mathbf{k}_\alpha(\theta)| < k_F$  and different values of the twist  $\boldsymbol{\theta}$  can correspond to different numbers of particles. The number of particles  $\bar{N}$  and the energy  $E_{\bar{N}}$  are obtained from averages over all possible twist angles. With our use of TABC (where for each twist we keep fixed not the volume of the simulation box, but the density) we still find a residual size effect  $\Delta T_{\bar{N}}$  which is much smaller than in the PBC case. The extrapolation to the TL is performed using Eq. (4.9) both for PBC and TABC, where the coefficient in front of  $\Delta T_{\bar{N}}$  gives a reliable estimate of the effective mass only in the case of PBC (see Appendix A for more details).

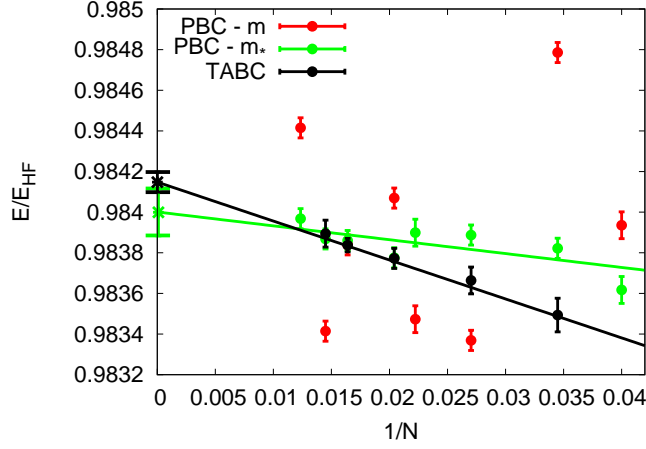


Figure 4.8: Finite size effects in a Fermi liquid at the density  $k_F r_0 = 0.22$ . Black symbols and line correspond to TABC energies and linear fit. Green symbols and line correspond to PBC energies  $E_N - (m/m_*)\Delta T_N$  and linear fit. Red symbols correspond instead to PBC energies  $E_N - \Delta T_N$ . The values extrapolated to the TL are shown with the corresponding error bars.

We obtain statistical agreement in  $E_{TL}$  between PBC and TABC for all values of the density (see Fig. 4.8).

### 4.3.5 Equation of state, effective mass and renormalization factor

In this section we discuss the FNDMC results in thermodynamic limit at small interaction strength, which were obtained using the techniques discussed in the previous sections of this chapter.

The results are shown in Fig. 4.9 using black points. Blue and red lines are the ground state energy  $E_{pe}$  perturbatively calculated up to the first (which gives the Hartree-Fock energy  $E_{HF}$ ) and the second order in  $k_F r_0$ , correspondingly. More precisely  $E_{pe}$  has the following form [36]:

$$\frac{E_{pe}}{N} = \frac{\hbar^2 k_F^2}{4m} \left( 1 + \frac{128}{45\pi} k_F r_0 + \frac{1}{4} (k_F r_0)^2 \ln(uk_F r_0) \right), \quad (4.10)$$

here  $N$  is the number of particles,  $u = 1.43$  is a constant. It can be seen from the inset of Fig. 4.9 that the Hartree-Fock term is quantitatively accurate only up to  $k_F r_0 \approx 0.1$ . Taking into account the second order term makes  $E_{pe}$  accurate up to  $k_F r_0 \approx 0.3$ . For larger interaction strengths,  $k_F r_0 > 0.5$ ,

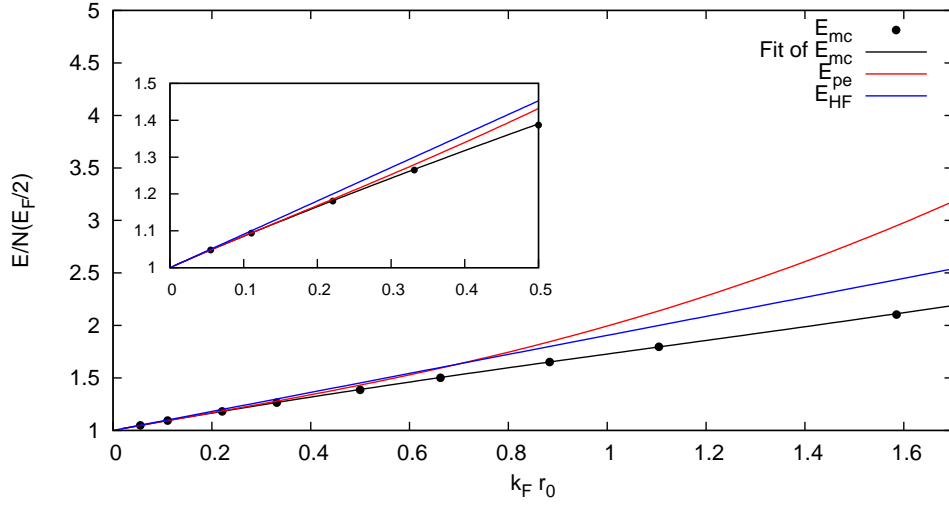


Figure 4.9: Dependence of FL energy in thermodynamical limit on strength of dipolar interaction  $k_F r_0$ .

deviations are visible between QMC results and the perturbation expansion  $E_{pe}$ .

From the fit of  $E_{MC}$  (black line in Fig. 4.9) we have obtained higher order corrections to  $E_{pe}$ :

$$\frac{E_{MC}}{N} = \frac{E_{pe}}{N} + \frac{E_F}{2} \left( a * (k_F r_0)^3 + b * (k_F r_0)^4 + c * (k_F r_0)^5 \right), \quad (4.11)$$

where  $a = -0.413(14)$ ,  $b = 0.177(16)$ ,  $c = -0.031(4)$ . The results for the EOS for large values of  $k_F r_0$  are presented in Section 4.6.

Now let's discuss the results for the effective mass that were obtained from the fit (4.9) of the QMC energies calculated using PBC. The results of the weakly interacting regime are presented at Fig. 4.10. The effective mass decreases with the increase of the dipolar interaction. A similar behavior is predicted from perturbative calculations [36]:

$$\left( \frac{m_*}{m} \right)_{pe} = \left( 1 + \frac{4}{3\pi} k_F r_0 + 0.25 (k_F r_0)^2 \ln(0.65 k_F r_0) \right)^{-1}. \quad (4.12)$$

One can see that, similarly to the case of the ground-state energy, the first order correction is quantitatively valid only for  $k_F r_0 < 0.1$ , while the second-order correction is accurate for  $k_F r_0 < 0.5$ . We can conclude that at weak coupling our results reproduce the perturbation expansion well. The effective mass in the strong-coupling regime is shown in Fig. 4.11. One can see that the reduction of  $m_*$  is less pronounced than the perturbative prediction and

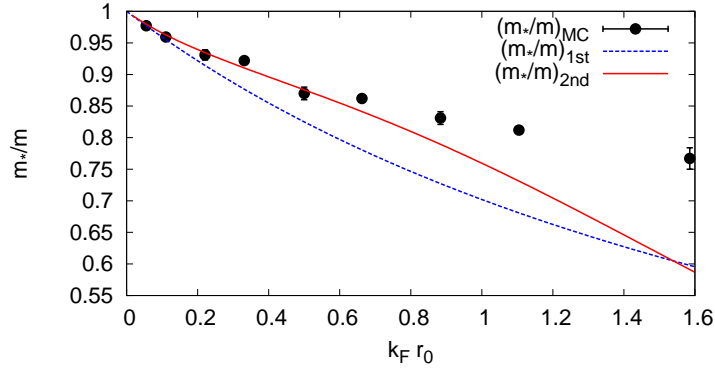


Figure 4.10: Dependence of the effective mass  $m/m^*$  on strength of dipolar interaction  $k_F r_0$  at the weakly interacting regime. Black points are QMC results, dashed blue line is the perturbative expansion up to the first order, red line is the perturbative expansion up to the second order.

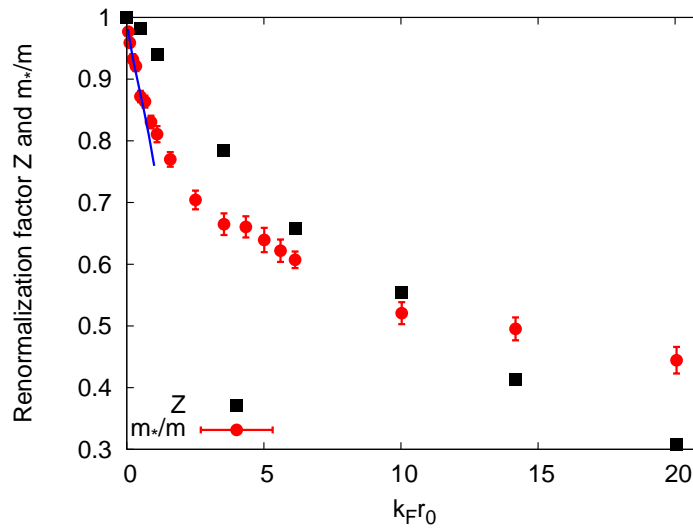


Figure 4.11: Effective mass and renormalization factor in the liquid phase as a function of the interaction strength. The line corresponds to the perturbation expansion for  $m^*/m$  of Ref. [36].

$m_*/m$  approaches the value 0.4 for  $k_F r_0$  close to freezing. In Fig. 4.11 we also present the results for the renormalization factor  $Z$ , which is extracted from the discontinuity at  $k_F$  of the momentum distribution parametrized by  $n_k = Z\theta(k_F - k) + g(k)$ , where  $\theta(x)$  is the step function and  $g(k)$  is a continuous function of  $k$ .

Finally it is worth discussing here the validity of the procedure to extract  $m_*$  simply as the coefficient in Eq. (4.9). In the case of a Coulomb gas the fitting procedure Eq. (4.9) works well for the FL phase but the coefficient in front of  $\Delta T_N$  does not give a good estimate of  $m_*/m$ . This fact can be understood from the arguments below. In order to define  $m_*/m$  from Eq. (4.9) all other parameters of the FL phase should not change when the system size changes. But for a Coulomb gas at least one parameter, namely the renormalization factor, has a strong dependence on the number of particles [115]. Therefore the calculation of the effective mass of a Coulomb gas requires the use of more sophisticated techniques. In the case of a 2D dipolar Fermi gas the situation is different, because  $Z$  does not show any significant dependence on the system size (for details see Section 4.7). So, we believe that the coefficient in front of  $\Delta T_N$  in Eq. (4.9) indeed gives a reliable estimate of the effective mass.

### 4.3.6 Chemical potential and compressibility

The equation of state allows one to easily calculate important quantities related to the system such as chemical potential  $\mu = \frac{\partial E}{\partial N}$ , where  $N$  is the number of particles and inverse compressibility  $\kappa^{-1} = n^2 \frac{\partial \mu}{\partial n}$ . These quantities were also calculated perturbatively [36]:

$$\begin{aligned} \frac{\mu_{pe}}{E_F} &= 1 + \frac{32}{9\pi} k_F r_0 + \frac{3}{8} (k_F r_0)^2 \ln(1.68 k_F r_0), \\ \frac{\kappa_{pe}^{-1}}{E_F(N/S)} &= 1 + \frac{16}{3\pi} k_F r_0 + \frac{3}{4} (k_F r_0)^2 \ln(2.16 k_F r_0). \end{aligned} \quad (4.13)$$

The comparison of  $\mu$  and  $\kappa$  with the predictions of Eqs. (4.11) and (4.13) is presented in Fig. 4.12. The fit of  $\mu$  and  $\kappa$  is shown below:

$$\begin{aligned} \frac{\mu_{MC}}{E_F} &= \frac{\mu_{pe}}{E_F} - 0.723 * (k_F r_0)^3 + 0.354 * (k_F r_0)^4 - 0.0698 * (k_F r_0)^5, \\ \frac{\kappa_{MC}^{-1}}{E_F(N/S)} &= \frac{\kappa_{pe}^{-1}}{E_F(N/S)} - 1.807 * (k_F r_0)^3 + 1.062 * (k_F r_0)^4 - 0.244 * (k_F r_0)^5. \end{aligned}$$

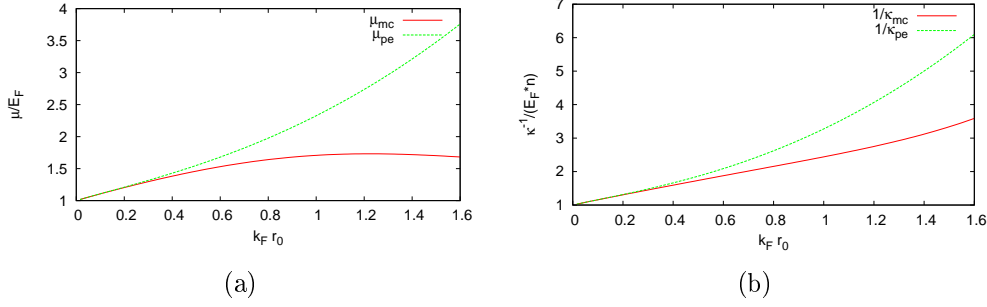


Figure 4.12: Dependence of the chemical potential (a) and compressibility (b) on strength of dipolar interaction  $k_F r_0$ . Red line presents the results obtained using (4.11) and dashed green line shows perturbative expansion (4.13).

## 4.4 Crystal phase

### 4.4.1 Wave function

As it was discussed in the last chapter two-dimensional dipolar system can be well described in terms of FL theory at relatively small  $k_F r_0$ . But this description should be broken at some value of  $k_F r_0$  when the system becomes a crystal. For two dimensional dipolar Bose gas this question was addressed in [45]. It was found that at zero temperature the triangular crystal becomes energetically preferable at density  $nr_0^2 = 290(30)$ , which corresponds to  $k_F r_0 = 60(3)$ . A FNDMC study of the triangular crystal phase for fermionic systems is performed in order to find a quantitatively reliable estimate of the freezing density. Below sometimes the term "Wigner crystal" (WC) is used in analogy with the Coulomb gas case.

To describe the WC phase we make use of the following trial wave function

$$\psi_T(\mathbf{r}_1, \dots, \mathbf{r}_N) = \prod_{i < j} f(r_{ij}) \det[e^{-\alpha(\mathbf{r}_i - \mathbf{R}_m)^2}], \quad (4.14)$$

where the Jastrow correlation term  $f(r)$  is the same as in the FL phase and the single-particle orbitals in the determinant are constructed with Gaussians, whose width  $\alpha$  is a variational parameter, centered at the lattice points  $\mathbf{R}_m$  of the triangular Bravais lattice. Fig. 4.13 shows the details of the construction of the triangular lattice. It is convenient to consider a pseudo-elementary cell (Fig. 4.13.a) which contains two atoms. It has dimensions  $a_x$  and  $a_y$  such that  $a_y = 3\sqrt{a_x}$ . In order to enforce PBC, both the number of particles  $N$  and the box sizes  $L_x$  and  $L_y$  must be multiples of this primitive cell. Moreover, we choose the combinations of primitive cells such that the simulation box is as close as possible to the square one, because the spherical constraint for dipolar

potential is used. These conditions leads these "magic" numbers of particles: 30, 56 and 90 that are always used in the following. Fig. 4.13.b shows an example of the triangular lattice used for the simulation of 30 particles at the density  $nr_0^2 = 256$ . The aspect ratio between the sizes of the simulation box for 30 particles is  $\frac{L_x}{L_y} = 0.96225$ .

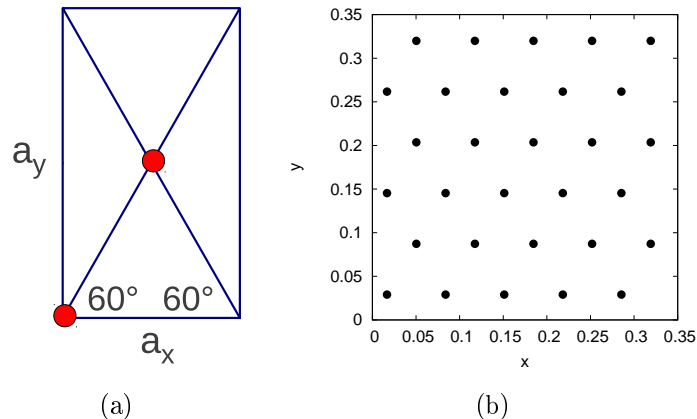


Figure 4.13: (a) The pseudo-elementary cell of triangular lattice which contains two atoms. (b) The example of triangular lattice for 30 particles, black circles are positions of lattice points  $\mathbf{R}_m$ .

#### 4.4.2 Optimization of the variational parameter $\alpha$

Before performing FNDMC calculations it is necessary to find an optimal value for the variational parameter  $\alpha$  in Eq. (4.14). Fig. 4.14 contains an example of such optimization. VMC energies are fitted by a quadratic function which gives a minimum at  $\alpha = 295$ . The variational parameter of the Jastrow part is kept fixed ( $R_p = 0.15$ ) for all values of  $\alpha$ . Such optimization of  $\alpha$  was performed for all densities considered in the WC phase.

#### 4.4.3 Finite size scaling

In the case of the WC phase the issue of finite size scaling should also be addressed carefully. We use a linear fit in  $1/N$ :

$$E_N = E_{TL} + \frac{a}{N}, \quad (4.15)$$

where  $E_{TL}$  is the energy in the thermodynamic limit and  $a$  is a fitting constant. It is worth to notice that in contrast to the case of FL (Eq. (4.11)) there is no finite size correction for the kinetic energy in Eq. (4.15). Fig. 4.15 shows

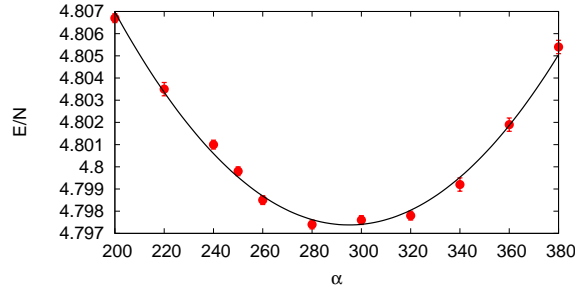


Figure 4.14: Dependence of VMC energy on the value of variational parameter  $\alpha$  for  $N = 30$  at  $nr_0^2 = 96$ . Red points are VMC energies, black line is a quadratic fit. The energy is in  $\frac{\hbar^2}{mr_0^2}(nr_0^2)^{3/2}$  units.

an example of finite size scaling at the density  $nr_0^2 = 128$ . For every value of the density we perform this extrapolation procedure in order to get  $E_{TL}$ .

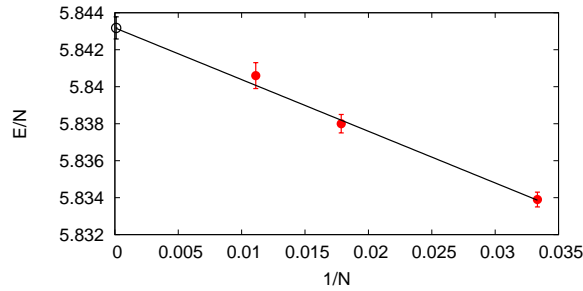


Figure 4.15: Finite size scaling of WC crystal energy. Filled red points are FN DMC energies for 30, 56 and 90 particles, black line is the linear fit and empty black point is the the energy in thermodynamical limit. The energy is in units of  $\frac{\hbar^2}{mr_0^2}(nr_0^2)^{3/2}$ .

## 4.5 Stripe phase

### 4.5.1 The model

A stripe (or density-wave) phase was predicted by several authors [106, 39, 40, 43, 107, 108, 109, 110, 36] as an intermediate phase between FL and WC which breaks both rotational and translational symmetry. But most of those studies were made at the level of mean-field theories. Here we use the FNDMC method in order to check these predictions. We consider stripes as a "melted crystal", which means that the localization around some equally

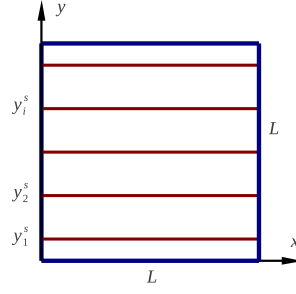


Figure 4.16: Stripes along  $y$  direction,  $L$  is the size of simulation box,  $y_i^s$  is the position of the  $i$ -th stripe.

spaced points in the  $y$  direction is preserved but in the  $x$  direction the system behaves like a FL. This assumption leads to use the Gaussian localization terms (as for the WC) in the  $y$  direction and to use plane waves (as for FL) in the  $x$  direction (Fig. 4.16). For this pattern of equally spaced stripes in the  $y$ -direction the corresponding trial wave function has the following general form:

$$\psi_T(\mathbf{r}_1, \dots, \mathbf{r}_N) = \prod_{i < j} f(r_{ij}) \det[e^{ik_{\alpha x}x_i - \gamma(y_i - y_m)^2}], \quad (4.16)$$

where the Jastrow factor is the same as in the FL and WC phase,  $y_m$  denotes the  $y$  coordinate of the  $m$ -th stripe,  $k_{\alpha x} = 2\pi n_{\alpha x}/L_x$  are the PBC wave vectors in the  $x$ -direction and  $\gamma$  is a variational parameter. It is convenient to use  $\cos k_{\alpha x}x_i$  and  $\sin k_{\alpha x}x_i$  instead of  $e^{ik_{\alpha x}x_i}$  for the single-particle orbitals, so the Slater determinant in Eq. (4.16) becomes:

$$\Delta_S = \begin{bmatrix} e^{-\gamma(y_1 - y_1^S)^2} \cos k_{n_{max}}x_1 & \cdots & \cdots & e^{-\gamma(y_N - y_1^S)^2} \cos k_{n_{max}}x_N \\ \vdots & \ddots & & \vdots \\ e^{-\gamma(y_1 - y_1^S)^2} \cos k_1x_1 & \cdots & \cdots & e^{-\gamma(y_N - y_1^S)^2} \cos k_1x_N \\ e^{-\gamma(y_1 - y_1^S)^2} & \cdots & \cdots & e^{-\gamma(y_N - y_1^S)^2} \\ e^{-\gamma(y_1 - y_1^S)^2} \sin k_1x_1 & \cdots & \cdots & e^{-\gamma(y_N - y_1^S)^2} \sin k_1x_N \\ \vdots & \ddots & & \vdots \\ e^{-\gamma(y_1 - y_1^S)^2} \sin k_{n_{max}}x_1 & \cdots & \cdots & e^{-\gamma(y_N - y_1^S)^2} \sin k_{n_{max}}x_N \\ \vdots & \ddots & & \vdots \\ \vdots & & \ddots & \vdots \\ e^{-\gamma(y_1 - y_{N_s}^S)^2} \cos k_{n_{max}}x_1 & \cdots & \cdots & e^{-\gamma(y_N - y_{N_s}^S)^2} \cos k_{n_{max}}x_N \\ \vdots & & \ddots & \vdots \\ e^{-\gamma(y_1 - y_{N_s}^S)^2} \sin k_{n_{max}}x_1 & \cdots & \cdots & e^{-\gamma(y_N - y_{N_s}^S)^2} \sin k_{n_{max}}x_N \end{bmatrix}$$

Here  $N_s$  is the number of stripes, which is also equal to the number of particles per stripe;  $n_{max} = \frac{(N_s-1)}{2}$ ,  $N$  is the total number of particles ( $N = N_s \times N_s$ ).

### 4.5.2 VMC results

Here we discuss the optimization of the trial wave function in Eq. (4.16). Firstly the width  $\gamma$  of the Gaussian localization term was optimized. It was found that usually  $\gamma$  has roughly the same value as the parameter  $\alpha$  for the crystal wave function (4.14). Then we optimize the stripe separation  $a = |y_{m+1} - y_m|$ . Here the overall density in the simulation box with area  $S = L_x \times L_y$  is fixed. So in order to change the distance  $a$  between stripes we change the ratio  $\rho = L_x/L_y$ . Fig. 4.17 contains the energy as function of the stripe separation  $a$  for 25 particles, which corresponds to 5 stripes each containing five particles;  $a_{sq}$  is the stripe separation for a square simulation box. It is important to notice here that the tail energy changes with the change of  $L_{cut}$ , so one should compare not bare VMC energies but instead  $E_{VMC} + E_{tail}$  as it is done in Fig. 4.17. It is clearly seen that an optimal value of  $a$  is  $a_{sq}$  which corresponds to  $k_F a_{sq} = \sqrt{4\pi}$ .

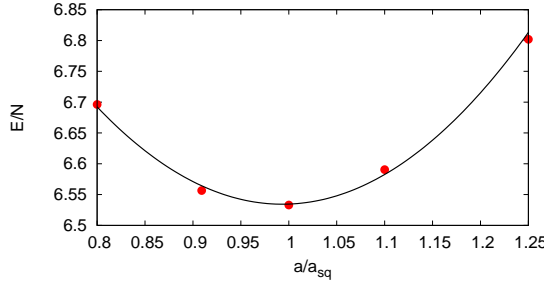


Figure 4.17: Dependence of VMC energy (with added  $E_{tail}$ ) on stripes separation  $a$  at  $k_F r_0 = 20.053$ . Energy is in  $\frac{\hbar^2}{mr_0^2} (nr_0^2)^{3/2}$  units. Error bars are smaller than symbol size.

### 4.5.3 Finite size scaling

In order to find the energy in the thermodynamic limit we perform simulations for 25 ( $5 \times 5$ ), 49 ( $7 \times 7$ ) and 81 ( $9 \times 9$ ) particles at every density. Such numbers are chosen because one needs odd numbers of particles per stripe in order to have filled one-dimensional Fermi liquid shells. Fig. 4.18 contains the example of finite size scaling for stripes at  $k_F r_0 = 20.053$ . FNDMC energies are fitted using a linear fit which allows one to perform extrapolation to the thermodynamic limit.

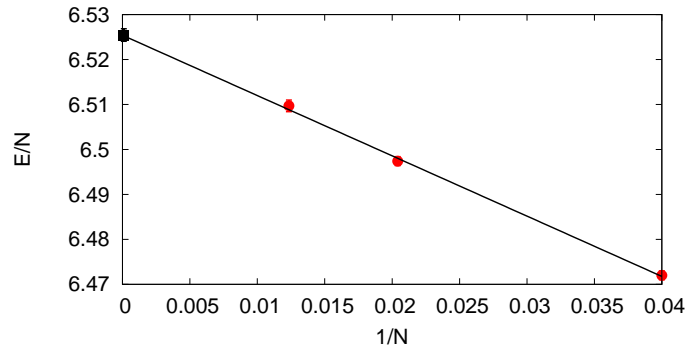


Figure 4.18: Finite scaling for stripes. Red points are FNDMC energies (with added  $E_{tail}$ ), line is a linear fit and black square is the extrapolated energy in thermodynamical limit. Energy is in  $\frac{\hbar^2}{mr_0^2}(nr_0^2)^{3/2}$  units. Error bars are smaller than symbol size.

## 4.6 Quantum phase transition liquid-crystal

In this section we discuss the main results for the equation of state (4.19). Exact data are presented in Table 4.1. FNDMC energies for FL and WC can

Table 4.1: Data for the equation of state. Here  $E_{FL}$ ,  $E_{WC}$  and  $E_{ST}$  are energies of Fermi liquid, Wigner crystal and stripes in units of  $E_{HF}$ ;  $\sigma_{FL}$ ,  $\sigma_{WC}$ ,  $\sigma_{ST}$  are corresponding standard errors.

$k_F r_0$	$E_{FL}$	$\sigma_{FL}$	$E_{WC}$	$\sigma_{WC}$	$E_{ST}$	$\sigma_{ST}$
14.17963	0.6365	0.0002	0.6387	0.0003	0.64265	0.00004
20.05303	0.60941	0.00009	0.6104	0.0002	0.6134	0.0001
28.35926	0.5857	0.0001	0.58515	0.00006	0.587689	0.000003
34.73286	0.5732	0.0001	0.57231	0.00009		
40.10605	0.56499	0.00006	0.56396	0.00006		
50.13257	0.55299	0.00009	0.5517	0.0001		
61.39960	0.54318	0.00006	0.5415	0.0001		
70.89815	0.536731	0.000004	0.53445	0.00007		

be fitted by the following function:

$$E/E_{HF} = (a * k_F r_0 + b * \sqrt{k_F r_0} + \frac{c}{k_F r_0}) / (1 + \frac{128}{45\pi} * k_F r_0). \quad (4.17)$$

The best parameters of the fit are  $a = 0.3985(2)$ ,  $b = 0.796(2)$  and  $c = 2.3(1)$  for the Fermi liquid phase and  $a = 0.3940(6)$ ,  $b = 0.817(4)$  and  $c = 2.5(2)$  for the Wigner crystal.

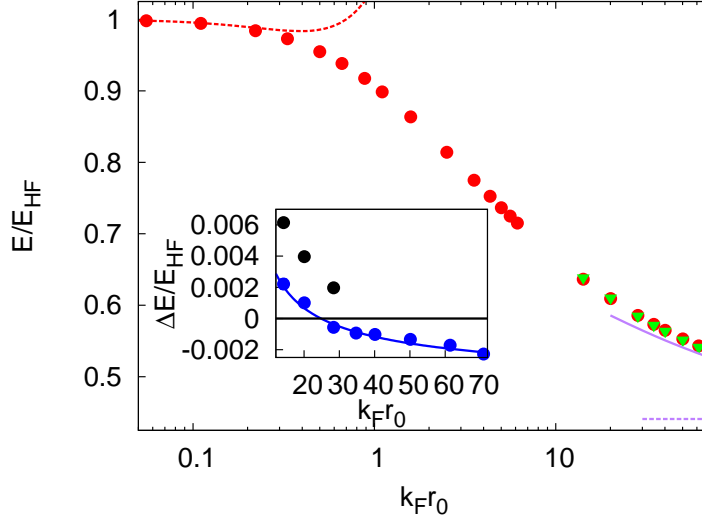


Figure 4.19: Equation of state of the liquid and solid phase in units of the Hartree-Fock energy (4.2). Circles refer to the liquid and triangles to the solid. The red dashed line corresponds to the second-order expansion in Ref. [36]. The purple dashed horizontal and solid line correspond respectively to the classical energy of the Wigner crystal and to the result of Ref. [46] including the first correction arising from the zero-point motion of phonons. Inset: Energy difference between the solid and the liquid (blue circles) and between the stripe phase and the liquid (black circles). The blue solid line is obtained from a best fit to the equation of state of the liquid and solid phase. Error bars are smaller than the symbols size and are comparable in the three phases.

The Fermi liquid equation of state was already discussed in details so here we concentrate on the results for the crystal and the stripe phase. The results for the WC equation of state are reported in Fig. 4.19 by green triangles. It is worth noticing that the antisymmetric constraint imposed in the wave function (4.14) for particle exchange has negligible effect on the energy. In fact, statistically compatible results are obtained with a nodeless wave function of distinguishable boltzmannons in agreement with the findings of Ref. [45]. This behavior is expected at large density, where the energy of the WC phase is given by the result [46]

$$E_{WC} = N \frac{\varepsilon_F}{2} \frac{k_F r_0}{4} \left( 1.597 + \frac{2.871}{\sqrt{k_F r_0}} \right), \quad (4.18)$$

obtained by including the contribution from the zero-point motion of phonons to the purely classical interaction energy of a system of dipoles arranged in a triangular Bravais lattice. The above expansion, holding for large  $k_F r_0$ , is shown in Fig. 4.19 and is indeed approached by our QMC results. The

difference between the ground-state energy of the WC and the FL phases is shown in the inset of Fig. 4.19. From the fit to the equation of state of the two phases (Eq. 4.17) we can determine the intersection point at  $k_F r_0 = 25 \pm 3$ . This value is more than a factor two smaller compared to the critical density  $k_F r_0 \sim 60$  [45, 47, 46] of an equivalent system of bosons having the same mass, density and dipolar strength. This can be understood if one considers that the equation of state of the crystal is practically independent of statistics, while the energy of the fermionic fluid is significantly larger than the bosonic one.

From the equation of state of the FL and WC phase in the vicinity of the freezing density one can also estimate the width of the region where phase separation occurs driving the first-order liquid to solid transition. This can be performed using the Maxwell double tangent construction as it is done for example for  $^4\text{He}$  [57]. This method means that one imposes the equilibrium of pressure and chemical potential in the two phases, which gives a coexistence region of width  $\delta(k_F r_0) \sim 0.01$ , a very small value consistent with a similar finding in the bosonic case [46].

Near the phase transition point the search for stripes was performed. The FNDMC results are shown in the inset of Fig. 4.19, where we report the energy difference between the stripe and the FL phase (black points). For values of  $k_F r_0$  in the vicinity of the freezing density the stripe phase is never energetically favorable compared to neither the FL nor the WC phase (the exact values of stripes energy are shown in Table 4.1. The very small region of phase coexistence in the present system is an evidence of the fact that melting of the WC does not involve the appearance of microemulsion phases. Finally, it is worth to mention that a QMC search for stripes (similar to ours) in the 2D Coulomb gas [111] does not indicate the existence of such *stable* phase at  $T = 0$ .

## 4.7 Correlation functions

To complete the analysis of the properties of the system it is important to calculate not only the energy of the ground state, but also correlation functions such as the pair-distribution function, the static structure factor and the momentum distribution.

Let us start from the radial pair-distribution function  $g(r)$  giving the probability of finding two particles at a distance  $r$ . Results for different values of  $k_F r_0$  in the FL phase are shown in Fig. 4.20. One should notice that by increasing the interaction strength the short-range repulsion increases and a shell structure starts to appear when approaching the freezing density. Fig. 4.20 contains also  $g(r)$  deep in the crystal phase. The existence of long-range

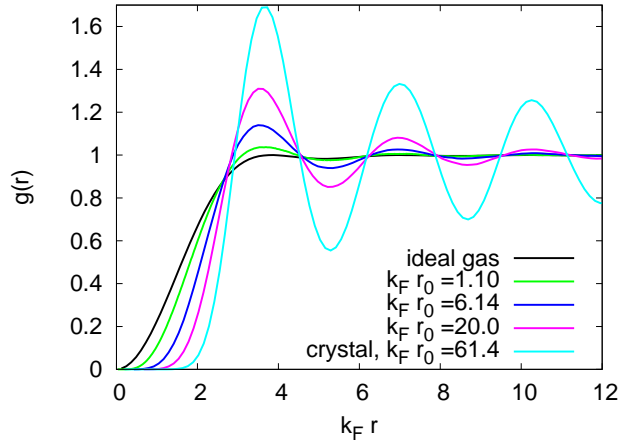


Figure 4.20: Pair correlation function in the liquid (for 49 particles) and in the crystal (for 56 particles) phase. The pair correlation function of the non-interacting gas is also shown.

ordering can be seen from the oscillating behavior of  $g(r)$  at large  $r$ .

Furthermore, it is possible to study the dependence on  $x$  and  $y$  in the pair-distribution function. An example of the DMC estimate of such two-dimensional distribution function is shown in Fig. 4.21 for FL, WC and stripe phases. One can easily see the absence of any long-range correlations in the FL phase and a clear triangular lattice structure for the WC phase. For the stripes  $g(x, y)$  shows long-range ordering only along the  $y$ -direction as it was imposed by construction from the trial wave function.

The Fourier transform of  $g(r)$  yields the static structure factor  $S(\mathbf{k}) = 1 + n \int d\mathbf{r} e^{i\mathbf{k}\cdot\mathbf{r}} [g(r) - 1]$ . This quantity can also be calculated directly in the FNDMC algorithm by evaluating the average of the product of density fluctuation operators  $NS(\mathbf{k}) = \langle \rho_{\mathbf{k}} \rho_{-\mathbf{k}} \rangle = \langle \sum_{i,j} e^{i\mathbf{k}\cdot(\mathbf{r}_i - \mathbf{r}_j)} \rangle$  (for more details see Chapter 3). Results are reported in Fig. 4.22 for both estimators. For large values of  $k_F r_0$  the direct estimator exhibits a more pronounced peak compared to the smoother Fourier transform at the wave vector corresponding to the lowest non-zero reciprocal lattice vector of the triangular lattice.

Fig. 4.23.a shows the momentum distribution directly calculated in the FNDMC algorithm at different values of the interaction strength for the liquid and crystal phase. One can see the typical behavior for Fermi liquid: the discontinuity of  $n(k)$  at  $k = k_F$  decreases with the increase of  $k_F r_0$ , but always stays finite even very close to the phase transition point. On the contrary, the momentum distribution for the crystal does not have any discontinuity, meaning that when the phase transition occurs the Fermi system completely loses any memory about the Fermi surface. Fig. 4.23.b presents an example

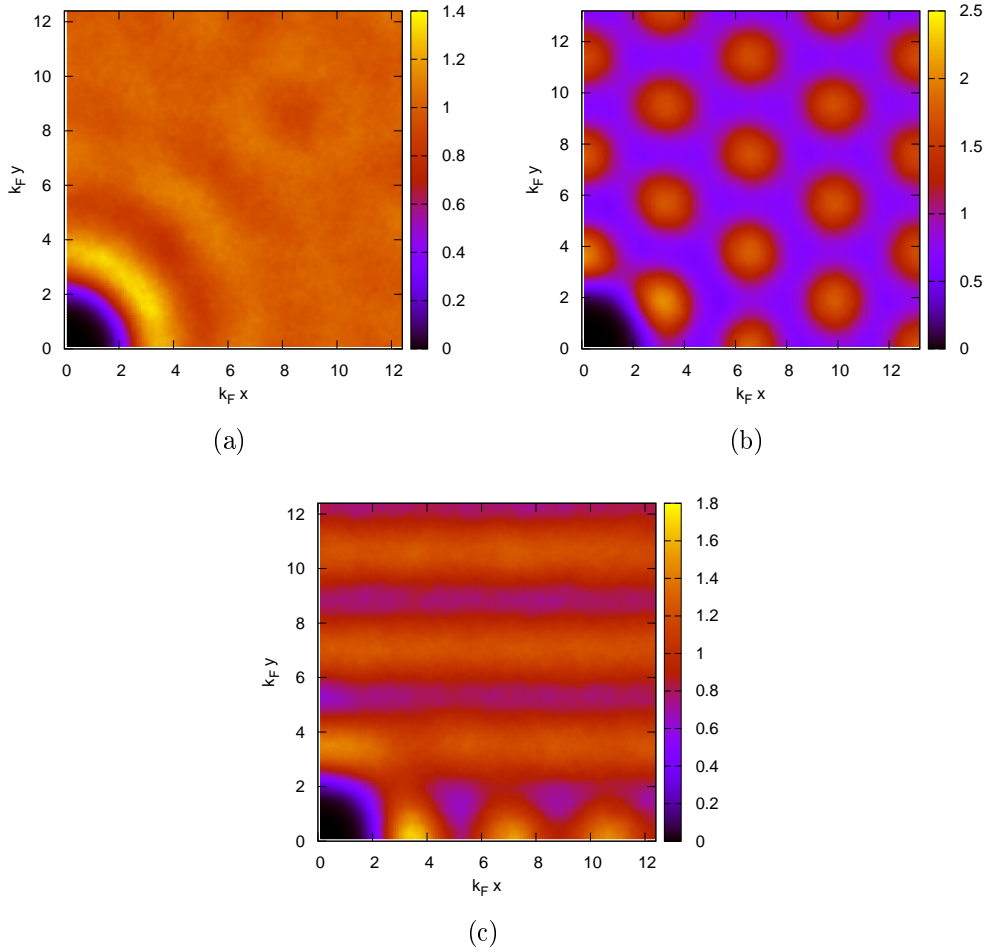


Figure 4.21: Two dimensional pair-distribution function  $g(x, y)$  in the liquid (a), crystal (b) and striped phase (c). Here  $k_F r_0 = 20.05303$  for FL and stripes and 49 particles are used; for WC  $k_F r_0 = 34.73$  and 56 particles are used.

of the dependence of  $n(k)$  on the system size near the phase transition point. It is clear from Fig. 4.23.b that there is no essential dependence of  $n(k)$  on the system size. This fact is a peculiar property of 2D dipolar Fermi systems, since, for example, in a 2D Coulomb gas the momentum distribution has a very strong dependence on the number of particles [116]. Another important characteristic of the system is the one-body density matrix which is shown in Fig. 4.24 for the FL and WC phases.

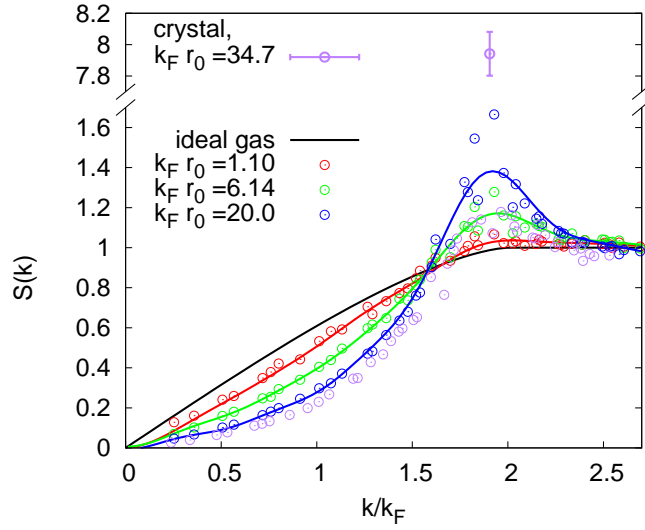


Figure 4.22: Static structure factor in the liquid (for 49 particles) and in the crystal (for 56 particles) phase. In the liquid phase, solid lines correspond to the Fourier transform of  $g(r)$  while symbols correspond to the direct calculation of  $S(k)$ . The static structure factor of the non-interacting gas is also shown.

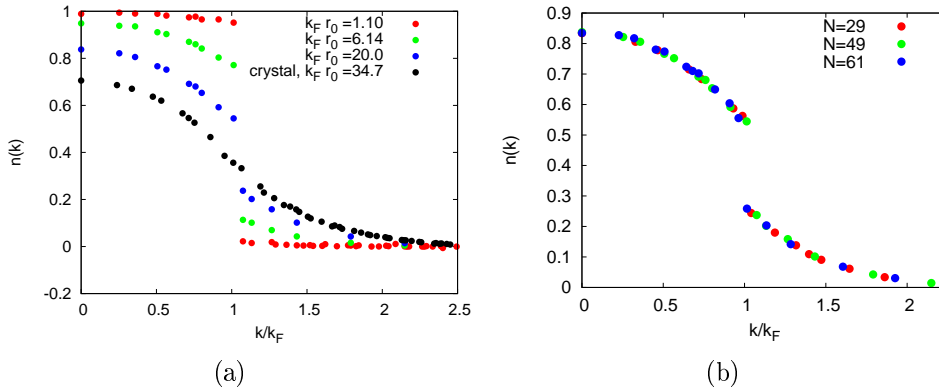


Figure 4.23: Momentum distribution for liquid (for 49 particles) and for crystal (for 56 particles) at different  $k_F r_0$  5.10(a); momentum distribution for FL for different system size at  $k_F r_0 = 20.053$  5.10(b).

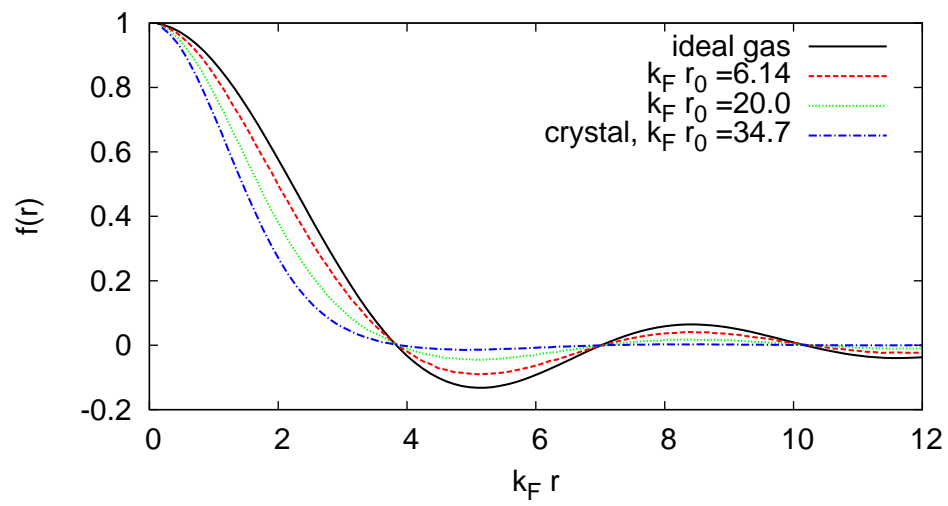


Figure 4.24: One-body density matrix in the liquid (for 49 particles) and in the crystal (for 56 particles) phase.



# The impurity problem

---

In this chapter we study 2D dipolar fermions in a bilayer configuration, where the dipole moments are polarized perpendicular to the planes. We consider an extreme case of the population imbalance when the top layer contains only one particle and the bottom layer has many particles. The dipolar interaction between particles in the bottom layer has a purely repulsive character, but the interlayer interaction has an attractive part. Therefore, this system represents an interesting impurity problem with long-range anisotropic interactions. We consider the bottom layer fermions to be in the weakly interacting regime, therefore they are in the Fermi liquid phase. The partially attractive interaction between the impurity and fermions of the bottom layer leads to an effective mass of the impurity larger than its bare mass. Using the FNDMC method we calculate the chemical potential of the impurity, as well as its effective mass, as a function of the intralayer interaction strength. Also, the pair-correlation function for the impurity and the bottom layer particles is obtained.

## 5.1 Introduction

We consider two 2D layers (Fig. 5.1), where the bottom layer B contains  $N$  identical fermionic particles of mass  $m$  and the top layer A has only one fermion of the same type, which is further called the "impurity". The fermions in both layers have electric or magnetic dipole moment  $d$ , which is oriented perpendicular to the plane of motion by an external field. The interaction potential of the impurity  $p$  and a particle  $i$  from the layer B is

$$V_{imp}(r_{pi}) = \frac{d^2(1 - 3 \cos^2(90^\circ - \theta))}{R^3} = \frac{d^2(r_{pi}^2 - 2\lambda^2)}{(r_{pi}^2 + \lambda^2)^{5/2}}, \quad (5.1)$$

where  $R$  is the distance between particles  $p$  and  $i$ ,  $r_{pi}$  is the inlayer distance between particle  $i$  and the projection of particle  $p$  to the layer B,  $\theta$  is the angle between the direction  $R$  and the layer B,  $\lambda$  is the distance between layers A and B. The Hamiltonian of the system is

$$H = -\frac{\hbar^2}{2m} \sum_{i=1}^{N+1} \nabla_i^2 + \sum_{i<j}^{j=N} \frac{d^2}{r_{ij}^3} + \sum_{i=1}^N V_{imp}(r_{pi}), \quad (5.2)$$

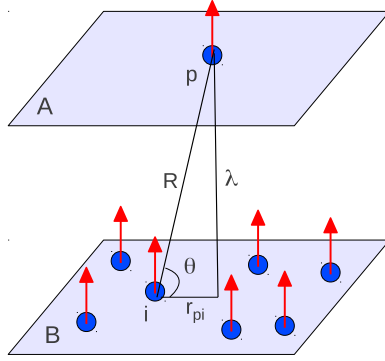


Figure 5.1: Two 2D layers of one-component fermions with the dipolar moment oriented perpendicular to the plane.

where  $r_{ij}$  is the distance between the particles  $i$  and  $j$  which belong to the layer B.

The strength of the intra- and inter- layer dipolar interaction is conveniently expressed in terms of the dimensionless parameter  $k_F r_0$  and  $k_F \lambda$ , respectively. Here  $r_0 = md^2/\hbar^2$  is the characteristic length of the dipole-dipole force and  $k_F = \sqrt{4\pi n}$  is the Fermi wave vector of the 2D gas determined by the density  $n$  in layer B.

Our main goal is to calculate the chemical potential  $\mu$  of the impurity and its effective mass  $m^*$  at zero temperature by means of the FNDMC method (Chapter 3). The chemical potential is defined as

$$\mu = E_{N+1} - E_N, \quad (5.3)$$

where  $E_{N+1}$  is the ground state energy of the present bilayer system and  $E_N$  is the ground state energy of a 2D dipolar Fermi liquid (see Chapter 4).

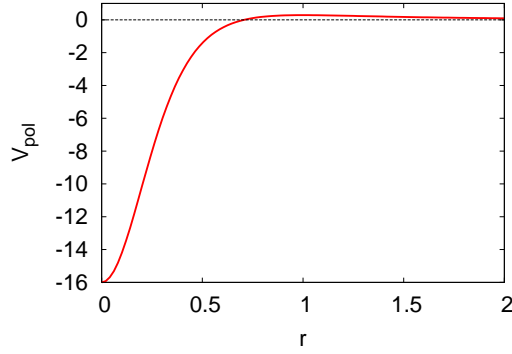
The energies are expressed in units of the Hartree-Fock energy (4.2) per particle

$$\varepsilon_{HF} = \frac{E_{HF}}{N} = \frac{E_F}{2} \left( 1 + \frac{128k_F r_0}{45\pi} \right), \quad (5.4)$$

where  $E_F = \frac{\hbar^2 k_F^2}{2m}$  is the Fermi energy of a 2D noninteracting Fermi gas. Sometimes we also use the units of energy  $\frac{\hbar^2}{mr_0^2}$ .

## 5.2 Two-body problem

In this section we consider the two-body problem for the potential  $V_{imp}(r)$ . We are interested in the bound state solutions. In polar coordinates the

Figure 5.2: Potential  $V_{pol}(r)$  at  $\lambda = 0.5$ .

corresponding Schroedinger's equation is

$$\left(-\frac{\hbar^2}{m} \Delta + V_{imp}(r)\right) \Psi(r, \phi) = E_b \Psi(r, \phi), \quad (5.5)$$

where  $\Psi(r, \phi)$  is a two-body wave function,  $r \equiv r_{pi}$ ,  $\phi$  is the polar angle and  $E_b$  is the energy of the bound state. After the usual substitution  $\Psi(r, \phi) = \chi(r)\Phi(\phi)$  the equation (5.5) becomes

$$-\frac{d^2\chi(r)}{dr^2} - \frac{d\chi(r)}{rdr} + V_{imp}(r)\chi(r) = E_b\chi(r), \quad (5.6)$$

where  $r$  and  $\lambda$  are in units of  $r_0$ ,  $E_b$  and  $V_{imp}(r)$  are in units of  $\frac{\hbar^2}{mr_0^2}$ . Here only the s-wave scattering is taken into account, therefore there is no dependence on the angle  $\phi$ .

The potential  $V_{imp}(r)$  is attractive at small  $r$  and repulsive at large  $r$  (Figure 5.2). Also it satisfies the following condition

$$\int V_{imp}(r)rdr = 0. \quad (5.7)$$

In Ref. [117] it was shown that the potential (5.1) always has at least one bound state. In the regime of  $\lambda \gg 1$  the Schroedinger's equation (5.6) has only one shallow bound state, whose energy was approximately calculated in Ref. [118]

$$E_{b1} \approx \frac{\hbar^2}{mr_0^2} \exp(-8\lambda^2 + 8.533333\lambda - 6.75662 + O(1/\lambda)) \quad (5.8)$$

In the limit  $\lambda \ll 1$  the potential (5.1) has many bound states [118]. The energy of the lowest one was obtained in Ref. [118]

$$E_{b2} = \frac{\hbar^2}{mr_0^2} \frac{2}{\lambda^3} (1 - \sqrt{6\lambda}). \quad (5.9)$$

In order to determine numerically the ground-state eigenfunction and eigenenergy of the Schroedinger's equation one can use the well-known technique called the shooting method [119]. In the following we give a brief description of it.

First, let us define the boundary conditions which the solution of the Schroedinger's equation (5.6) should satisfy. We require  $\chi$  be everywhere finite and also that  $\chi'(0) = 0$ . In order to determine the eigenfunctions and eigenvalues, we need a boundary condition at  $r \rightarrow \infty$ . Numerically, of course, one needs to use a cut-off value  $r_{max}$  of the coordinate  $r$ . Since we are interested in a bound state solution, which decays exponentially at large  $r$ , where  $V_{imp}(r)$  in Eq. (5.6) can be neglected. Therefore, one can simply take  $\chi(r_{max}) = 0$ . It is important to notice that the accuracy and stability of the results must be checked by varying the value of  $r_{max}$ .

Then we need to guess a value  $E_b$  for the ground state energy and numerically integrate Eq. (5.6) from  $r = r_{max}$  towards the origin  $r = 0$ . Fig. 5.3.a shows an example of the solutions of Eq. (5.6) for a set of values of  $E_b$ . Then we need to plot the corresponding values of  $\chi'(0)$  versus  $E_b$ , as it is done in Fig. 5.3.b. The point where the curve crosses the axis of  $E_b$  defines the value of the ground-state energy.

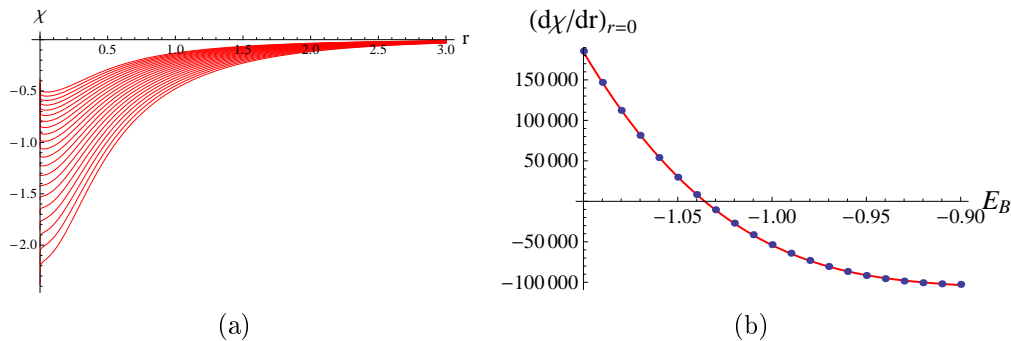


Figure 5.3: The details of the shooting method: the solutions of Eq. (5.6)  $\chi(r)$  for a set of values of  $E_b$  (a), the dependence of  $\chi'(0)$  on  $E_b$  (b). The bound state energy is defined as the point where  $\chi'(0) = 0$ .

Fig. 5.4 shows the dependence of the bound state energy of the Schroedinger's equation (5.5) on  $\lambda$  (the black points), which was calculated by the shooting method. They are in perfect agreement with the numerical results for  $E_b$  which are obtained in Ref. [120]. The above mentioned analytical expressions for the binding energy  $E_{b1}$  and  $E_{b2}$  are plotted in Fig. 5.4 with lines.

### 5.3. Perturbative calculation of the impurity chemical potential 79

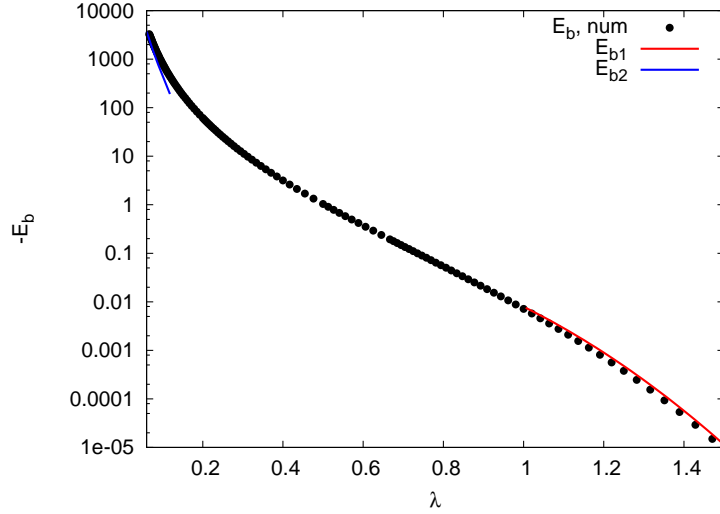


Figure 5.4: The dependence of the ground state binding energy  $E_b$  on  $\lambda$ . The energy is in the units of  $\frac{\hbar^2}{mr_0^2}$ .

### 5.3 Perturbative calculation of the impurity chemical potential.

Before going to the details of the FNDMC calculation, we discuss the perturbative calculation of the chemical potential of the impurity  $\mu$  in the limit of large distance  $\lambda$ . The prediction of the perturbative expansion is a good benchmark for the FNDMC results. We base this section on Ref. [121], where the chemical potential of the impurity was calculated up to second order on the small parameter  $\frac{1}{\lambda}$ . In the following we briefly review this calculation.

The property (5.7), due to the partially attractive and partially repulsive character of the impurity potential  $V_{imp}$ , leads to the vanishing of the first order term in the perturbative expansion on  $\frac{1}{\lambda}$ . The second order term can be calculated as

$$\mu_2 = \frac{2m}{\hbar^2 V} \sum_{\mathbf{p}} f_{\mathbf{p}} \sum_{\mathbf{q} \neq 0} \frac{(1 - f_{\mathbf{p}+\mathbf{q}}) |V(\mathbf{q})|^2}{\mathbf{p}^2 - (\mathbf{p} + \mathbf{q})^2 - \mathbf{q}^2}, \quad (5.10)$$

where  $f_p$  denotes the Fermi-distribution at zero temperature,  $\mathbf{p}$  is the momentum of a particle of layer B and  $V(\mathbf{q})$  is the Fourier transform of the impurity potential (5.1). The above equation comes from standard perturbation theory for the second-order correction to the ground-state energy

$$E_2^0 = \sum_{n \neq 0} \frac{|V_{0n}|^2}{E_0 - E_n}, \quad (5.11)$$

where  $V_{0n}$  is the matrix element  $\langle 0|V_{imp}|n\rangle$  and  $E_n$  are the excited-states energies.

In Eq. (5.10) the summation goes over the states where the impurity is transferring momentum  $\mathbf{q}$  to a fermion of the layer B which carries momentum  $\mathbf{p}$ . Due to the Pauli exclusion principle, the final momentum should lie outside the Fermi sphere, hence the factor  $1 - f_{\mathbf{p}+\mathbf{q}}$ . The denominator in Eq. (5.10) is the energy difference between the ground and excited states:  $E_0 - E_n = \frac{\hbar^2}{2m}(\mathbf{p}^2 - (\mathbf{p} + \mathbf{q})^2 - \mathbf{q}^2)$ .

We rewrite Eq. (5.10) in the form of an integration over  $\mathbf{q}$  and  $\mathbf{p}$  in polar coordinates

$$\mu_2 = -\frac{2m}{\hbar^2 V} \cdot \frac{V^2}{(2\pi\hbar)^4} \int_0^{k_F} \int_{-\pi}^{\pi} p dp d\theta_1 \int_{q_{min}}^{\infty} \int_{-\pi}^{\pi} q dq d\theta_2 \frac{|V(q)|^2}{2p q \cos \alpha - 2q^2}, \quad (5.12)$$

where  $\alpha = \pi - \theta_2$ , and  $q_{min}$  is the minimal value of  $|\mathbf{q}|$ , such that  $|\mathbf{p} + \mathbf{q}| > k_F$ , see Fig. 5.5. Substituting the Fourier transform of Eq. (5.1),  $V(q) =$

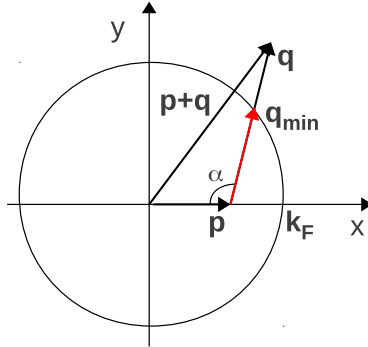


Figure 5.5: Fermion in layer B receiving the momentum  $\mathbf{q}$ .

$2\pi d^2 q e^{-\lambda q}$ , and integrating over  $\theta_1$  one obtains

$$\mu_2 = \frac{\hbar^2}{m r_0^2} \cdot \frac{V}{2\pi} \int_0^{k_F} p dp \int_{-\pi}^{\pi} d\alpha \int_{q_{min}}^{\infty} dq \frac{q^2 e^{-2\lambda q}}{p \cos \alpha - q}. \quad (5.13)$$

The integral over  $q$  can be done analytically, while the integrations over  $\alpha$  and  $p$  are performed numerically. We compare the results of this calculation to the ones obtained with the FNDMC method in Section 5.6.

It is worth noticing here that the above calculation of the chemical potential is expected to be valid only in the weakly interacting regime  $k_F r_0 < 1$ . For larger values of  $k_F r_0$  the Fermi-distribution  $f_p$  should be replaced with the

momentum distribution for the Fermi liquid containing the renormalization factor  $Z$  and the effective mass of quasiparticles  $m^*$  should be used instead of the bare mass  $m$ . Both  $Z$  and  $m^*$  were calculated in Chapter 4.

## 5.4 Trial wave function and its optimization

The trial wave function for the impurity problem is chosen as a Slater-Jastrow wave function of the form

$$\Psi_T = \prod_{i=1}^N h(r_{pi}) \Psi_{FL}. \quad (5.14)$$

Here  $\Psi_{FL}$  is the trial wave function (4.8), which is used in Chapter 4 to calculate the ground state properties of the FL phase,  $r_{pi}$  is the same as in Eq. (5.1) and  $h(r_{pi})$  is a Jastrow correlation term which accounts for the interlayer interaction. We choose it as (see Fig. 5.6)

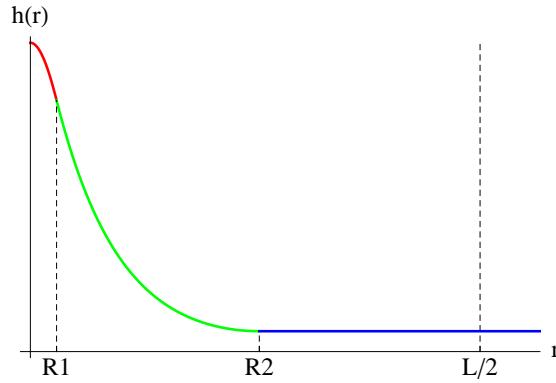


Figure 5.6: Two-body wave function  $h(r)$  for the intralayer interaction.

$$h(r) = \begin{cases} h_1 = e^{-\gamma r^2} & r < R_1 \\ h_2 = \frac{C}{2}(e^{-\alpha(r-R_2)} + e^{\alpha(r-R_2)}) & R_1 < r < R_2 \\ C & r > R_2 \end{cases} \quad (5.15)$$

with the matching conditions

$$\begin{aligned} h_1(r = R_1) &= h_2(r = R_1) \\ h'_1(r = R_1) &= h'_2(r = R_1). \end{aligned} \quad (5.16)$$

Here  $C$ ,  $R_1$ ,  $R_2$ ,  $\gamma$ ,  $\alpha$  are parameters. Two of them ( $\alpha$  and  $R_1$ ) are determined by the conditions Eq. (5.16), and the three others ( $\gamma$ ,  $C$  and  $R_2$ ) should be optimized by the VMC method. This optimization is done using the iteration

method. Its essence is to minimize a wave function with respect to only one parameter at the time keeping the others as constants. After a minimum on this parameter is found, the minimization is performed on the second parameter. This procedure is repeated until the algorithm converges. Fig. 5.7 shows an example of the optimization. The disadvantage of this minimization procedure is that the algorithm can find a local minimum instead of the global one.

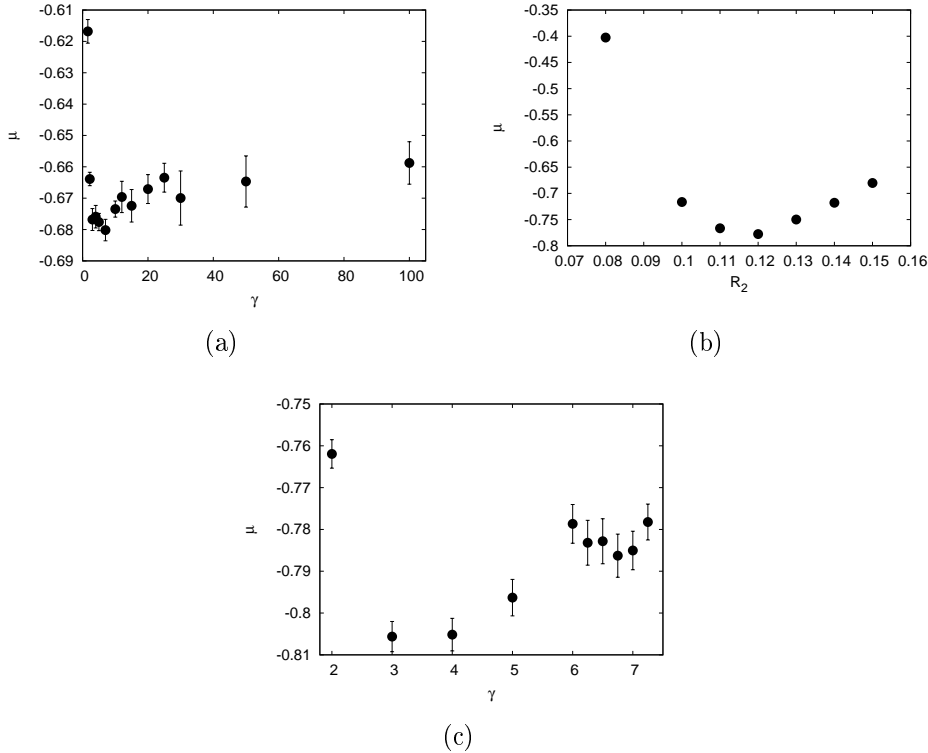


Figure 5.7: Three iterations of the VMC optimization of  $h(r)$  at  $k_F r_0 = 0.5$  and  $\lambda = 0.5$ : the minimization on  $\gamma$  at  $C = 0.7$ ,  $R_2 = 0.15\frac{L}{2}$  (a), then on  $R_2$  at  $\gamma = 7$ ,  $C = 0.7$  (b) and again on  $\gamma$  at  $C = 0.066$  and  $R_2 = 0.12\frac{L}{2}$  (c).

## 5.5 Calculation of the potential energy

The intralayer potential energy (the second term in Eq. 5.2) is calculated using the same technique discussed in Section 4.2. The only difference is the use of  $L_{cut} = 0.5L$  instead of  $L_{cut} = 2L$ . We checked that  $L_{cut} = 0.5L$  is large enough once the difference  $E_{N+1} - E_N$  is taken.

The interlayer potential energy (the third term in Eq. 5.2) is also treated using the same technique and the tail energy for the impurity potential is

given by

$$\frac{E_{tail}^{imp}(m)}{N} = \frac{1}{2} \int_{mL_x}^{\infty} \frac{d^2(r^2 - 2\lambda^2)}{(r^2 + \lambda^2)^{5/2}} g_{imp}(r) n 2\pi r dr, \quad (5.17)$$

where  $L_x$  is the smallest size of the simulation box,  $m$  is an integer number and  $g_{imp}(r)$  is the pair-correlation function between the impurity and the fermions of layer B. After the replacement of  $g_{imp}(r)$  by its average value in the bulk  $g_{imp}(r) = 1$ , Eq. (5.17) becomes

$$E_{tail}^{imp} = \frac{\hbar^2}{mr_0^2} \frac{2\pi m^2 N}{(\lambda^2 + \frac{m^2 N}{nr_0^2})^{3/2}}. \quad (5.18)$$

We use  $m = 2$  for the calculation of the interlayer potential energy and we checked that the use of larger values of  $m$  gives the same estimate of the chemical potential within statistical uncertainty.

## 5.6 Chemical potential of the impurity

In this section the main results for the chemical potential of the impurity are discussed. Using the FNDMC technique (Chapter 3) we calculate the ground state energy  $E_{N+1}$  of the system which contains  $N = 29$  particles in layer B and the impurity in layer A. The trial wave function was already discussed in Section 5.4 (see Eq. (5.14)). We use the same time-step  $dt$ , average number of walkers  $N_w$  and variational parameter  $R_p$  of the Jastrow part as it is done for the study of the pure FL phase. The chemical potential  $\mu$  is calculated using Eq. (5.3), where  $E_N$  is the ground-state energy of 29 fermions in the FL phase (discussed in Chapter 4). It was checked that the calculation with  $N = 49$  and  $N = 61$  particles in layer B gives the same estimate of  $\mu$  within statistical uncertainty.

Fig. 5.8 reports the FNDMC results for the chemical potential of the impurity at  $k_F r_0 = 0.5$  (red points) and at  $k_F r_0 = 2.5$  (green points) as a function of the interlayer distance  $k_F \lambda$ . The logarithmic scale is used for the  $y$ -axis. The solid lines show the energy of the two-body bound state  $E_b$  (see Section 5.2) in units of  $\varepsilon_{HF}$  (5.4): the red one corresponds to  $k_F r_0 = 0.5$  and the green one to  $k_F r_0 = 2.5$ . The dashed lines are the results of the perturbative calculation of the chemical potential Eq. (5.13). One can see that at small  $\lambda$  the chemical potential of the impurity approaches  $E_b$  meaning that the impurity forms a bound state with one fermion from layer B. At large  $\lambda$  the chemical potential of the impurity approaches instead the perturbative result. Surprisingly, we still find the agreement with the perturbation expansion (5.13) at  $k_F r_0 = 2.5$ . At the intermediate interlayer distance the FNDMC values of  $\mu$  deviate both from  $tE_b$  and from Eq. (5.13).

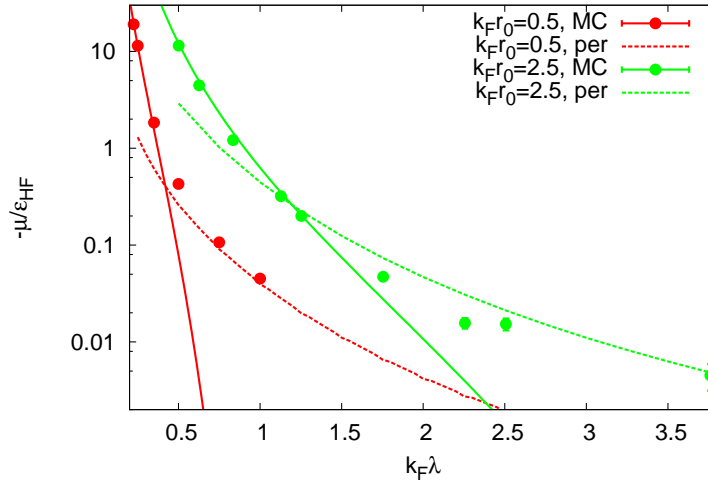


Figure 5.8: Chemical potential of the impurity  $\mu$  at  $k_F r_0 = 0.5$  (the red points) and at  $k_F r_0 = 2.5$  (the green points) as a function of the inter-layer distance  $\lambda$ . The solid lines are the energy of two-body bound state in units of  $\varepsilon_{HF}$ , the dashed lines are the perturbation expansion  $\mu_2$ .

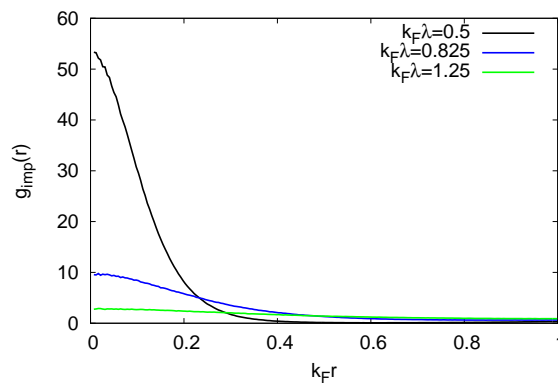


Figure 5.9: The pair-correlation function for the impurity  $g_{imp}(r)$  for the different inter-layer distances  $k_F \lambda$  at  $k_F r_0 = 2.5$ .

The results for the pair-correlation function  $g_{imp}(r)$  at different interlayer distances are shown in Fig. 5.9 for  $k_F r_0 = 2.5$ . They are obtained from the VMC and DMC estimates of  $g_{imp}(r)$  using the usual extrapolation technique (see Chapter 3). One can see from Fig. 5.9 that the peak in  $g_{imp}(r)$  becomes higher by decreasing  $\lambda$ , which reflects the increase of the attraction between the impurity and the fermions of layer B closer to it.

## 5.7 Effective mass of the impurity

In this section the effective mass of the impurity  $m^*$  is discussed. The effective mass is obtained in the FNDMC calculation from the diffusion coefficient of the impurity in imaginary time, as it was done in Ref. [122], where the calculation of the effective mass of one  $^3\text{He}$  atom in superfluid  $^4\text{He}$  was performed. More precisely,  $m^*$  can be defined in the following way

$$\frac{m}{m^*} = \lim_{\tau \rightarrow \infty} \frac{\langle |\mathbf{r}_{imp}(\tau) - \mathbf{r}_{imp}(\mathbf{0})|^2 \rangle}{4D\tau}. \quad (5.19)$$

Here  $\tau$  is the imaginary time,  $D = \frac{\hbar^2}{2m}$  is the diffusion constant (see Section 3.5),  $\mathbf{r}_{imp}(\tau)$  is the vector of the impurity displacement. Fig. 5.10 shows the dependence of the mean square impurity displacement  $\langle \Delta r_{imp}^2 \rangle = \langle |\mathbf{r}_{imp}(\tau) - \mathbf{r}_{imp}(\mathbf{0})|^2 \rangle$  on  $\tau$  for  $k_F r_0 = 0.5$  (a) and for  $k_F r_0 = 2.5$  (b). This dependence can be fitted using the following function

$$s(\tau) = a_1 + \frac{a_2}{\tau}(1 - e^{-a_3\tau}), \quad (5.20)$$

where  $a_1, a_2, a_3$  are fitting constants and  $\frac{1}{a_1} = m^*/m$ . The black lines in Fig. 5.10 correspond to the fits using Eq. (5.20).

The results for the effective mass, which are extracted from Fig. 5.10, are shown in Fig. 5.11. One can see that the effective mass rapidly increases starting from a critical value of  $k_F \lambda$  which depends on  $k_F r_0$ .

## 5.8 Conclusion

We considered the impurity problem of a 2D dipolar bilayer Fermi gas in the weakly interacting regime. The chemical potential of the impurity, its effective mass and the pair-correlation function were calculated at different interlayer distances. We found that the chemical potential of the impurity agrees with the results of the perturbation expansion at large distances and it approaches the energy of the two-body bound state at small distances. The rapid increase of the effective mass starting from a critical value of  $k_F \lambda$  was

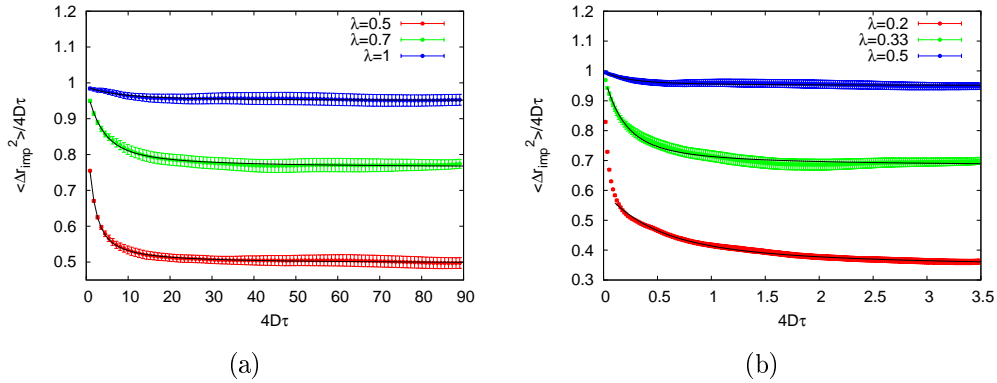


Figure 5.10: The dependence of the mean square impurity displacement  $\langle \mathbf{r}_{\text{imp}}^2 \rangle$  on  $\tau$ : at  $k_F r_0 = 0.5$  for  $\lambda = 0.5, 0.7, 1$  (a) and at  $k_F r_0 = 2.5$  for  $\lambda = 0.2, 0.33, 0.5$ . The black solid lines show the fits using  $s(\tau)$ .

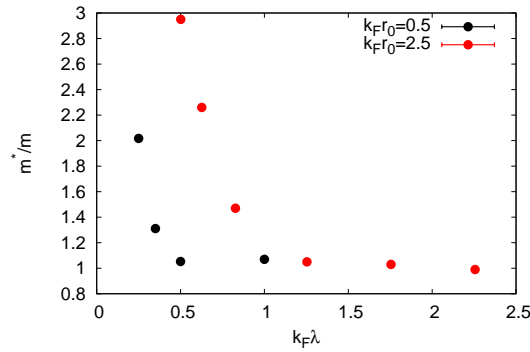


Figure 5.11: The dependence of  $m^*$  on  $k_F \lambda$  at  $k_F r_0 = 0.5$  (the black points) and at  $k_F r_0 = 2.5$  (the red points).

also observed. An interesting extension of the following work is to consider the strongly interacting regime and in particular the crystal phase, where the impurity is coupled to the phonon modes of the crystal.

# Twist-averaged boundary conditions

---

The choice of boundary conditions is very important for the simulation of an infinite system, because the appropriate boundary conditions can simplify the extrapolation to the thermodynamic limit. The periodic boundary condition (PBC) means that the wave function keeps the same phase when a particle crosses the border of the simulation box and its image particle enters the simulation box on the opposite side. For a Fermi liquid using PBC, the convergence of energy to the thermodynamic limit is quite slow, as it can be easily demonstrated for an ideal gas. One of the ways to improve the convergence to the infinite system size is to use twist-averaged boundary conditions (TABC), which means that the wave function should get a phase when a particle wraps around the boundaries. As it was shown in Ref. [113], the finite-size shell effects are greatly reduced for a degenerate Fermi liquid if one averages over twist angles. Further, we will discuss the details of the calculation of energy using TABC in an example of the ideal 2D gas.

Let us consider a 2D ideal Fermi gas in a square box of size  $L$ . If one applies PBC the single-particle states have wave vectors  $\mathbf{k}_\mathbf{n} = \frac{2\pi\mathbf{n}}{L}$  (the circles in Fig. A.1). One can consider another set of single-particle states  $\mathbf{q}_\mathbf{n} = \frac{2\pi\mathbf{n}+\theta}{L}$ , which satisfy the twist boundary conditions (the triangles in Fig. A.1). Each component of twist vector  $\theta$  belongs to the interval  $-\pi, \pi$ . Figure A.1 schematically shows the momenta of five fermions with PBC (red filled circles) and for one twist vector (red triangles). In this case the number of particles is conserved corresponding to the canonical ensemble description. For each twist angle the five fermions will fill the five lowest states. So, after the average over many twist vectors the Fermi surface will be almost filled leading to the reduction of finite-size errors in kinetic energy.

Fig. A.2 illustrates the convergence of the relative error in energy  $\Delta E = |\frac{E_N}{E_{th}} - 1|$ , where  $E_N$  is the energy for  $N$  particles and  $E_{th}$  is the energy for an infinite system. The red (green) points are  $\Delta E$  for PBC (TABC). It can be clearly seen that using TABC the averaged energy converges much faster to the thermodynamic limit.

Another way of using TABC is to work in the grand-canonical ensemble (GCE TABC), which in practice means that the number of occupied states

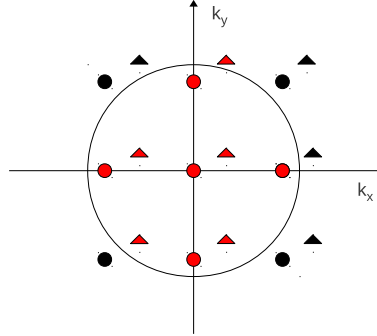


Figure A.1: Momenta of five fermions with PBC and for canonical ensemble TABC (one given twist angle). Red (black) circles are filled (empty) states for PBC and red (black) triangles are filled (empty) states for TABC. The large circle shows the Fermi surface for an infinite system.

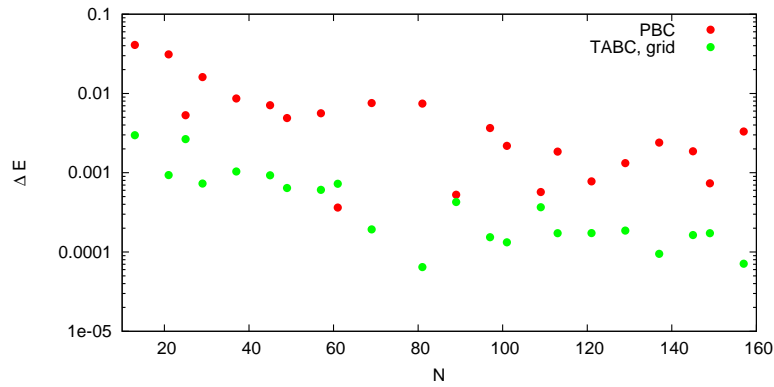


Figure A.2: Relative error  $\Delta E = \left| \frac{E_N}{E_{th}} - 1 \right|$  for an ideal gas energy for PBC (red points) and canonical ensemble TABC (green points).

can be different for the different twist vectors. In this case the procedure of choosing single-particle states for each twist is different from the canonical TABC. More exactly only states which lay within the Fermi surface are occupied.

In Fig. A.3 GCE TABC states of five particles are schematically shown for three different twist vectors.

There is a possibility to reduce the numbers of twists in GCE TABC [114]. The trial wave function can be written as:

$$\Psi_T(\mathbf{r}_1, \dots, \mathbf{r}_N, \theta) = \exp \left( \sum_{i=1}^{n_p} (i\theta_x x_i + i\theta_y y_i) \Psi_{\{\mathbf{k}_p\}}(\mathbf{r}_1, \dots, \mathbf{r}_N) \right), \quad (\text{A.1})$$

where  $\{\mathbf{k}_p\}$  are the PBC wave vectors before applying the shift  $\theta = (\theta_x, \theta_y)$ . For each set of  $\{\mathbf{k}_p\}$  there is a region (in the following it is called "pocket") of values of  $\theta_x, \theta_y$  such that only the momenta belonging to  $\{\mathbf{k}_p\}$  lay within the Fermi surface after the twist vector addition. The energy dependence on  $\theta$  is trivial within each pocket, so the average over all  $\theta_x, \theta_y$  can be performed:

$$E_p = \sum_{\theta_x, \theta_y} \frac{E_{\theta_x, \theta_y}}{N_x, N_y} = E_{\{\mathbf{k}_p\}} + (\langle \theta_x^2 \rangle + \langle \theta_y^2 \rangle) n_p - i \sum_{i=1}^{n_p} (k_{p_i}^x \langle \theta_x \rangle + k_{p_i}^y \langle \theta_y \rangle), \quad (\text{A.2})$$

where  $E_p$  is the average energy for a given pocket,  $E_{\{\mathbf{k}_p\}}$  is the energy calculated using only  $\Psi_{\{\mathbf{k}_p\}}(\mathbf{r}_1, \mathbf{r}_N)$ ,  $N_x, N_y$  are the number of the twist points  $\theta_x, \theta_y$  and  $n_p$  is the number of states in a given pocket. Here it is worth mentioning that  $E_{\{\mathbf{k}_p\}}$  has a nonzero imaginary part, but after the average over large enough number of configurations this becomes vanishingly small. Finally the GCE TABC energy  $E$  is given by

$$E = \sum_{i=1}^{N_{pock}} E_p^i W^i, \quad (\text{A.3})$$

where  $N_{pock}$  is the number of pockets for a given number of particles  $N$ ,  $W^i$  is the weight of a pocket  $i$  (the relative area in  $\theta_x, \theta_y$  space). It is important to notice that due to the projection and rotational symmetries pockets can be defined only for twist components  $\theta_x, \theta_y$  that belong to the interval  $[0, \pi]$  (not the whole region  $-\pi, \pi$ ). Therefore the total number of pockets can be reduced four times.

The change of occupied states for different pockets leads to the change of the size of the simulation box  $L$  (if the density  $n$  is kept fixed) or to the change

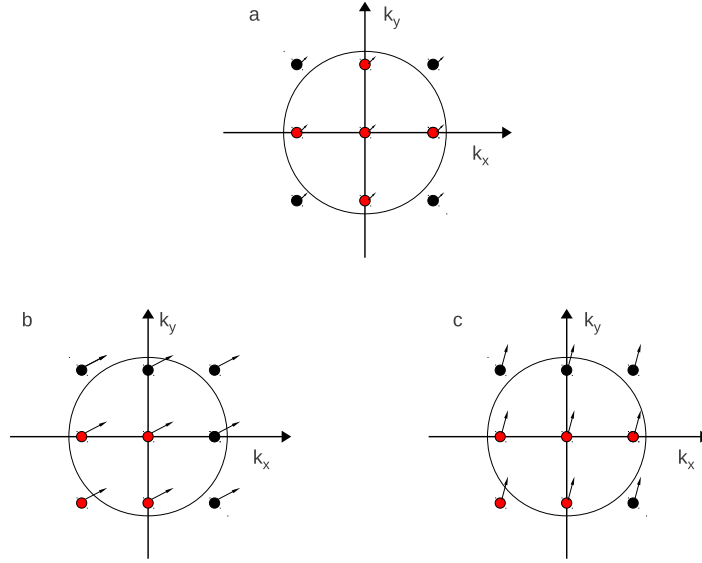


Figure A.3: Momenta of five fermions in GCE TABC for three different twist angles (the arrows are twist shifts of the initial PBC states, the red points are the filled states, the black points are the empty states).

of  $n$  (if  $L$  is fixed). In the last case the average over all densities (using the same formula (A.3)) becomes approximately equal to the background density. For noninteracting systems at a fixed  $L$  GCE TABC gives the exact  $E_{TL}$  in the limit of an infinite number of twists. In the first case ( $n$  is the same for any twists) GCE TABC does not give the exact  $E_{TL}$ , but shows a behavior similar to the case of canonical ensemble TABC (Fig. A.2). More precisely, the difference from  $E_{TL}$  always remains finite even if pockets are defined using a very fine grid (more than 30000 in every direction).

The use of TABC for the dipolar fermions is similar to the noninteracting case, because there is no dependence on  $\theta$  in the Jastrow part of the wave function. So, for each number of particles  $N$  the pockets can be defined as for an ideal gas and then the QMC calculation of  $E_p$  for the interacting fermions can be performed using the trial function  $\Psi_{\{\mathbf{k}_p\}}(\mathbf{r}_1, \mathbf{r}_N)$  as the Slater part. So, only one QMC run is sufficient for each pocket. The potential energy can be treated using the same technique discussed in Section 4.2. The tail energy is defined as

$$E_{tail} = \sum_{i=1}^{N_{pock}} E_{tail}^i W^i, \quad (\text{A.4})$$

where  $E_{tail}^i$  is the tail energy for  $i$ -th pocket calculated using Eq. (4.5) with the corresponding density and number of particles.

Fig. A.4 shows the finite size scaling of GCE TABC energies. Black points

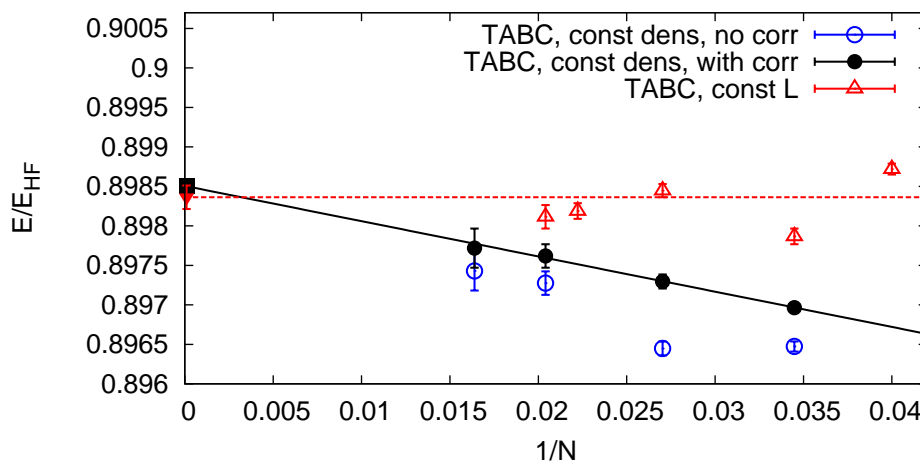


Figure A.4: GCE TABC energies for the implementation with fixed  $L$  and with fixed  $n$ . Here  $k_F r_0 = 1.1$ .

are the energies for the fixed density implementation with added corrections to the kinetic energy  $\Delta T_N$ . The extrapolation to the thermodynamic limit can be done using Eq. (4.9), but  $\Delta T_N$  is much smaller here than for the PBC case, and the effective mass can not be determined reliably. The result for  $E_{TL}$  can be obtained using a linear fit  $E = E_{TL} + a/N$ , which is shown by the black line. Blue circles are the fixed density GCE TABC energies without any correction  $\Delta T_N$ . Red triangles show instead the GCE TABC energies for the case of fixed  $L$ . No corrections are added here. Red dashed line is a fit by constant function which agrees with  $E_{TL}$  for fixed density case. The advantage of the fixed  $L$  implementation is that even using a small number of particles one can get a good estimate of  $E_{TL}$ . But there is a disadvantage: it is not clear which fitting function should be used, because the use of a constant does not look completely reliable. Due to this reason we use the fixed density implementation of GCE TABC.

Finally, it is important to notice, that the use of TABC makes the simulations at least twice more time consuming because one needs to use a complex wave function.



# Bibliography

- [1] M. H. Anderson, J. R. Ensher, M. R. Matthews, C. E. Wieman, and E. A. Cornell, "Observation of Bose-Einstein Condensation in a Dilute Atomic Vapor", *Science* **269**, 198, 1995.
- [2] K. B. Davis, M. -O. Mewes, M. R. Andrews, N. J. van Druten, D. S. Durfee, D. M. Kurn, and W. Ketterle, "Bose-Einstein Condensation in a Gas of Sodium Atoms", *Phys. Rev. Lett.* **75**, 3969, 1995.
- [3] B. DeMarco and D. S. Jin, "Onset of Fermi Degeneracy in a Trapped Atomic Gas", *Science* **285**, 1703, 1999.
- [4] F. Dalfovo, S. Giorgini, L. P. Pitaevskii, and S. Stringari, "Theory of Bose-Einstein condensation in trapped gases", *Rev. Mod. Phys.* **74**, 463, 1999.
- [5] S. Giorgini, L. P. Pitaevskii, S. Stringari, "Theory of ultracold atomic Fermi gases", *Rev. Mod. Phys.* **80**, 1215, 2008.
- [6] T. Lahaye, C. Menotti, L. Santos, M. Lewenstein, and T. Pfau, "The physics of dipolar bosonic quantum gases", *Rep. Prog. Phys.* **72**, 126401, 2009.
- [7] M. A. Baranov, M. Dalmonte, G. Pupillo, and P. Zoller, "Condensed matter theory of dipolar quantum gases", *Chem. Rev.* **112**, 5012, 2012.
- [8] N. Matveeva, A. Recati, and S. Stringari, "Dipolar drag in bilayer harmonically trapped gases", *Eur. Phys. J. D* **65**, 219-222, 2011.
- [9] N. Matveeva, and S. Giorgini, "Liquid and crystal phase of dipolar fermions in two dimensions", *Phys. Rev. Lett.* **109**, 200401, 2012.
- [10] M. Marinescu and L. You, "Controlling Atom-Atom Interaction at Ultralow Temperatures by dc Electric Fields", *Phys. Rev. Lett.* **81**, 4596, 1998.
- [11] S. Yi, and L. You, "Trapped atomic condensates with anisotropic interactions", *Phys. Rev. A* **61**, 041604, 2000.
- [12] S. Giovanazzi, A. Gorlitz, and T. Pfau, "Tuning the Dipolar Interaction in Quantum Gases", *Phys. Rev. Lett.* **89**, 130401, 2002.

- 
- [13] A. Micheli, G. Pupillo, H. P. Buchler, and P. Zoller, "Cold polar molecules in two-dimensional traps: Tailoring interactions with external fields for novel quantum phases", *Phys. Rev. A* **76**, 043604, 2007.
- [14] A. Micheli, Z. Idziaszek, G. Pupillo, M. A. Baranov, P. Zoller, and P. S. Julienne, "Universal Rates for Reactive Ultracold Polar Molecules in Reduced Dimensions", *Phys. Rev. Lett.* **105**, 073202, 2010.
- [15] A. Griesmaier, J. Werner, S. Hensler, J. Stuhler, and T. Pfau, "Bose-Einstein Condensation of Chromium", *Phys. Rev. Lett.* **94**, 160401, 2005.
- [16] K. Aikawa, A. Frisch, M. Mark, S. Baier, A. Rietzler, R. Grimm, and F. Ferlaino, "Bose-Einstein Condensation of Erbium", *Phys. Rev. Lett.* **108**, 210401, 2012.
- [17] M. Lu, N. Q. Burdick, S. H. Youn, and B. L. Lev, "Strongly Dipolar Bose-Einstein Condensate of Dysprosium", *Phys. Rev. Lett.* **107**, 190401, 2011.
- [18] M. Lu, N. Q. Burdick, and B. L. Lev, "Quantum Degenerate Dipolar Fermi Gas", *Phys. Rev. Lett.* **108**, 215301, 2012.
- [19] E. Timmermans, P. Tommasini, M. Hussein, and A. Kerman, "Feshbach resonances in atomic Bose-Einstein condensates", *Phys. Rep.* **315**, 199, 1999.
- [20] K.-K. Ni, S. Ospelkaus, M.H.G. de Miranda, A. Peer, B. Neyenhuis, J.J. Zirbel, S. Kotochigova, P.S. Julienne, D.S. Jin and J. Ye, "A High Phase-Space-Density Gas of Polar Molecules", *Science* **322**, 231, 2008.
- [21] S. Ospelkaus, K.-K. Ni, D. Wang, M.H.G. de Miranda, B. Neyenhuis, G. Quemener, P.S. Julienne, J.L. Bohn, D.S. Jin and J. Ye, "Quantum-State Controlled Chemical Reactions of Ultracold Potassium-Rubidium Molecules", *Science* **327**, 853, 2010.
- [22] K.-K. Ni, S. Ospelkaus, D. Wang, G. Quemener, B. Neyenhuis, M.H.G. de Miranda, J.L. Bohn, J. Ye and D.S. Jin, "Dipolar collisions of polar molecules in the quantum regime", *Nature* **464**, 1324, 2010.
- [23] M.-S. Heo, T.T. Wang, C.A. Christensen, T.M. Rvachov, D.A. Cotta, J.-H. Choi, Y.-R. Lee and W. Ketterle, "Formation of Ultracold Fermionic NaLi Feshbach Molecules", *Phys. Rev. A* **86**, 021602(R), 2012.
- [24] C.-H. Wu, J. W. Park, P. Ahmadi, S. Will, and M. W. Zwierlein, "Ultracold Fermionic Feshbach Molecules of  $^{23}\text{Na}^{40}\text{K}$ ", *Phys. Rev. Lett.* **109**, 085301, 2012.

- 
- [25] M. Repp, R. Pires, J. Ulmanis, R. Heck, E. D. Kuhnle, M. Weidemuller, E. Tiemann, "Observation of interspecies Li-Cs Feshbach resonances", *Phys. Rev. A* **87**, 010701, 2013.
- [26] K. Pilch, A. D. Lange, A. Prantner, G. Kerner, F. Ferlaino, H.-C. Nagerl, and R. Grimm, "Observation of interspecies Feshbach resonances in an ultracold Rb-Cs mixture", *Phys. Rev. A* **79**, 042718, 2009.
- [27] M. Saffman, T. G. Walker, and K. Molmer, "Quantum information with Rydberg atoms", *Rev. Mod. Phys.* **82**, 2313, 2010.
- [28] D. Comparat and Pillet, "Dipole blockade in a cold Rydberg atomic sample", *J. Opt. Soc. Am. B* **27**, A208, 2010.
- [29] S. Yi, and L. You, "Trapped condensates of atoms with dipole interactions", *Phys. Rev. A* **63**, 053607, 2001.
- [30] L. Santos, G. V. Shlyapnikov, P. Zoller, and M. Lewenstein, "Bose-Einstein Condensation in Trapped Dipolar Gases", *Phys. Rev. Lett.* **85**, 1791, 2000.
- [31] L. Santos, G. V. Shlyapnikov, P. Zoller, and M. Lewenstein, "Erratum: Bose-Einstein Condensation in Trapped Dipolar Gases [*Phys. Rev. Lett.* **85**, 1791 (2000)]", *Phys. Rev. Lett.* **89**, 139904, 2002.
- [32] S. Ronen, D. C. E. Bortolotti, J. L. Bohn, "Radial and Angular Rotons in Trapped Dipolar Gases", *Phys. Rev. Lett.* **98**, 030406, 2007.
- [33] K. Goral and S. Santos, "Ground state and elementary excitations of single and binary Bose-Einstein condensates of trapped dipolar gases", *Phys. Rev. A* **66**, 023613, 2002.
- [34] D. H. O'Dell, S. Giovanazzi, C. Eberlein, "Exact Hydrodynamics of a Trapped Dipolar Bose-Einstein Condensate", *Phys. Rev. Lett.* **92**, 250401, 2004.
- [35] L. Santos, G. V. Shlyapnikov, and M. Lewenstein, "Roton-Maxon Spectrum and Stability of Trapped Dipolar Bose-Einstein Condensates", *Phys. Rev. Lett.* **90**, 250403, 2003.
- [36] Zhen-Kai Lu and G.V. Shlyapnikov, "Fermi liquid of two-dimensional polar molecules", *Phys. Rev. A* **85**, 023614, 2012.
- [37] T. Miyakawa, T. Sogo, and H. Pu, "Phase-space deformation of a trapped dipolar Fermi gas", *Phys. Rev. A* **77**, 061603(R), 2008.

- 
- [38] T. Sogo, L. He, T. Miyakawa, and S. Yi, "Dynamical properties of dipolar Fermi gases", *New. J. Phys.* **11**, 055017, 2008.
- [39] Y. Yamaguchi, T. Sogo, T. Ito and T. Miyakawa, "Density-wave instabilities in a two-dimensional dipolar Fermi gas", *Phys. Rev. A* **82**, 013643, 2010.
- [40] Kai Sun, Congjun Wu and S. Das Sarma, "Spontaneous inhomogeneous phases in ultracold dipolar Fermi gases", *Phys. Rev. B* **82**, 075105, 2010.
- [41] L. You, M. Marinescu, "Prospects for p-wave paired Bardeen-Cooper-Schrieffer states of fermionic atoms", *Phys. Rev. A* **60**, 2324, 1999.
- [42] M. A. Baranov, M. S. Marenko, V. S. Rychkov, and G. V. Shlyapnikov, "Superfluid pairing in a polarized dipolar Fermi gas", *Phys. Rev. A* **66**, 013606, 2002.
- [43] A. Pikovski, M. Klawunn, G.V. Shlyapnikov and L. Santos, "Interlayer Superfluidity in Bilayer Systems of Fermionic Polar Molecules", *Phys. Rev. Lett.* **105**, 215302, 2010.
- [44] M. A. Baranov, A. Micheli, S. Ronen, and P. Zoller, "Bilayer superfluidity of fermionic polar molecules: Many-body effects", *Phys. Rev. A* **83**, 043602, 2011.
- [45] G. E. Astrakharchik, J. Boronat, I. L. Kurbakov, and Yu. E. Lozovik, "Quantum Phase Transition in a Two-Dimensional System of Dipoles", *Phys. Rev. Lett.*, **98**, 060405, 2007.
- [46] C. Mora, O. Parcollet, and X. Waintal, "Quantum melting of a crystal of dipolar bosons", *Phys. Rev. B.*, **76**, 064511, 2007.
- [47] H.P. Büchler, E. Demler, M. Lukin, A. Micheli, N. Prokof'ev, G. Pupillo and P. Zoller, "Strongly Correlated 2D Quantum Phases with Cold Polar Molecules: Controlling the Shape of the Interaction Potential", *Phys. Rev. Lett.* **98**, 060404, 2007.
- [48] F. Cinti, P. Jain, M. Boninsegni, A. Micheli, P. Zoller, and G. Pupillo, "Supersolid Droplet Crystal in a Dipole-Blockaded Gas", *Phys. Rev. Lett.*, **105**, 135301, 2010.
- [49] A. G. Rojo, "Electron-drag effects in coupled electron systems", *J. Phys.: Condens. Matter* **11**, R31, 1999.

- 
- [50] Q. Li, E. H. Hwang, and S. Das Sarma, "Collective modes of monolayer, bilayer, and multilayer fermionic dipolar liquid", *Phys. Rev. B* **82**, 235126, 2010.
- [51] C.-C. Huang and W.-C. Wu, "Center motions of nonoverlapping condensates coupled by long-range dipolar interaction in bilayer and multilayer stacks", *Phys. Rev. A* **82**, 053612, 2010.
- [52] T. Lahaye, C. Menotti, L. Santos, M. Lewenstein, T. Pfau, "The physics of dipolar bosonic quantum gases", *Rep. Progr. Phys.* **72**, 126401, 2009.
- [53] K. Goral, B.-G. Englert and K. Rzazewski, "Semiclassical theory of trapped fermionic dipoles", *Phys. Rev. A* **63**, 033606, 2001.
- [54] W. L. McMillan, "Ground State of Liquid  $\text{He}^4$ ", *Phys. Rev.* **138**, A442-A451, 1965.
- [55] D. Schiff and L. Verlet, "Ground State of Liquid Helium-4 and Helium-3", *Phys. Rev.* **160**, 208-218, 1967.
- [56] D. Ceperley, G. V. Chester and M. H. Kalos, "Monte Carlo simulation of a many fermion study", *Phys. Rev. B* **16**, 3081, 1977.
- [57] P. A. Whitlock, D. M. Ceperley, G. V. Chester and M. H. Kalos, "Properties of liquid and solid  $^4\text{He}$ ", *Phys. Rev. B*, **19**, 5598-5633, 1979.
- [58] M. A. Lee, K. E. Schmidt, M. H. Kalos and G. V. Chester, "Green's function Monte Carlo method for liquid  $^3\text{He}$ ", *Phys. Rev. Lett.* **46**, 728-731, 1981.
- [59] J. B. Anderson, "A random-walk simulation of the Shrodinger equation: $H_3^+$ ", *J. Chem. Phys.* **63**, 1499-1503, 1975.
- [60] D. M. Ceperley, "Ground state of the fermion one-component plasma: A Monte Carlo study in two and three dimensions", *Phys. Rev. B* **18**, 3126-3128, 1978.
- [61] D. M. Ceperley and B. J. Alder, "Ground state of a electron gas by a stochastic method", *Phys. Rev. Lett.* **45**, 566, 1980.
- [62] Kolorenc J and Mitas L, "Application of Quantum Monte Carlo methods in condensed systems", *Rep. Prog. Phys.* **74**, 026502, 2011.
- [63] D. M. Ceperley and E. L. Pollock, "Path-integral computation of the low-temperature properties of liquid  $^4\text{He}$ ", *Phys. Rev. Lett.* **56**, 351-354, 1986.

- [64] N. V. Prokof'ev, B. V. Svistunov and I. Tupitsyn, "Exact, complete, and universal continuous-time worldline Monte Carlo approach to the statistics of discrete quantum systems", *JETP*, **87**, 310-321, 1998.
- [65] D. M. Ceperley, "Path-integral calculations of normal liquid  $^3\text{He}$ ", *Phys. Rev. Lett.*, **69**, 331-334, 1992.
- [66] C. Pierleoni, D. M. Ceperley, B. Bernu and W. R. Magro, "Equation of state of the hydrogen plasma by Path Integral Monte Carlo simulation", **73**, 2145-2149, 1994.
- [67] S. Giorgini, J. Boronat, and J. Casulleras, "Ground state of a homogeneous Bose gas: A diffusion Monte Carlo calculation", *Phys. Rev. A* **60**, 5129-5132, 1999.
- [68] S. Pilati, J. Boronat, J. Casulleras, and S. Giorgini, "Quantum Monte Carlo simulation of a two-dimensional Bose gas", *Phys. Rev. A*, **71**, 23605, 2005.
- [69] G. E. Astrakharchik, J. Boronat, J. Casulleras, and S. Giorgini, "Beyond the Tonks-Girardeau gas: Strongly correlated regime in quasi-one-dimensional Bose gases", *Phys. Rev. Lett.* **95**, 190407, 2005.
- [70] A.J. Leggett, "Diatomic molecules and cooper pairs", Springer-Verlag, Berlin, 1980.
- [71] G. E. Astrakharchik, J. Boronat, J. Casulleras, and S. Giorgini, "Equation of state of a Fermi gas in the BEC-BCS crossover: A Quantum Monte-Carlo study", *Phys. Rev. Lett.*, **93**, 200404, 2004.
- [72] S. Y. Chang, V. R. Pandharipande, J. Carlson, and K. E. Schmidt, "Quantum Monte Carlo studies of superfluid Fermi gases", *Phys. Rev. A*, **70**, 043602, 2004.
- [73] S. Pilati, G. Bertaino, S. Giorgini, and M. Troyer, "Itinerant Ferromagnetism of a Repulsive Atomic Fermi Gas: A Quantum Monte Carlo Study", *Phys. Rev. Lett.*, **105**, 030405, 2010.
- [74] M. P. A. Fisher, P. B. Weichman, G. Grinstein, and D. S. Fisher, "Boson localization and the superfluid-insulator transition", *Phys. Rev. B.*, **40**, 546, 1989.
- [75] S. Trotzky, L. Pollet, F. Gerbier, U. Schnorrberger, I. Bloch, N. V. Prokofev, B. Svistunov and M. Troyer, "Suppression of the critical temperature for superfluidity near the Mott transition", *Nature Physics*, **6**, 998, 2010.

- 
- [76] L. Pollet, N. V. Prokofev, B. V. Svistunov, and M. Troyer, "Absence of a Direct Superfluid to Mott Insulator Transition in Disordered Bose Systems", *Phys. Rev. Lett.*, **103**, 140402, 2009.
- [77] V. Gurarie, L. Pollet, N. V. Prokofev, B. V. Svistunov, and M. Troyer, "Phase diagram of the disordered Bose-Hubbard model", *Phys. Rev. B*, **80**, 214519, 2009.
- [78] E. Burovski, N. Prokofev, B. Svistunov and M. Troyer, "Critical temperature and thermodynamics of attractive fermions at unitarity", *Phys. Rev. Lett.*, **96**, 160402, 2006.
- [79] A. Bulgac, J. E. Drut, and P. Magierski, "Spin 1/2 fermions in the unitarity regime", *Phys. Rev. Lett.*, **96**, 90404, 2006.
- [80] L. Pollet, "Recent developments in Quantum Monte-Carlo simulations with applications for cold gases", *Rep. Prog. Phys.* **75**, 094501, 2012.
- [81] L. Pollet, J. D. Picon, H. P. Buchler, and M. Troyer, "Supersolid Phase with Cold Polar Molecules on a Triangular Lattice", *Phys. Rev. Lett.*, **104**, 125302, 2010.
- [82] B. Capogrosso-Sansone, C. Trefzger, M. Lewenstein, P. Zoller, and G. Pupillo, "Quantum Phases of Cold Polar Molecules in 2D Optical Lattices", *Phys. Rev. Lett.*, **104**, 125301, 2010.
- [83] K. Van Houcke, F. Werner, E. Kozik, N. Prokofev, B. Svistunov, M. J. H. Ku, A. T. Sommer, L. W. Cheuk, A. Schirotzek, and M. W. Zwierlein, "Feynman diagrams versus Fermi-gas Feynman emulator", *Nature. Phys.*, **8**, 366, 2012.
- [84] P.G. Hoel, S.C. Port, and C.J. Stone, "Introduction to stochastic processes", Houghton Mifflin Company, 1972.
- [85] G.E.P. Box and M.E. Muller, "A Note on the Generation of Random Normal Deviates", *The Annals of Mathematical Statistics*, **29**, 610, 1958.
- [86] W. H. Press, S. A. Teukolsky, W. T. Vetterling, B. P. Flannery, "Numerical receipts in C", Oxford University Press, 1992.
- [87] N. Metropolis, A. W. Rosenbluth, M. N. Rosenbluth, A. H. Teller and E. Teller, "Equation of state calculations by fast computing machine", *Jour. Chem. Phys.* **21**, 1087, 1953.
- [88] W.K. Hastings, "Monte Carlo Sampling Methods Using Markov Chains and Their Applications", *Biometrika*, **57(1)**, 97, 1970.

- 
- [89] P. Davies, "Quantum mechanics", Chapman and Hall, 1994.
- [90] P. Atkins, "Molecular quantum mechanics", Oxford University Press, 1983.
- [91] P. J. Rossky, J.D. Doll, and H.L. Friedman, "Brownian dynamics as smart Monte Carlo simulation", *Jour. Chem. Phys.* **69**, 4628, 1978.
- [92] C. Pangali, M. Rao, and B.J. Berne, "On a novel Monte Carlo scheme for simulating water and aqueous solutions", *Chem. Phys. Lett.*, **55**, 413, 1978.
- [93] S. Sorella, "Wave function optimization in the variational Monte Carlo method", *Phys. Rev. B*, **71**, 241103(R), 2005.
- [94] R. Guardiola, "Monte Carlo methods in quantum many-body theories", Springer, 1998.
- [95] B. L. Hammond, W. A. Lester, Jr., and P. J. Reynolds, "Monte Carlo methods in ab initio quantum chemistry", World Scientific, 1994.
- [96] J. Vrbik and S. M. Rothstein, "Quadratic accuracy diffusion Monte Carlo", *J. Comput. Phys.* **63**, 130, 1986.
- [97] P.J. Reynolds, "Fixed-node quantum Monte Carlo for molecules", *Jour. Chem. Phys.* **77**, 5593, 1982.
- [98] J. Slater, "The theory of complex spectra", *Phys. Rev.*, **34**, 1293, 1929.
- [99] L.D. Landau, "Theory of Fermi-Liquids", *Sov. Phys. JETP*, **3**, 1957.
- [100] A.A. Abrikosov and I.M. Khalatnikov, "The theory of a fermi liquid (the properties of liquid  $^3\text{He}$  at low temperatures)", *Reports on Progress in Physics*, **22**, 329, 1959.
- [101] E. M. Lifshitz and L. P. Pitaevskii, *Statistical Physics, Part 2* (Pergamon Press, Oxford, 1980).
- [102] S. Pilati and S. Giorgini, "Phase Separation in a Polarized Fermi Gas at Zero Temperature", *Phys. Rev. Lett.*, **100**, 030401, 2008.
- [103] S.-Y. Chang, M. Randeria, and N. Trivedi, "Ferromagnetism in repulsive Fermi gases: upper branch of Feshbach resonance versus hard spheres", *Proc. Natl. Acad. Sci.* **108**, 51-54, 2011.
- [104] D. M. Ceperley and M. H. Kalos, "Monte-Carlo methods in statistical physics", Springer, Berlin, 1979.

- 
- [105] A. Sarsa, J. Boronat and J. Casulleras, "Quadratic accuracy diffusion Monte Carlo and pure estimators for atoms", *J. Chem. Phys.* **116**, 5956, 2002.
- [106] G. M. Bruun and E. Taylor, "Quantum phases of a two-dimensional dipolar fermi gas", *Phys. Rev. Lett.* **101**, 245301, 2008.
- [107] N.T. Zinner and G.M. Bruun, "Density Waves in Layered Systems with Fermionic Polar Molecules", *Eur. Phys. J. D* **65**, 133, 2011.
- [108] M. Babadi and E. Demler, "Density ordering instabilities of quasi-two-dimensional fermionic polar molecules in single-layer and multilayer configurations: Exact treatment of exchange interactions", *Phys. Rev. B* **84**, 235124, 2011.
- [109] L.M. Sieberer and M.A. Baranov, "Collective modes, stability, and superfluid transition of a quasi-two-dimensional dipolar Fermi gas", *Phys. Rev. A* **84**, 063633, 2011.
- [110] M.M. Parish and F.M. Marchetti, "Density instabilities in a two-dimensional dipolar fermi gas", *Phys. Rev. Lett.* **108**, 145304, 2012.
- [111] B. Spivak and S.A. Kivelson, "Phases intermediate between a two-dimensional electron liquid and Wigner crystal", *Phys. Rev. B* **70**, 155114, 2004.
- [112] B. Tanatar and D. M. Ceperley, "Ground state of the two-dimensional electron gas", *Phys. Rev. B* **39**, 5005-5016, 1989.
- [113] C. Lin, F. H. Zong and D. M. Ceperley, "Twist-averaged boundary conditions in continuum quantum Monte Carlo algorithms", *Phys. Rev. E* **64**, 016702, 2001.
- [114] S. Chiesa, D. M. Ceperley, R. M. Martin and M. Holzmann, "Finite-Size Error in Many-Body Simulations with Long-Range Interactions", *Phys. Rev. Lett.* **97**, 076404, 2006.
- [115] M. Holzmann, B. Bernu, C. Pierleoni, J. McMinis, D. M. Ceperley, V. Olevano, and L. D. Site, "Momentum distribution of the homogeneous electron gas", *Phys. Rev. Lett.* **107**, 110402, 2011.
- [116] M. Holzmann, B. Bernu, V. Olevano, R.M. Martin and D.M. Ceperley, "Renormalization factor and effective mass of the two-dimensional electron gas", *Phys. Rev. B* **79**, 041308(R), 2009.

- 
- [117] B. Simon, "The bound state of weakly coupled Schrodinger operators in one and two dimensions", *Ann. Phys.* **97**, 279, 1976.
- [118] M. A. Baranov, A. Micheli, S. Ronen, and P. Zoller, "Bilayer superfluidity of fermionic polar molecules: Many-body effects", *Phys. Rev. A* **83**, 043602, 2011.
- [119] J. M. Feagin, "Quantum Methods With Mathematica", Springer, 2002.
- [120] M. Klawunn, A. Pikovski, and L. Santos, "Two-dimensional scattering and bound states of dipolar molecules in bilayers", *Phys. Rev. A* **82**, 044701, 2010.
- [121] M. Klawunn, and A. Recati, "Polar molecules in bilayers with high population imbalance", arXiv:1110.2336.
- [122] J. Boronat and J. Casulleras, "Quantum Monte Carlo study of static properties of one  $^3\text{He}$  atom in superfluid  $^4\text{He}$ ", *Phys. Rev. B* **59**, 13, 1999.